UNIVERSITY OF CALIFORNIA

Los Angeles

Rapid Thermal and Electrochemical Characterization with Low Measurement Uncertainty

A dissertation submitted in partial satisfaction

of the requirements for the degree

Doctor of Philosophy in Mechanical Engineering

by

Yuan Hu

2021

ABSTRACT OF THE DISSERTATION

Rapid Thermal and Electrochemical Characterization with Low Measurement Uncertainty

by

Yuan Hu
Doctor of Philosophy in Mechanical Engineering
University of California, Los Angeles, 2021
Professor Timothy S. Fisher, Chair

Spectroscopy methods are widely used for system characterization. Typically a perturbation signal is introduced to the system, and corresponding outputs are detected. The underlying properties of a system can be determined by comparing the output to the input. This work employs advanced statistical methods to improve overall performance of such methods applied to energy transport and storage, in terms of accuracy, time efficiency and cost for spectroscopy methods to characterize thermal and electrochemical systems.

The first part of this work reports a custom spectroscopy system that employs periodic heating to characterize thermal diffusivity under ambient conditions; the technique is also known as Ångström's method. We employ forced convection to reduce variation in convective heat transfer losses along the heat propagation direction to enable the experiment to be conducted outside vacuum. We employ IR thermography to for data-rich temperature detection and further introduce a Bayesian framework for uncertainty quantification and uncertainty reduction with increased data. We demonstrate accurate results ($< 5\%$ error) for multiple short metal strips.

In the second part we extend the room temperature spectroscopy approach to high temperatures. For high-temperature characterization, the testing environment is difficult to control precisely; therefore, additional unknowns exist in the physical model as compared to

low-temperature measurements. In addition, nonlinear radiation loss are present, and the transient heat transfer process must be modeled numerically. Solving the inverse problem using conventional regression approaches is challenging because the solutions are not unique and lack uncertainty estimates. Therefore, we develop a Bayesian framework to solve the inverse problem. The main challenges overcome are: (1) probing the posterior distribution given a computationally expensive forward model and (2) achieving convergence in the sampling process for a model with a relatively high number of unknowns. In this study we report a computationally efficient parametric surrogate model to accelerate the Bayesian analysis and employ a No-U-Turn sampler to achieve good convergence in the sampling process. The custom instrument exhibits high accuracy (approx. 5% error) and requires only 10 min. obtain steady high-temperature results, compared to several hours using conventional methods and commercial instruments.

Lastly we demonstrate a broadband spectroscopy instrument for electrochemical impedance spectroscopy (EIS) measurements for supercapacitors. Measuring EIS is challenging because (1) low-frequency scans are time consuming and (2) impedance of supercapacitors typically changes by several orders of magnitude across a wide frequency band. The custom instrument employs a broadband exponential chirp signal for rapid frequency scanning. To account for large impedance variations, we report a custom circuit for automatically adaptable impedance matching during measurements. The custom instrument is accurate and exhibits four times measurement time reduction and ten times cost reduction compared to leading commercial instruments.

The dissertation of Yuan Hu is approved.

Jayathi Y. Murthy

Tsu-Chin Tsao

Richard B. Kaner

Timothy S. Fisher, Committee Chair

University of California, Los Angeles

2021

This dissertation is dedicated to my parents, who support me with everything they have

TABLE OF CONTENTS

LIST OF FIGURES

LIST OF TABLES

ACKNOWLEDGMENTS

I would like to thank many fantastic people that contributed to this dissertation and help me in many aspects during my PhD period. First, I am sincerely grateful to my advisor, Prof. Fisher, who is a great mentor and always have the students' best interest at heart. I was once just an undergrad exchange student in Purdue from Shanghai Jiao Tong and knew little about what I can do to make a difference. With his support and guidance, I became a passionate researcher about instrumentation and data science and dedicate to develop new measurement instruments for thermal and electrochemical community. I appreciate the kind help from Prof. Murthy, Prof. Tsao and Prof. Kaner for serving ony my doctoral committee and providing instructive feedback on my dissertation. I am grateful for my advisory committee at Purdue before moving to UCLA. I am thankful for Prof. Bilionis at Purdue and because of his excellent free online uncertainty quantification lectures, I became interested in the topic and it became a significant part of this dissertation. I am grateful for Prof. Davies at Purdue for her kind guidance and many fruitful discussions on signal process for electrochemical impedance spectroscopy. I also owe much gratitude to Prof. Reifenburger at Purdue, who gave me motivation to pursue better instrumentation technologies. For faculties at UCLA I am especially grateful for Prof. Handcock from stat department for Bayesian analysis for room temperature thermal characterization; Prof. Eldredge for many detailed and patient guidance on Kalman filter and numerical heat transfer coding. I am thankful for my NTRG colleagues at Purdue and UCLA, Aaditya, Rajath, Arpan, Menlong, Guoping, Pingge, Kim, Aunrag, Rajib, Brian, Ujash, Matt, Mostafa, Abdalla, Saurin, Indro, Yanguang, Yijun, Kaiyuan, Yang and many others for so many unforgettable memories. I am also grateful to my undergrad friends Xiongfeng Zhu and Tan Chen for many advice on research and career. Lastly, I would like to thank my parents and many other family members. Without their support from behind the scene, I will never become the person I am today. To all the people who have helped me, "Thank you very much!"

I am grateful for the Center for Integrated Thermal Management of Aerospace Vehicles,

UCLA Dissertation Year Fellowship and YTC America for funding support for my PhD period. I would like to once again thank these funding agencies and UCLA TDG for many of their efforts to commercialize some of my research projects.

VITA

2012 - 2014	M.S., Mechanical Engineering, Purdue University, West Lafayette, Indiana
2009 - 2013	B.S., Mechanical Engineering, Shanghai Jiao Tong University, Shanghai, China

PUBLICATIONS

Hu, Y., Abuseada, M., Alghfeli, A., Holdeim, S., Fisher, T.S.,"High-temperature thermal diffusivity measurements using a modified Ångström's method with transient infrared thermography". Submitted.

Hu, Y., Abuseada, M., Alghfeli, A., Holdeim, S., Fisher, T.S.,"Surrogate-accelerated Bayesian framework for high-temperature thermal diffusivity characterization". In preparation.

Hu, Y., and Fisher, T.S.,"Accurate Thermal Diffusivity Measurements Using a Modified Ångström's Method with Bayesian Statistics". *J of HEAT TRANSFER-TRANSACTIONS OF THE ASME.*, 2020, **142**(7), p.071401.

Hu, Y., Brahim, S., Maat, S., Davies, P., Kundu, A., and Fisher, T.S.,"Rapid Analytical Instrumentation for Electrochemical Impedance Spectroscopy Measurements". *J. Electrochem. Soc.*, 2020, **167**(2), p.027545.

Vinnacombe-Willson, G., Chiang, N., Scarabelli, L., Hu, Y. et al., "In Situ Shape Control of Thermoplasmonic Gold Nanostars on Oxide Substrates for Hyperthermia-Mediated Cell Detachment". *ACS Cent. Sci.*, 2020, **6**(11), pp.2105–2116.

Xu, X., Zhang, Q., Hao, M., Hu, Y. et al.,"Double-negative-index ceramic aerogels for thermal superinsulation". *Science*, 2019, **363**(6428), pp.723-727.

Hu, Y., Fisher, T.S.,"Suggested standards for reporting power and energy density in supercapacitor research". *Bull. Mater. Sci.*, 2018, **41**(5), pp.1-4.

Hu, Y., Fisher, T.S., "Accurate Thermal Diffusivity Instrument for Foil-Like Samples with Systematic Uncertainty Quantification".*Proceedings of the Thirty-fourth International Thermal Conductivity and Thermal Conductivity Conference*, 2019, pp.48-54.

Irwin, R., Hu, Y., Alam, A., Benedic, S., Fisher, T.S., Iyer, S.S.,"Nanowire Impregnated Poly-dimethyl Siloxane for Flexible, Thermally Conductive Fan-Out Wafer-Level Packaging".*2020 IEEE 70th Electronic Components and Technology Conference (ECTC)*, 2020, pp.1548-1553.

CHAPTER 1

Introduction

Spectroscopy methods are powerful tools to characterize thermal and electrochemical system because of their simplicity and robustness. However, current spectroscopy techniques are time-consuming, expensive and lack systematic uncertainty quantification. Therefore, this dissertation is written to develop novel spectroscopy methods with faster measurement speed, lower cost and systematic framework for uncertainty quantification.

This chapter identifies the need for enhanced spectroscopy method and outlines the objectives of the current study. Section 1.1 briefly discuss the advantage of spectroscopy methods to characterize thermal diffusivity and existing studies. We also briefly review the constrains of existing techniques for both room temperature and high temperature characterizations and present our solutions. Section 1.2 briefly discuss the significance of electrochemical impedance spectroscopy (EIS) techniques are existing studies. We also discuss the limitations of current studies and our improvements. Section 1.3 overviews this dissertation by chapter and summarize the main contributions of this work.

1.1 Spectroscopy method for thermal diffusivity characterization

In this study, we discuss spectroscopy methods for thermal diffusivity characterization at ambient condition and at high temperature respectively.

1.1.1 Ambient condition thermal diffusivity characterization

Thin-film foil-like materials are commonly used as heat spreader in electronic packaging for thermal management [86][22]. Precise understanding of thermal properties of the heat spreader are crucial to accurately model the temperature of the chip in real time. For such materials, established thermal diffusivity measurements typically employ transient approaches, such as 3ω [36] and laser flash [95] methods. 3ω methods require a layer of metallic coating on the sample. This layer often involves cleanroom processes and deposition in vacuum at elevated temperatures [137], which can potentially alter the sample. Laser flash is another established transient technique; however it suffers heat loss from sample to the holder for less thermally conductive materials [94]. Steady-state approaches, such as Joule heating methods, are also commonly used for thermal conductivity measurements of bulk materials and for thermal interfacial resistance [130][59]. However, the setups typically involve vacuum to eliminate convection losses and long times to reach steady state. Meanwhile, contact resistance between the instrument and the sample also contributes to measurement error, which is difficult to quantify.

Ångström's method was initially developed in 1863 [20] and is another effective approach for one-dimensional thermal diffusivity measurements. As compared to 3ω and laser flash methods, Ångström's method involves less sample preparation and does not require minimization of heat loss to surroundings. As compared to steady-state methods, Ångström's method is much faster and does not require accurate quantification of Joule heating into the sample, thermal resistance between the instrument and the sample, and heat loss to the surroundings. A limitation of the original Ångström's method is its semi-infinite assumption, such that long samples (>150 mm) are typically required [140][97][88]. To enable thermal diffusivity measurements on short samples, a modified Ångström's method was developed by Lopez-Baeza et al. [77] based on a transient fin model of a cylindrical rod, and temperatures were measured using thermocouples in vacuum. However, this setup is not appropriate for temperature measurements in thin films because of heat loss to the temperature sensors.

This work is based on Lopze-Baeza et al.'s physical model, but employs IR thermography

for non-contact temperature measurements. For IR thermography, accurately measuring temperature of samples placed in vacuum is challenging because infrared radiation would be measured through a specialized window. Therefore in this work, IR thermography is performed at ambient conditions, in which temperature measurements are much noisier as compared to those performed in vacuum. In order to quantify and reduce experimental uncertainty, this work reports a Bayesian framework that benefits from the increased number of temperature measurements in IR thermography to reduce parameter uncertainties.

1.1.2 High temperature thermal diffusivity characterization

Accurate thermal diffusivity characterization at high temperatures is very important for aerospace [93][27][108] and energy industries [138][117][100]. Currently, the laser-flash [95, 41, 40], transient plane source [55], hot wire [61] and Ångström's [20][106] methods are commonly used for such characterization. Compared to other methods, Ångström's method is robust and simple to realize. Typically a portion of a sample is periodically heated, and thermal diffusivity is extracted by analyzing amplitude and phase differences between temperature profiles along the heat conduction direction. The method typically does not require knowledge or precise control of (1) contact resistance between the sample and the heater, (2) heat input to the sample, and (3) sample heat loss to the surroundings.

Ångström's method has been previously used for thermal diffusivity characterization at high temperatures. Prior studies can be categorized into in-plane and cross-plane measurements. For in-plane measurements, the sample is typically heated periodically at an outer surface, whereas top and bottom surfaces are thermally insulated. Two thermocouples are placed at different radii to measure oscillatory temperature profiles, and thermal diffusivity is computed from temperature amplitude decay, phase shift or both. Katsura[69] used such a technique on silica glass up to 9 GPa and 1200 K with approx. 3% accuracy. Xu et al.[132] used a similar apparatus and measured olivine, wadsleyite and ringwoodite up to 1373 K with 12% accuracy. For thin sheets or foils, Hatta et al.[60] used a mask to cover part of a strip sample and irradiated both the sample and the mask using a lamp with periodic

intensity. Thermal diffusivity was calculated by measuring the decay of temperature oscillation at multiple locations within the masked region. This method achieved 5% accuracy for in-plane thermal diffusivity of nickel foil up to 500 °C.

For cross-plane measurements, a cylindrical sample can be periodically heated at either a top or bottom surface. Typically two or three thermocouples are placed at different axial locations to measure temperature oscillations, and thermal diffusivity is extracted based on amplitude decay and phase shift. Sidles and Danielson[106] developed an apparatus and measured copper and nickel rods (>50 cm) up to 500 °C. Abeles et al. [13] reported an apparatus that measures thermal diffusivity of cylindrical solids (Armco iron and germanium) up to 1000 °C with an accuracy of approx. 2%. Vandersande and Pohl[119] reported an instrument that is more convenient to assemble and is capable of measuring thermal diffusivity between 80-500 K with ±3% - ±7% accuracy. An alternative technique for cross-plane thermal diffusivity measurements was developed by Cowan[42]. The method is similar to the laser flash method and is suitable for electrically conductive thin disks. In Cowan's method, a high-intensity electron gun with uniform intensity distribution bombards the front side of the disk periodically. The temperature phase difference between the front and the back surfaces of the disk is used to determine thermal diffusivity. Wheeler[125] used this approach and measured refractory metals up to 3000 K with 5% accuracy. Tanaka and Suzuki[115] employed a similar technique on pyrolytic graphite up to 1900 K with 5% accuracy.

The foregoing methods (except Cowan's) require a heat source external to the sample to heat it and the surroundings to high temperature prior to periodic heating. This process is typically lengthy, requiring hours to reach steady, elevated temperature. To mitigate heat loss, radiation shields are often used that preclude the use of non-contact, non-intrusive temperature detection. Thermocouples are commonly used, and drilling or welding is typically involved to attach thermocouples to the sample, introducing heat losses and potentially altering the sample's structure. In addition, temperature measurements are limited by the number of thermocouples, leading to unreliable results if defects are present between the thermocouples[58].

In this work and in contrast to methods that heat samples from surroundings, we employ a concentrated light source to directly heat samples (3.5" OD thin disks) to high temperatures. Upon reaching a steady target temperature (typically under 10 mins), we modulate the light source's heat flux periodically. This approach significantly decreases the total time for characterization and increases testing throughput. Similar to Hatta et al.'s approach[60], we partially block the light source such that only the center of the sample is heated. However, several key difference exist. First, in Hatta's work samples were heated to high temperatures (up to 500 °C) from the surroundings. Second, in Hatta et al.'s work the radiation losses were linearized, whereas in our case temperature gradients along the direction of heat conduction exist even under steady heating, and nonlinear radiation losses are included in the model. Thirdly, in Hatta's work amplitude decay was calculated by comparing two temperature profiles, one from the unmasked region and the other from the masked region. This approach requires the light source to be highly uniform. In our approach, amplitude decay and phase shift are calculated only from masked region. This approach is more robust against uncertainties and variations in the intensity distribution of the light source, as later demonstrated in our sensitivity analysis. Fourthly, Hatta's work requires thermocouples for temperature detection. In our study, an IR camera calibrated up to 2000 °C is employed for non-contact and non-intrusive temperature detection. Moreover, IR thermography offers data-rich temperature profiles that increase measurement reliability[58] and decrease uncertainties for parameters of interest [67]. Here, we employ a Bayesian framework that benefits from the data-rich IR thermography to quantify uncertainty rigorously for the parameters of interest.

In our study we employ a concentrated light source to directly heat the sample to steady high temperatures rapidly. However, this introduces significant temperature gradient along the heat conduction direction. As a result, radiation losses cannot be linearized and temperature-dependent properties are required to evaluate the physical model numerically. This create several difficulties for parameter estimation. First, applying regression approaches suffer solution uniqueness issue because of large number of local minima for the

nonlinear models. Instead of seeking specific parameters that best fit the model, we employ a Bayesian framework and treat parameters as random variables with statistical distributions. In addition, Bayesian framework does not require linearing the model for uncertainty quantification as compared to the covariance matrix approach [21]. Furthermore, Bayesian framework allows incorporating prior knowledge for the parameter of interest using a prior distribution, which also serves as a regularization mechanism for the inverse problem [122].

The disadvantage of the Bayesian framework is that it probes a probability distribution using Markov chain Monte Carlo (MCMC) methods, which require to evaluate the physical model extensively and becomes impractical when the physical model is computationally expensive. To accelerate the Bayesian analysis, previous studies from other fields employ surrogate models or reduced order models to replace the original model [23][101][114]. In this study, we develop an accurate parametric surrogate model in the form of polynomial chaos and achieve nearly four orders of magnitude of speed improvement.

Having obtained an efficient surrogate model, we discuss another challenge in the sampling process. Conventional sampling techniques typically employ random walk to explore the parameter space. However, this becomes inefficient as the number of unknowns increase and suffers poor convergence in the sampling process. We employ a No-U-Turn sampler which explores the posterior distribution more thoroughly and demonstrates satisfactory convergence for the sampling process.

1.2 Spectroscopy method for electrochemical characterization

Supercapacitors (or electrochemical capacitors) with high power densities, short charging times and long cycle lifetimes are being widely used in energy management applications, such as hybrid vehicles, energy harvesting processes, consumer electronics and bulk energy storage from the utility grid [70][128]. Research and development in the field of supercapacitors is becoming increasingly important as the market grows [37][39]. Electrochemical impedance spectroscopy (EIS) is one of the most common techniques to assess the electro-

chemical performance of supercapacitors [113][17]. It measures impedance over a relevant frequency band and is often performed under DC bias voltage. EIS provides fundamental performance indicators, such as capacitance, equivalent series resistance (ESR) and response to arbitrary input signals in the time domain [33]. This work focuses on supercapacitors with relative lower nominal voltages (about 2 V). These supercapacitors are typically assembled in series and parallel configurations to achieve higher nominal voltage and capacitance for energy storage applications [66]. For such supercapacitors, EIS are typically performed under nominal bias voltages [105] to characterize their in-operando performance. For EIS measurements, the majority of prior electrochemical studies have used commercially available instruments. Such instruments typically perform multiple measurements each at a single frequency using steady-state response to sinusoidal input, and scan the entire frequency band sequentially. The main drawback of this approach is its lengthy measurement time at low frequencies[96]. In contrast, broadband excitation that reduces measurement time can be achieved by using exponential chirp signals, for which the frequency sweep rate is exponential [43][134]. By using these chirp signals, more time is spent exciting the supercapacitor at lower frequencies. The expression for a generic exponential chirp voltage signal as a function of time t is given in Eq. 1.1:

$$v(t) = A \sin\left\{\phi_0 + 2\pi f_0 \left(\frac{k^t - 1}{\ln k}\right)\right\}, k = \left(\frac{f_1}{f_0}\right)^{1/T} \tag{1.1}$$

where A is the voltage amplitude, ϕ_0 is the initial phase, f_0 is the starting frequency, f_1 is the ending frequency, and T is the time required to scan from f_0 to f_1. Fig. 1.1A shows an exponential chirp signal with initial frequency f_0= 10 mHz, final frequency f_1= 10 Hz and the total sweep time T to scan from f_0 to f_1 (T=150 s). Figs. 1.1B and C show exponentially varied frequency with respect to time for chirp signals, and illustrate the proportion of time spent in different frequency bands on logarithm and linear frequency scales respectively.

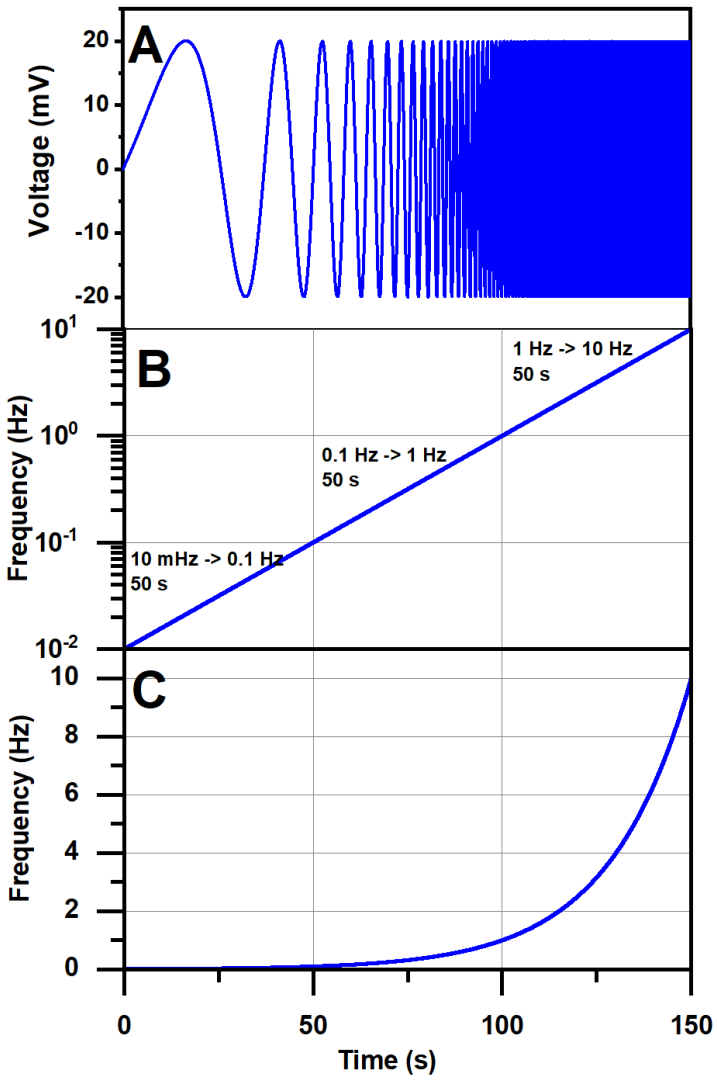

Figure 1.1: (A) A chirp signal with initial frequency $f_0 = 10$ mHz, final frequency $f_1 = 10$ Hz, and $T = 150$ s. (B) The frequency as a function of time for the chirp signal shown in (A) on a logarithm frequency scale. The time required to scan each frequency decade is 50 s. (C) The frequency with respect to time for the chirp signal shown in (A) on a linear frequency scale.

A previously study using chirp signals was able to obtain accurate EIS results from 1 Hz to 2 kHz for a Randles equivalent circuit composed of resistors and capacitors with known values [43]. However, real supercapacitors typically require a broader frequency band

from a few millihertz to a few kilohertz to characterize important performance parameters [133][112][129][73], such as self-discharge rate, ionic transfer resistance, ESR and capacitance [98]. Therefore, obtaining EIS information for supercapacitors over such broad frequency band under a bias voltage is critical for electrochemical research as well as manufacturing quality control. Here, we report a new technique that employs automatically selectable shunt resistances and different chirp signals tuned to frequency subbands adaptively. As a result, accurate EIS measurements are achieved over a broad frequency band (10 mHz to 2 kHz) for multiple commercial and laboratory-fabricated supercapacitor samples.

1.3 Overview of the dissertation

In this dissertation, Chapter 2 presents a custom thermal diffusivity instrument using a spectroscopy technique, also known as Ångström's method to accurately measure foil-like materials. The highlights of this study is summarized below:

1. Conventional Ångström's methods are performed in vacuum. However, this is inconvenient and some samples are inappropriate to test under vacuum. We introduce forced convection using a uniform air nozzle to ensure "uniform" convective heat transfer coefficient along heat propagation direction. This enables the experiment to be conveniently performed in regular ambient conditions.

2. Conventional Ångström's method requires semi-infinite medium assumption and existing studies typically uses long samples (> 150mm) to satisfy this condition. We employ an analytical solution with adiabatic tip condition which enables characterizing short samples (25 mm).

3. Previous studies employ regression techniques to solve inverse heat transfer problems. However, this approach does not produce unique solution and lacks rigorous uncertainty quantification. In this study we present a Bayesian framework for uncertainty

quantification.

Chapter 3 extends the spectroscopy technique to characterize more challenging high temperature thermal diffusivities. We present a custom instrument that periodically heats a disk sample under vacuum with a concentrated light source directly. The highlights of this study are:

- Previous studies and commercial instruments heat samples indirectly from the surroundings to reach high temperatures. This process is time-consuming and typically requiring hours to reach stable temperatures. In this work samples are heated directly by a concentrated light source and are able to reach high steady-periodic temperatures in approx. 10 mins.

- Existing Ångström's methods for high temperature characterizations use thermocouples for temperature detection that are commonly attached to samples via drilling and welding, which are destructive to samples and introduce thermal anomalies. In addition, thermocouples detect temperature at point locations. In this work we use an infrared camera calibrated to 2000 °C for non-contact, non-destructive and data-rich temperature measurements. We present an image analysis approach to process the IR data that significantly reduces random noise in temperature measurements. We extract amplitude and phase from processed temperature profiles and demonstrate that these metrics are insensitive to uncertainty in emissivity.

Chapter 4 reports the data science framework we develop to solve the inverse problem for the high temperature thermal diffusivity instrument presented in Chapter 3. We present a Bayesian framework to solve the inverse problem involving the numerical transient heat transfer model with radiation and temperature-dependent properties. The highlights of this study are:

1. In previous studies, regression techniques are used to solve inverse problems and determine thermal diffusivity by minimizing the residual between measurement results and

model simulation. This approach lacks uncertainty quantification and does not allow to incorporate prior knowledge. Adopting a Bayesian framework addresses these issues, however, probing the posterior distribution is prohibitively expensive using Markov chain Monte Carlo (MCMC) methods, especially when the forward model must be evaluated numerically. This work reports a Bayesian framework for a custom high temperature characterization system using a modified Ångström's method. This study employs a parametric surrogate model in the form of polynomial chaos to accelerate the numerical physical model by several orders of magnitude to enable Bayesian analysis.

2. Previous studies commonly employ random walk to propose new parameters in the MCMC sampling process. Such an approach suffers poor convergence and high autocorrelation with increased number of parameters. To overcome the poor convergence of random walk based sampling approach, this study employs a No-U-Turn sampler which explore the posterior distribution more thoroughly and exhibits better convergence.

Chapter 5 presents the custom electrochemical impedance spectroscopy (EIS) analyzer capable of rapid and accurate frequency scan for supercapacitor pouch cells. Conventionally, EIS is measured via sinusoidal perturbations; however, such an approach suffers from lengthy measurement time. Chirp signals have been shown previously to reduce EIS measurement time for supercapacitors for relative narrow frequency bands (1 Hz to 2 kHz). However, to characterize supercapacitors comprehensively, much broader frequency bands are required. In chapter 5, we present a custom instrument with an adaptive measurement algorithm for performing EIS measurements in a wide frequency range of 10 mHz to 2 kHz with low measurement uncertainties. The results obtained using this new technique has been validated here with a commercial instrument on several types of supercapacitors. Furthermore, measurement time on average decreases from 1500 s to less than 400 s. The overall cost of the custom instrument is 90% lower as compared to the commercial instrument.

Chapter 6 presents our recommended metric for reporting supercapacitor research. For

supercapacitors, power density and energy density are the most significant metrics. However currently no dominant, established standard exists, and research papers often report these two metrics differently. A standard for reporting power and energy density is proposed in chapter 6 for objective comparison. This chapter also discusses a common flaw in current supercapacitor power density calculations.

Chapter 7 presents our collaborations with other research groups for thermal system characterizations. In section 7.1 we present an energy balance method to characterize laser to heat conversion for gold nanostars. In section 7.2 we present a transient plane source method to characterize thermally insulating aerogel. In section 7.3 we employ the room temperature Ångström's method to characterize PDMS enhanced with silver and copper nanowire.

CHAPTER 2

Accurate Thermal Diffusivity Measurements using a Modified Ångström's Method with Bayesian Statistics

2.1 Introduction

For thin-film foil-like materials, established thermal diffusivity measurements typically employ transient approaches, such as 3ω [36] and laser flash [95] methods. 3ω methods require a layer of metallic coating on the sample. This layer often involves cleanroom processes and deposition in vacuum at elevated temperatures [137], which can potentially alter the sample. Laser flash is another established transient technique; however it suffers heat loss from sample to the holder for less thermally conductive materials [94]. Steady-state approaches, such as Joule heating methods, are also commonly used for thermal conductivity measurements of bulk materials and for thermal interfacial resistance [130][59]. However, the setups typically involve vacuum to eliminate convection losses and long times to reach steady state. Meanwhile, contact resistance between the instrument and the sample also contributes to measurement error, which is difficult to quantify.

Ångström's method was initially developed in 1863 [20] and is another effective approach for one-dimensional thermal diffusivity measurements. As compared to 3ω and laser flash methods, Ångström's method involves less sample preparation and does not require minimization of heat loss to surroundings. As compared to steady-state methods, Ångström's method is much faster and does not require accurate quantification of Joule heating into the sample, thermal resistance between the instrument and the sample, and heat loss to the surroundings. A limitation of the original Ångström's method is its semi-infinite assumption,

such that long samples (>150 mm) are typically required [140][97][88]. To enable thermal diffusivity measurements on short samples, a modified Ångström's method was developed by Lopez-Baeza et al. [77] based on a transient fin model of a cylindrical rod, and temperatures were measured using thermocouples in vacuum. However, this setup is not appropriate for temperature measurements in thin films because of heat loss to the temperature sensors.

This work is based on Lopze-Baeza et al.'s physical model, but employs IR thermography for non-contact temperature measurements. For IR thermography, accurately measuring temperature of samples placed in vacuum is challenging because infrared radiation would be measured through a specialized window. Therefore in this work, IR thermography is performed at ambient conditions, in which temperature measurements are much noisier as compared to those performed in vacuum. In order to quantify and reduce experimental uncertainty, this work reports a Bayesian framework that benefits from the increased number of temperature measurements in IR thermography to reduce parameter uncertainties.

2.2 Theory

This is the edited content based on review comments We begin with governing equations for the transient fin model. The length, width and the thickness of the fin are l, w, and t_f respectively. The cross-section area of the fin is A_C, and the perimeter is P. The thermal conductivity and diffusivity of the fin are k and α, respectively. The base of the fin is periodically heated (frequency ω, rad/s), and the fin tip is assumed to be thermally insulated. The fin is exposed to an environment with convective heat transfer coefficient h:

$$\begin{cases} \frac{1}{\alpha}\frac{\partial T}{\partial t} + m^2 T = \frac{\partial^2 T}{\partial x^2}, m = \frac{hP}{kA_C} \\ \frac{\partial T}{\partial x}\big|_{x=l} = 0 \\ T(x,t)|_{x=0} = T_0 \exp(i\omega t) \end{cases} \tag{2.1}$$

where all parameters are assumed to be constant and uniform. A schematic for the transient fin problem is shown in Fig. 2.1A.

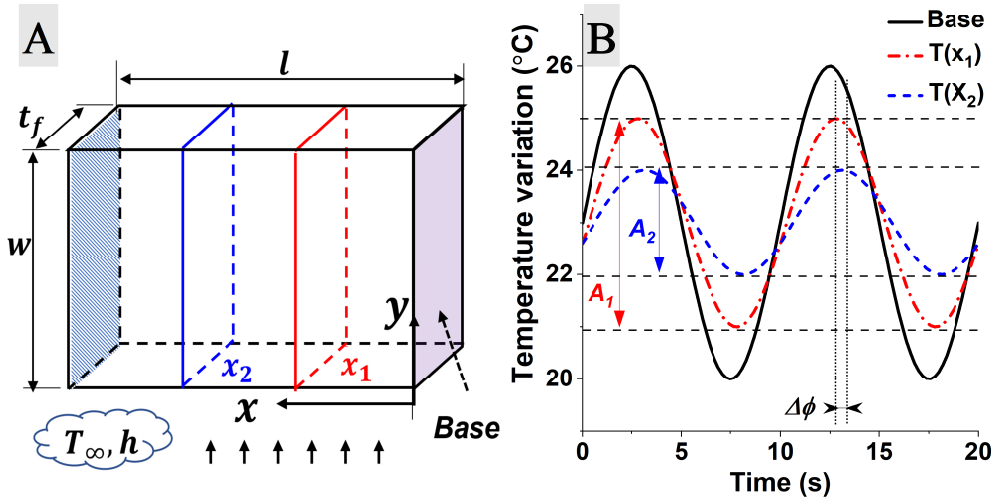

Figure 2.1: (A) Schematic of the transient fin problem. (B) Oscillatory temperature profile at three locations: base, x_1 and x_2 in (A).

The solution to the governing equations derived by Lopez-Baeza et al. [77] follows:

$$T = T_0 \exp(i\omega t)\frac{\cos(\gamma(l-x))}{\cos(\gamma l)} = T_0 \exp(i\omega t) g(\gamma, x) \tag{2.2}$$

$$g(\gamma, x) = \frac{\cos(\gamma(l-x))}{\cos(\gamma l)} \tag{2.3}$$

where γ is the wave vector defined as:

$$\gamma = \left\{ -\frac{h}{rk} + \left[\left(\frac{h}{rk}\right)^2 + \left(\frac{\omega}{2\alpha}\right)^2 \right] \right\}^{1/2} - i \left\{ \frac{h}{rk} + \left[\left(\frac{h}{rk}\right)^2 + \left(\frac{\omega}{2\alpha}\right)^2 \right] \right\}^{1/2} \tag{2.4}$$

Considering the temperature profiles at x_1 and x_2 as shown in Fig. 2.1B, the ratios of temperature amplitudes and phase differences can be computed using

$$\begin{cases} |g(\gamma, x_2 - x_1)| = A_2/A_1 = \Delta A \\ \angle(g(\gamma, x_2 - x_1)) = \phi_2 - \phi_1 = \Delta\phi \end{cases} \tag{2.5}$$

This work employs IR thermography to obtain temperature amplitude ratios and phase differences at multiple locations on a periodically heated sample. A Bayesian framework is then employed to compute thermal diffusivity from amplitude and phase results and to quantify uncertainties.

2.3 Model sensitivity analysis

Ångström's method computes thermal diffusivity (α) using temperature amplitude ratio and phase shift. However, these quantities are also affected by the convective heat transfer coefficient h. In this work, temperature measurements were performed in ambient conditions; therefore, h was difficult to estimate precisely. To enable accurate thermal diffusivity measurements without precise estimation of h, temperature amplitude ratio and phase shift must be more sensitive to α than h. We employed a Monte Carlo [109] method to determine the optimal heating frequency, such that the physical model exhibits high sensitivity to α and low sensitivity to h.

The sample under investigation is a copper foil (ESPI metal, 99.9% purity) of dimension $25.0\,\text{mm} \times 7.0\,\text{mm} \times 76.5\,\mu\text{m}$. We allowed α to vary over a relatively narrow range $[1.0 - 1.2] \times 10^{-4}\,\text{m}^2/\text{s}$ but allowed h to vary over a much wider range $[2 - 20]\,\text{W/m}^2\text{K}$. Then we computed the amplitude ratio and phase shift at the middle of the sample. The analysis was repeated for several different heating frequencies from 0.01 Hz to 1.0 Hz, and the results are shown in Table 2.1.

Table 2.1: Parameter sensitivity at different heating frequencies for copper

Heating frequency (Hz)	$\frac{\text{amplitude sensitivity}(\alpha)}{\text{amplitude sensitivity}(h)}$	$\frac{\text{phase sensitivity}(\alpha)}{\text{phase sensitivity}(h)}$
0.01	0.01	0.32
0.05	0.13	0.32
0.1	1.27	0.34
0.5	19.84	15.30
1.0	65.96	73.78

We note that amplitude ratio and phase shift are more sensitive to α than h at higher periodic heating frequencies. However, at high periodic heating frequencies, thermal penetration depths become small, and the oscillatory temperature profiles are more difficult to measure experimentally. Therefore, in this study, we choose 1.0 Hz as the periodic heating frequency. We plot in Fig. 2.2 the theoretical amplitude ratio and phase shift along the sam-

ple at 1.0 Hz heating frequency for four different combinations of α and h. As demonstrated in Fig. 2.2, amplitude ratio and phase shift are sensitive to α but are insensitive to h.

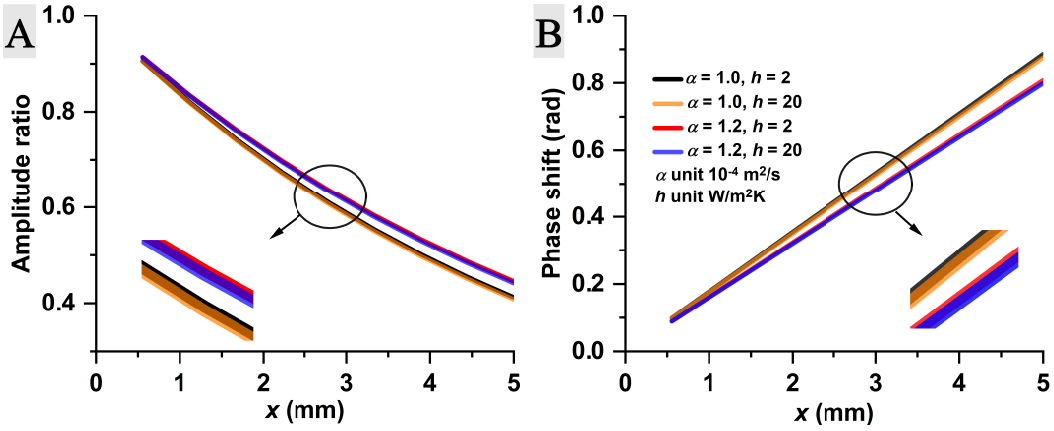

Figure 2.2: Amplitude ratio and phase shift for four extreme cases at 1.0 Hz heating frequency.

2.4 Experimental setup

2.4.1 IR thermography

In this work, the sample under test is a copper foil (ESPI metal, 99.9% purity) of dimension 25.0 mm $\times$ 7.0 mm $\times$ 76.5 μm. A periodic current of 0.5 Hz was supplied through two resistive heating wires (Pelican, 2B2N80ML), creating a 1.0 Hz Joule heating source. One tip of the sample was sandwiched between two heating wires, and the other tip of the sample was sandwiched between two thermally insulating foam strips, as shown in Fig. 2.3A and B. Sample temperatures were recorded with an infrared (IR) camera (Flir A655sc, close-up lens with 25 μm resolution) shown in Fig. 2.3B. A thin layer of flat black paint (carbon black, approx 12 μm thick) was applied on the sample to enhance and normalize surface radiative emissivity for accurate temperature measurements. The emissivity of the paint was calibrated using a precision thermistor (Amphenol: SC30Y103WN, accuracy 100 mK); calibration processes were performed at multiple temperatures between 25 and 50 °C, and the emissivity was approximately constant (0.94) within this temperature range.

Fig. 2.3C includes an IR image of the sample, with the direction of heat propagation indicated by x and the direction perpendicular to x indicated by y. Temperatures were measured where flat black paint was applied. Line A indicates a representative isotherm that is one pixel wide, with the average temperature of all pixels along the line used to represent the temperature at location x. A typical temperature profile on Line A is shown in Fig. 2.3C.

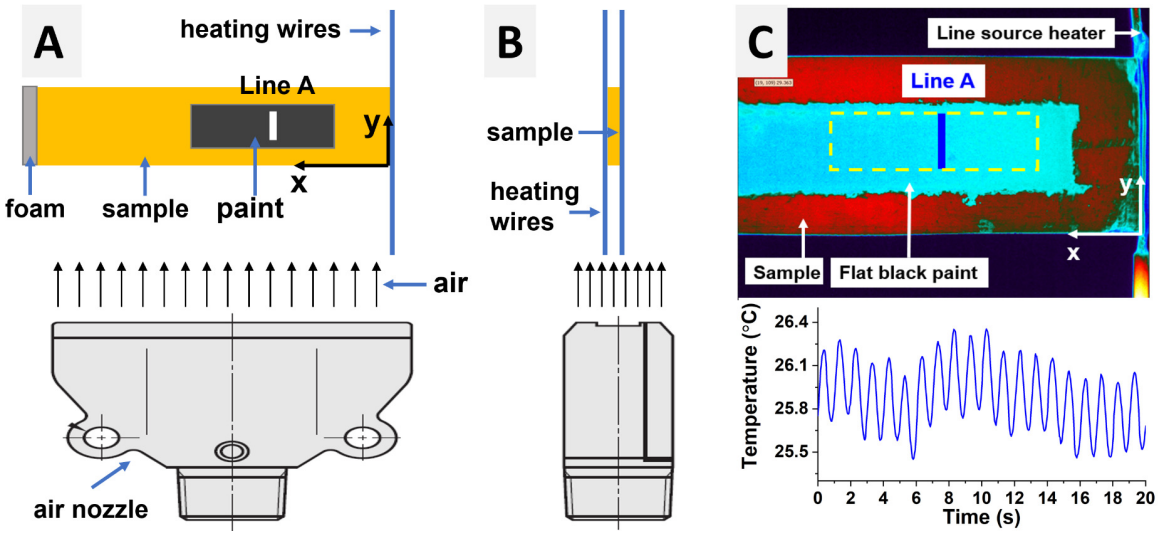

Figure 2.3: (A) Front view of the sample with heating wires, insulated tip and an air nozzle below the sample. (B) Side view of the setup .(C) Infrared image of the sample and an oscillatory temperature profile on a representative isotherm (Line A).

2.4.2 Forced convection on the sample surface

Initially, the sample was exposed to ambient conditions without forced convection. For temperature along Line A shown in Fig. 2.3C, because of ambient temperature fluctuations, relatively strong drift was observed, as shown in Fig. 2.4A. Also, for natural convection, the convective heat transfer coefficient h depends on surface temperature. Therefore, h exhibits relatively large variation along the x direction. We estimate the average convective heat transfer coefficient $\overline{h_y}$ along the x-axis using a correlation for natural convection on an

isothermal plate [91]:

$$\overline{h_y} = \frac{k\overline{Nu_y}}{w} = \frac{4}{3}\left(\frac{Gr_w}{4}\right)^{\frac{1}{4}} \frac{k_{\text{air}}}{w} \frac{0.75Pr^{1/2}}{(0.609 + 1.221Pr^{1/2} + 1.238Pr)^{\frac{1}{4}}} \tag{2.6}$$

where w indicates the sample width. Gr_w is the Grashof number calculated using characteristic length w and the mean temperature along the y-axis. Pr is the Prandtl number of air, k_{air} is the thermal conductivity of air. The results for $\overline{h_y}$ are shown in in Fig. 2.4B, with the blue band indicating the range of variability of $\overline{h_y}$.

To reduce ambient temperature fluctuations and minimize the variation of h along x-axis, we employed forced convection using a flat air nozzle (Misumi, AFTC7) below the sample such that the air flow was perpendicular to the direction of heat conduction, as shown in Fig. 2.3A and 2.3B. The air temperature was stabilized using a heat exchanger that coils the air inlet tube on a stainless steel rod with large thermal mass. We estimate the average convective heat transfer coefficient ($\overline{h_y}$) along the x-axis using a correlation for external flow over an isothermal plate [64]:

$$\overline{h_y} = \frac{\overline{Nu_y}k_{\text{air}}}{w} = \frac{0.664Re^{\frac{1}{2}}Pr^{\frac{1}{3}}k_{\text{air}}}{w} \tag{2.7}$$

where Re indicates the Reynolds number based on the characteristic length of w. Under forced convection, temperature drift was significantly reduced, as shown in Fig. 2.4A. In addition, $\overline{h_y}$ exhibits minimal variation as compared to that under natural convection, as shown in Fig. 2.4B.

Forced convection reduces the variation of h in x direction. However, along the y-axis h is non-uniform because of the growth of thermal boundary layer. We estimated the local convective heat transfer coefficient h_y using a correlation for laminar flow over an isothermal plate [64].

$$h_y = \frac{Nu_y k_{\text{air}}}{y} = \frac{0.332Re^{\frac{1}{2}}Pr^{\frac{1}{3}}k_{\text{air}}}{y} \tag{2.8}$$

The result is shown in Fig. 2.4C and significant variation of h exists near the leading edge. However, for thermally conductive metal films used in this study, the effect of variation in h_y was limited, as temperature measured at different y locations do not exhibit significant differences. More details are provided in the Supplemental Materials.

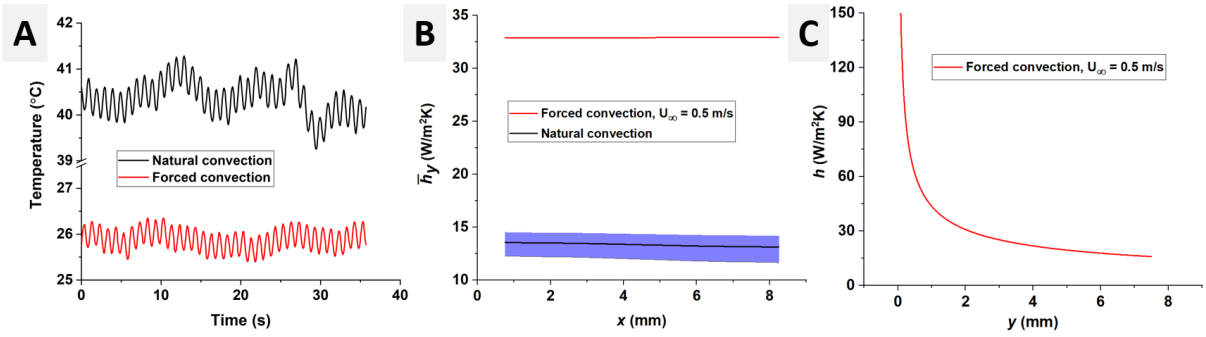

Figure 2.4: (A) Oscillatory temperature profiles for the isotherm shown in Fig 2.3C, with and without forced convection. (B) Average convective heat transfer coefficient $\overline{h_y}$ at different locations along the direction of heat propagation, with and without forced convection. The blue band indicates the range of variation in h. (C) h in the y direction.

2.4.3 IR temperature measurement processing

After obtaining oscillatory temperature profiles on the sample, the next step is to extract amplitudes and phases at different locations to calculate thermal diffusivity (see Eq. 2.5). As shown in previous section, temperature drift can be reduced using forced convection, and Fig. 2.5A includes an oscillatory temperature profile under forced convection. To accurately extract amplitudes and phases from such temperature profile, additional processing are required to minimize the effect of baseline drift. Typically the frequency of the baseline drift is much lower than the periodic heating frequency. Therefore, to mitigate drift, a fifth-order Butterworth high-pass filter [35] with cutoff frequency $f_C = 1/2f_{\text{heating}}$ was applied, where f_{heating} is the Joule heating frequency. The temperature profile after filtering is shown in Fig. 2.5B.

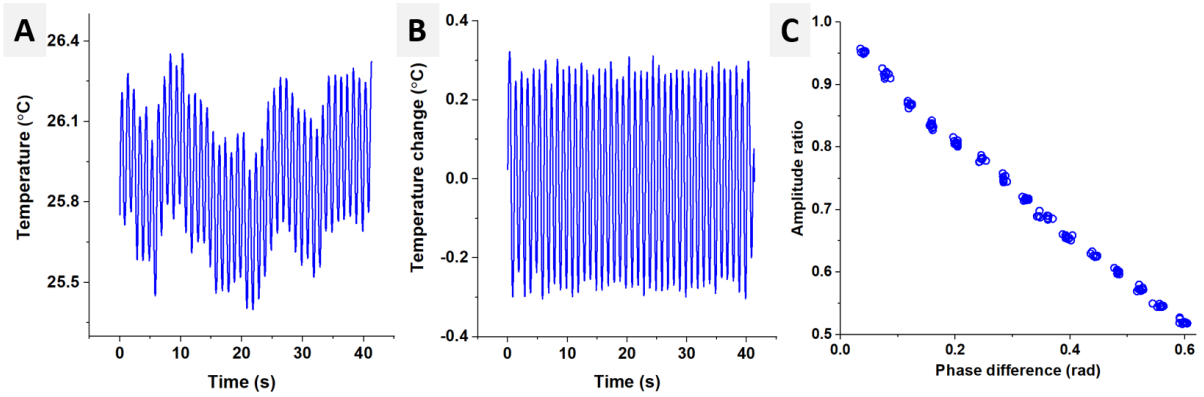

Figure 2.5: (A) A oscillatory temperature profile without filtering under forced convection. (B) The oscillatory temperature profile in (A) after applying a fifth-order Butterworth high--pass filter. (C) Phase differences and amplitude ratios for the region of analysis.

A Fourier transform developed in a previous study [65] was employed to transform the filtered temperature profile to extract the phases $\phi(x,t)$ and amplitudes $A(x,t)$ at location x. The same process was performed for N equally spaced isotherms to obtain amplitudes and phases at those locations. The amplitudes of the temperature profiles were normalized with the amplitude at line 1, which is the isotherm closest to the heat source. Similarly, the phases of the temperature profiles at these locations were subtracted from the phase at line 1 to obtain relative phase differences. The process was repeated for different equally spaced isotherms, and the resulting phase differences and amplitude ratios are shown in Fig. 2.5C. A detailed description of this process is provided in the Supplemental Materials.

2.4.4 Temperature measurement error analysis

We calibrated the sample's emissivity using a thermistor (accuracy 100 mK). As a result, the accuracy of absolute temperature measurement is approximately the same,100 mK. Here, we work with relative temperature changes instead of absolute temperatures, and the changes are relatively insensitive to emissivity [58]. We assume that the true emissivity of the surface is ϵ while the true temperature change due to periodic heating is ΔT. For an estimated emissivity

$\epsilon^{'}$, the relative temperature change $\Delta T^{'}$ that the IR camera measures is approximately [121]:

$$\Delta T^{'} = (\frac{\epsilon}{\epsilon^{'}})^{1/4} \Delta T \tag{2.9}$$

Consequently, errors in emissivity have only small effects on the apparent temperature oscillation amplitude. To demonstrate this assertion experimentally, we obtained a temperature profile on a periodically heated copper strip (Fig. 2.3C line A). The true emissivity of the sample surface is approximately 0.94. However, we assumed the experimentally measured thermal diffusivity emissivity is 0.75 (an exaggerated value) and obtained the corresponding temperature profile for line A. The temperature profiles for the true emissivity and the incorrect emissivity are shown in Fig. 2.6A:

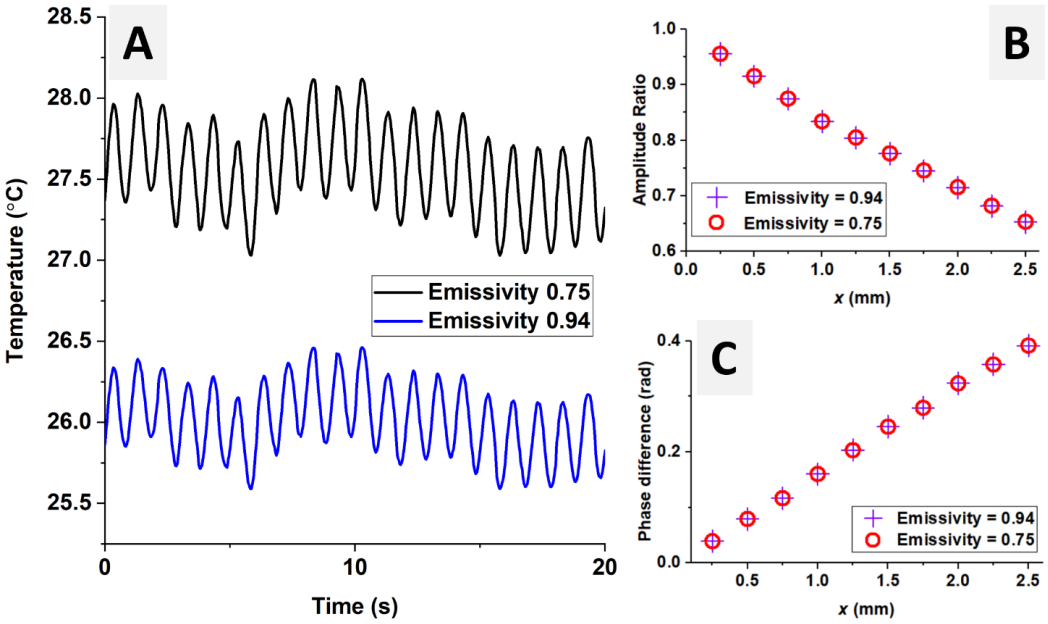

Figure 2.6: (A) Temperature along line A for two different emissivities. (B) Amplitude ratio at different locations on the sample for two different emissivities. (C) Phase shift at different locations on the sample for two different emissivities.

As observed in Fig. 2.6A, the absolute temperature is incorrect due to inaccurate emissivity. However, the amplitude of the oscillation and phase do not exhibit significant changes for different emissivities. We then computed the amplitude ratios and phase shifts in the region

of analysis shown in Fig. 2.3C (yellow rectangle), and the results are shown in Figs. 2.6B and C. As observed, inaccurate emissivity affects amplitude ratio and phase shift results insignificantly.

To conclude, we used a 100 mK thermistor to calibrate emissivity, but the oscillation amplitude and phase shift are insensitive to emissivity. For the IR camera, according to the manufacturer's specification, the thermal sensitivity is 30 mK, which indicates that the minimum detectable temperature change and is much lower than the oscillation amplitude observed in experiments. Therefore, we assume that instrumentation errors do not contribute to errors in amplitude ratio and phase shift results; the errors arise from other random effects, such as temperature drift in ambient environments.

2.5 Uncertainty quantification

Conventional parameter estimation methods often seek to minimize the square error between the physical model and measurement results. However, such approaches do not produce uncertainties for the parameters, and they do not account for prior knowledge of the parameters to reduce uncertainties [46]. In this work, we analyzed uncertainties in thermal diffusivities given measurement results using a Bayesian framework, which incorporates likelihood functions and prior knowledge to produce a complete statistical distribution of parameters. Previous studies have demonstrated the effectiveness of Bayesian framework in inverse heat transfer problems [122][131]. The framework is based on Bayes' theorem:

$$p(\theta|D) = \frac{p(D|\theta)p(\theta)}{p(D)} \tag{2.10}$$

where θ indicates parameters and D is measurement data. $p(\theta|D)$ is the posterior distribution and indicates updated knowledge of θ after observing D. The posterior is proportional to the prior $p(\theta)$ and the likelihood function $p(D|\theta)$. The prior is the state of knowledge of θ before experiments, and the likelihood function is a description of the measurement process and indicates the probability of obtaining the measurement results D given a set of parameters θ. In this work, the noisy phase and amplitude measurement processes are modeled as

bivariate normal distributions with mean μ and covariance matrix Σ. The mean μ is a matrix of theoretical amplitude ratios and phase differences obtained using Eq. 2.5 for a given set of parameters α and h. The covariance matrix is defined as:

$$\Sigma = \begin{pmatrix} \sigma_{\Delta A}^2 & \rho\sigma_{\Delta A}\sigma_{\Delta\phi} \\ \rho\sigma_{\Delta A}\sigma_{\Delta\phi} & \sigma_{\Delta\phi}^2 \end{pmatrix} \tag{2.11}$$

where $\sigma_{\Delta A}$ and $\sigma_{\Delta\phi}$ indicate the standard deviation of amplitude ratio and phase difference measurements, and ρ indicates their correlation coefficient. Considering a temperature ratio and phase difference measurement at x_i, the likelihood function can be expressed as:

$$\begin{aligned} &P\left(\Delta A_i^*, \Delta\phi_i^* \mid \alpha, h, \sigma_{\Delta A}, \sigma_{\Delta\phi}, \rho, x_i\right) \\ &\sim \mathcal{N}\left[\mu = \begin{pmatrix} |g\left(x_i, \alpha, h\right)| \\ \angle\left(g\left(x_i, \alpha, h\right)\right) \end{pmatrix}, \Sigma = \begin{pmatrix} \sigma_{\Delta A}^2 & \rho\sigma_{\Delta A}\sigma_{\Delta\phi} \\ \rho\sigma_{\Delta A}\sigma_{\Delta\phi} & \sigma_{\Delta\phi}^2 \end{pmatrix}\right] \end{aligned} \tag{2.12}$$

where variables with asterisks indicate measurement results. Because $\sigma_{\Delta A}$, $\sigma_{\Delta\phi}$ and ρ are difficult to calculate directly from temperature profiles, they are treated as parameters and are estimated using the Bayesian framework. Here we assume that specific heat and density of the material are known before the experiment; they are treated here as constants without uncertainties.

Once we define the likelihood function for a measurement at x_i, we then consider all measurements ($\Delta A_1 \cdots \Delta A_N$, $\Delta\phi_1 \cdots \Delta\phi_N$) for all locations on the sample. Assuming all measurements are independent, the likelihood function is expressed as:

$$p(\Delta A^*, \Delta\phi^* | \alpha, h, \sigma_{\Delta A}, \sigma_{\Delta\phi}, \rho) = \prod_{i=1}^{N} p(\Delta A_i^*, \Delta\phi_i^* | \alpha, h, \sigma_{\Delta A}, \sigma_{\Delta\phi}, \rho, x_i) \tag{2.13}$$

Having defined the likelihood function, we next consider the prior distributions for the parameters. The sample under test is copper 110, and α is positive and generally less than $10^{-3}\,\mathrm{m}^2/\mathrm{s}$ for common metals. To remove the positive constraint for α, we normalize α with unity value and work with $\log_{10}\alpha$ instead of α. For $\log_{10}\alpha$, its distribution is assumed to be Gaussian, centered at -4 with standard deviation of 1. The prior distribution is designed to be wide enough to cover the true values. Similarly, $\log_{10} h$ with h normalized by 1 $\mathrm{W}/(\mathrm{m}^2)\mathrm{K}$

is used, and its prior distribution is assumed to be Gaussian centered at 1 with standard deviation 1, which is reasonable for common natural and forced convection in air. The prior for $\log_{10}\sigma_{\Delta\alpha}$ and $\log_{10}\sigma_{\Delta\phi}$ are both Gaussian centered at -2 with standard deviation 1. The correlation coefficient ρ is bounded between [-1,1]. In this work, a Fisher transformation [50] is used to transform ρ into an unbounded parameter z. No prior distribution is assigned for ρ.

Based on the likelihood function and the prior distributions, the posterior distribution for parameters is expressed according to Eq. 2.10. Note that parameters α, h ,$\sigma_{\Delta A}$, $\sigma_{\Delta\phi}$, ρ are assumed to be independent:

$$
\begin{aligned}
p(\alpha, h, \sigma_{\Delta A}, \sigma_{\Delta\phi}, \rho|\Delta A^*, \Delta\phi^*) &= \frac{p(\alpha, h, \sigma_{\Delta A}, \sigma_{\Delta\phi}, \rho)\prod_{i=1}^{N} p(\Delta A_i^*, \Delta\phi_i^*|\alpha, h, \sigma_{\Delta A}, \sigma_{\Delta\phi}, \rho, x_i)}{p(\Delta A^*, \Delta\phi^*)} \\
&\sim p(\alpha, h, \sigma_{\Delta A}, \sigma_{\Delta\phi}, \rho)\prod_{i=1}^{N} p(\Delta A_i^*, \Delta\phi_i^*|\alpha, h, \sigma_{\Delta A}, \sigma_{\Delta\phi}, \rho, x_i) \\
&\sim p(\alpha)p(h)p(\sigma_{\Delta A})p(\sigma_{\Delta\phi})p(\rho)\prod_{i=1}^{N} p(\Delta A_i^*, \Delta\phi_i^*|\alpha, h, \sigma_{\Delta A}, \sigma_{\Delta\phi}, \rho, x_i)
\end{aligned}
\tag{2.14}
$$

The main difficulty associated with the Bayesian approach involves obtaining random samples from the posterior distribution. To address this issue, Metropolis et al. [81] developed a Markov chain Monte Carlo method to obtain random samples from an arbitrary distribution up to a normalizing constant. However, the algorithm is computationally expensive and was not widely used until the early 2000s, when computational power significantly increased. In this work, a Metropolis algorithm is employed to sample the unnormalized posterior distribution in Eq. 2.14. To account for reparametrization of the parameters, Jacobians are also included. The pseudo-code for our Metropolis algorithm is shown in Fig. 2.7.

Algorithm 1 Metropolis-Hasting algorithm for posterior sampling

procedure METROPOLIS-HASTING
  $\log \alpha^{'} = \mathcal{N}(\log \alpha, 0.02)$
  $\log h^{'} = \mathcal{N}(\log h, 0.02)$
  $\log \sigma^{'}_{\Delta A} = \mathcal{N}(\log \sigma_{\Delta A}, 0.02)$
  $\log \sigma^{'}_{\Delta \phi} = \mathcal{N}(\log \sigma_{\Delta \phi}, 0.02)$
  $z^{'} = \mathcal{N}(z, 0.02)$
  while $i < N_{\max}$ **do**
    c = U(0,1)
    $\frac{|J^{'}_{\mathrm{h}}|}{|J_{\mathrm{h}}|} = \frac{10^{\log \alpha^{'}} + \log h^{'} + \log \sigma^{'}_{\Delta A} + \log \sigma^{'}_{\Delta \phi}}{10^{\log \alpha + \log h + \log \sigma_{\Delta A} + \log \sigma_{\Delta \phi}}} (\frac{1+e^{z^{'}}}{1+e^{z}})^2 \frac{1+e^{4z^{'}}}{1+e^{4z}}$
    $\beta = \min \left\{ 1, \frac{p(\alpha^{'}, h^{'}, \sigma^{'}_{\Delta A}, \sigma^{'}_{\Delta \phi}, \rho^{'} | \Delta A^{*}, \Delta \phi^{*}) |J^{'}_{\mathrm{h}}|}{p(\alpha, h, \sigma_{\Delta A}, \sigma_{\Delta \Phi}, \rho | \Delta A^{*}, \Delta \phi^{*}) |J_{\mathrm{h}}|} \right\}$
    if $c \leq \beta$ **then**
      accept proposal, $i = i + 1$
    else
      reject proposal

Figure 2.7: The Metropolis algorithm for posterior sampling of the modified Ångström's method.

The Metropolis algorithm was executed in parallel with four Markov chains. The total number of accepted samples in each chain was set to 10000. The total run time of the code was about four hours for each experiment. In each chain, the first 200 samples were discarded, and the rest of the accepted random samples were stored to represent the probability distribution of parameters. Details regarding the diagnostics of the results obtained by our Metropolis algorithm are provided in the Supplemental Materials.

2.6 Results

2.6.1 Thermal Diffusivity Results for Copper 110 Foil

In this work, the Joule heating frequency was 1.0 Hz for all experiments. The pressure of the flat air nozzle was 0.3 psig (2.07 kPa, gauge), and the air velocity was approximately 3.3 m/s [9]. The density of the sample is 8960 kg/m^3, and the specific heat of the sample is 385 J/(kg$\cdot$K) according to the manufacturer's specifications [4]. All experiments were conducted

in a room temperature environment. The number of isothermal lines used here is $N = 135$, and random samples of α and h obtained from the posterior probability distribution function (PPDF) are shown in Fig. 2.8. The PPDF of each parameter indicates the updated state of knowledge based on the prior knowledge of the parameters, measurement processes, and the physical model.

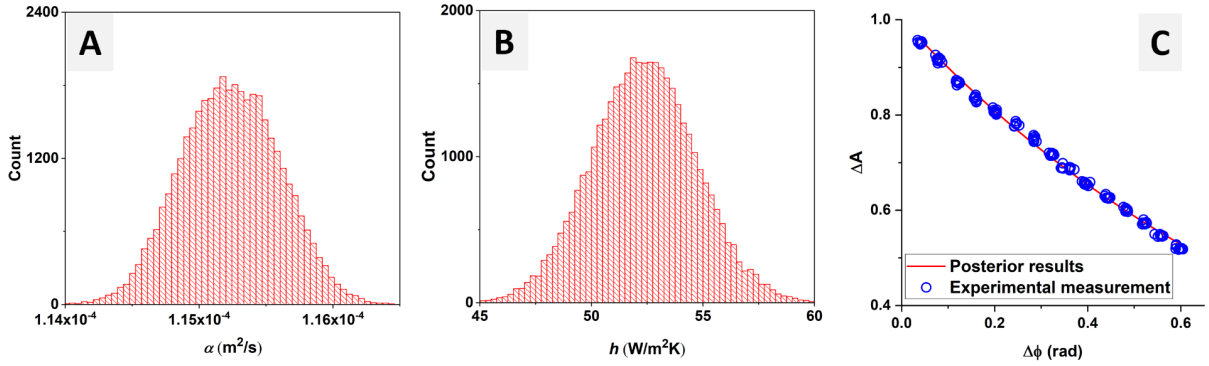

Figure 2.8: (A): Histogram for random samples obtained from the PPDF for thermal diffusivity α. (B) Histogram for random samples obtained from the PPDF for convective heat transfer coefficient h. (C) Experimental measurements (circles) and theoretical model plotted using the posterior mean of α and h (line).

Fig. 2.8A shows the PPDF for thermal diffusivity. The 95% confidence interval (CI) is $\alpha = 1.15 \pm 0.01 \times 10^{-4}\,\mathrm{m}^2/\mathrm{s}$. Our results match with Siddles and Danielson's work ($1.157 \pm 0.014 \times 10^{-4}\,\mathrm{m}^2/\mathrm{s}$) [106], which employed Ångström's method to measure thermal diffusivity for a copper rod (1/8 inch in diameter, 500 mm long) under vacuum. Our results also agree with a more recent study ($1.147 \times 10^{-4}\,\mathrm{m}^2/\mathrm{s}$, $2-5\%$ uncertainty level) using Ångström's method for a copper strip (20 mm wide, 300 mm long) under vacuum [140]. In our study, we achieve comparable accuracy and precision for thermal diffusivity of copper in ambient conditions, and the sample length in this work was much shorter than those used in previous studies. We also compare our results to other commonly used thermal diffusivity measurement methods. The most widely used approach is laser flash. In Parker's work [95], the uncertainty for copper is $\pm 5\%$. For a relatively recent work using laser flash method for copper [83], $\pm 3\%$ uncertainty has been obtained. However, laser flash typically requires

tightly controlled environments to minimize heat loss that are not required in our approach. Another common approach for thermal diffusivity measurement is the transient plane source method [56]. In Gustavsson's work [57], they obtained 0.5% uncertainty for copper. However, their approach makes the semi-infinite heat conduction assumption. As a result, much larger sample size is required for characterization (diameter 60 mm, thickness 2 - 4 mm).

For the convective heat transfer coefficient h, the PPDF is shown in Fig. 2.8B, and the estimated 95% CI is $h = 52 \pm 5\,\mathrm{W/m^2K}$. Based on the experimental conditions ($U_\infty = 3.3\,\mathrm{m/s}$), the estimated average h along the y-axis using Eq. 2.7 is $\overline{h_y} = 85\ \mathrm{W/(m^2/K)}$. The posterior results obtained for h are slightly less than our expectation from the external flow correlation (see Fig. 2.10B), possibly because the actual flat nozzle velocity profiles were non-uniform near the edge of the nozzle [9]. The theoretical model fits well to the experimental results using the posterior mean of α and h, as shown in Fig. 2.8C.

2.6.2 Uncertainty Reduction with Increased Measurements

In this work, the number of isothermal lines used to calculate the posterior distribution is $N = 135$. Here we examine the effect of different N on parameter uncertainties. We arbitrarily selected a certain number ($N = 2$, 15 and 45) of amplitude ratio and phase difference measurements from the entire dataset ($N = 135$) and applied the same procedure to compute the corresponding PPDFs, shown in Fig. 2.9 for α. As the number of measurements increases from 2 to 135, the uncertainties in thermal diffusivity decrease.

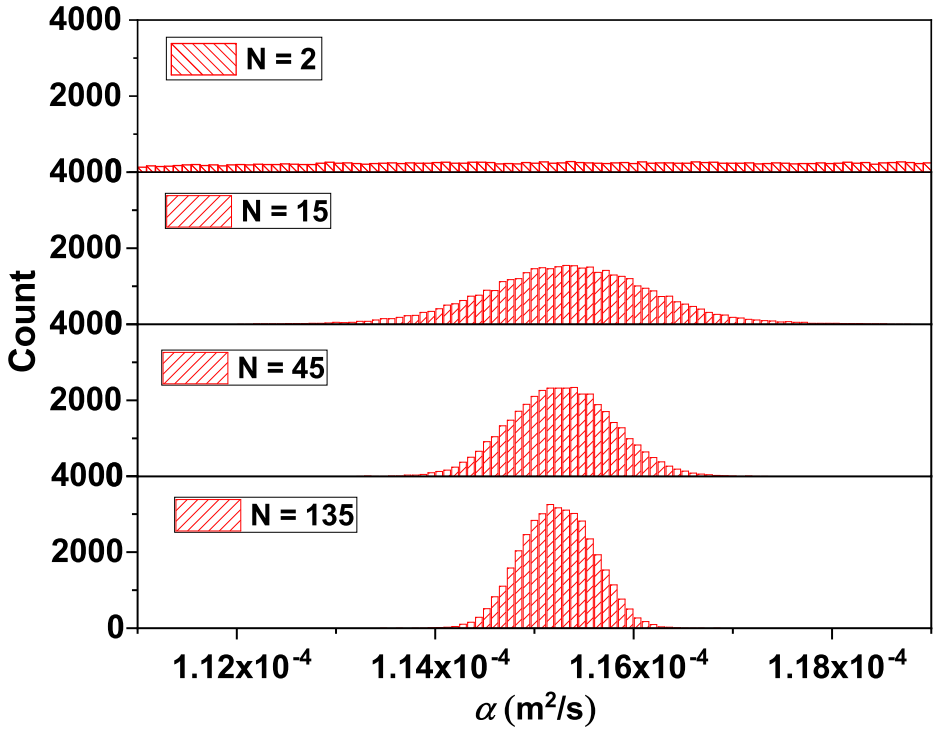

Figure 2.9: The PPDFs for thermal diffusivity for different number of amplitude and phase measurements.

For $N = 2$, temperature amplitude ratios and phase differences were measured only at two locations, yet updated knowledge of all five parameters (α, h, $\sigma_{\Delta A}$, $\sigma_{\Delta\phi}$, ρ) was obtained. This is a major advantage of Bayesian framework as compared to conventional regression methods, such as Levenberg–Marquardt method, which requires the number of measurement results to be greater than the number of estimated parameters in the model [110]. Meanwhile, conventional regression methods do not compute parameter uncertainties, whereas in the Bayesian framework, we are able to reduce uncertainties by increasing the number of measurements.

2.6.3 Effect of Convection on Thermal Diffusivity Measurements

By adjusting the pressure of the flat air nozzle, we repeated the same experiments under different convective conditions, and the results are shown in Fig. 2.10. Under forced convection conditions (nozzle pressure = 0.3, 0.6 psig or 2.07, 4.14 kPa, gauge), the thermal diffusivity measurement results show reasonable accuracy and robustness when the air nozzle pressure changes significantly. Meanwhile, h obtained from the PPDFs qualitatively matches calculations using the external flow correlation given in Eq. 2.7. For natural convection, which corresponds to zero nozzle pressure, h obtained from the PPDF qualitatively matches the correlation for natural convection on a vertical isothermal plate in Eq. 2.6. However, the thermal diffusivity obtained from the PPDF is about 4% less than previous studies, because under natural convection, h is less uniform and constant on the sample, and temperature drift is more significant.

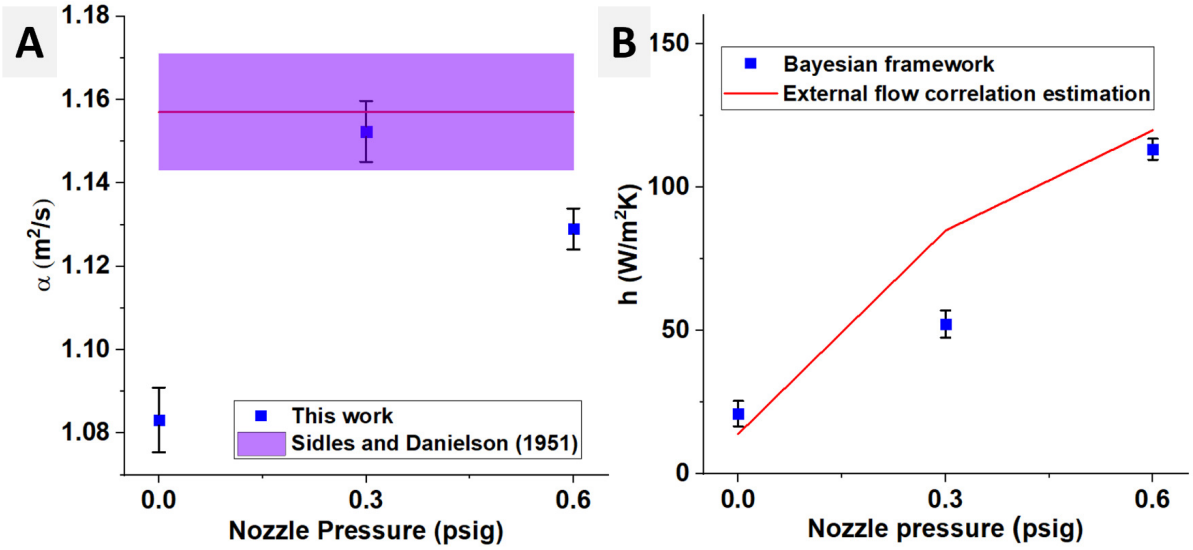

Figure 2.10: (A) Thermal diffusivity α and 95% CI obtained from the PPDF under different nozzle pressures. (B) Convective heat transfer coefficient h and 95% CI obtained from the PPDF under different nozzle pressures.

2.6.4 Effect of prior distribution and fitting residual examination

Here we investigate how the posterior distribution of thermal diffusivity is influenced by the prior distribution of θ (all unknowns) using results obtained under a 0.2 Hz heating frequency. We compute the posterior distribution using a wide ($\sigma_{log\theta} = 2$) and a narrow ($\sigma_{log\theta} = 1$) prior distribution for $log\theta$. The posterior distributions are shown in Fig.2.11.

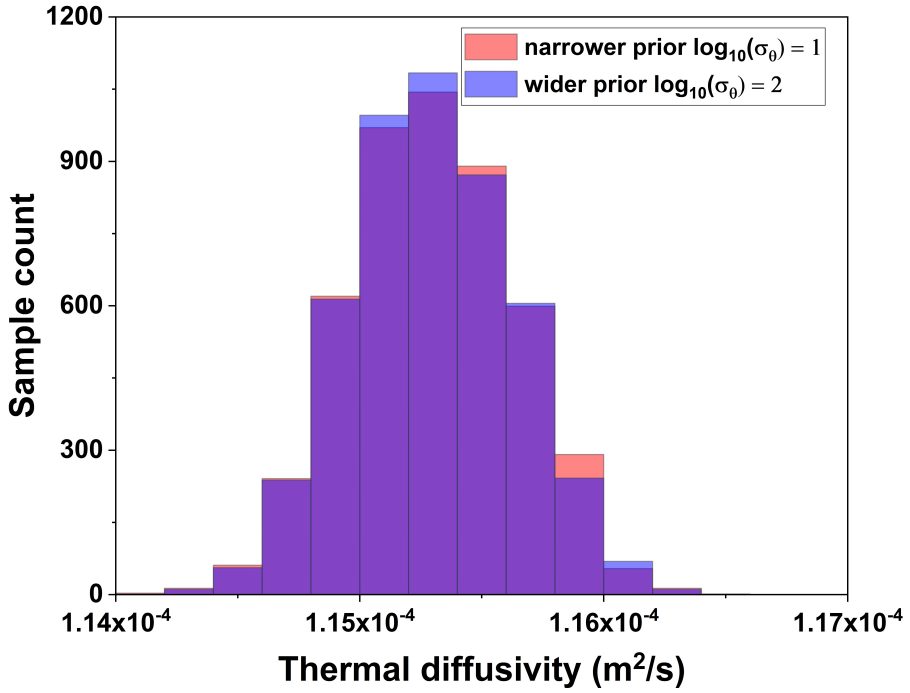

Figure 2.11: Posterior distributions for thermal diffusivity with different prior distributions

As observed, the posterior distributions remain unchanged for different prior distributions. This is expected when the measurement is informative with abundant observations [122][101]. However, prior distributions are not completely unimportant for the Bayesian framework, as they typically serve as regularization for ill-posed inverse problems [122].

In this study we assume that measurements at multiple locations on the sample are independent. We examine this assumption by checking the fitting residuals for amplitude decay and phse shift, as shown in Fig. 2.12.

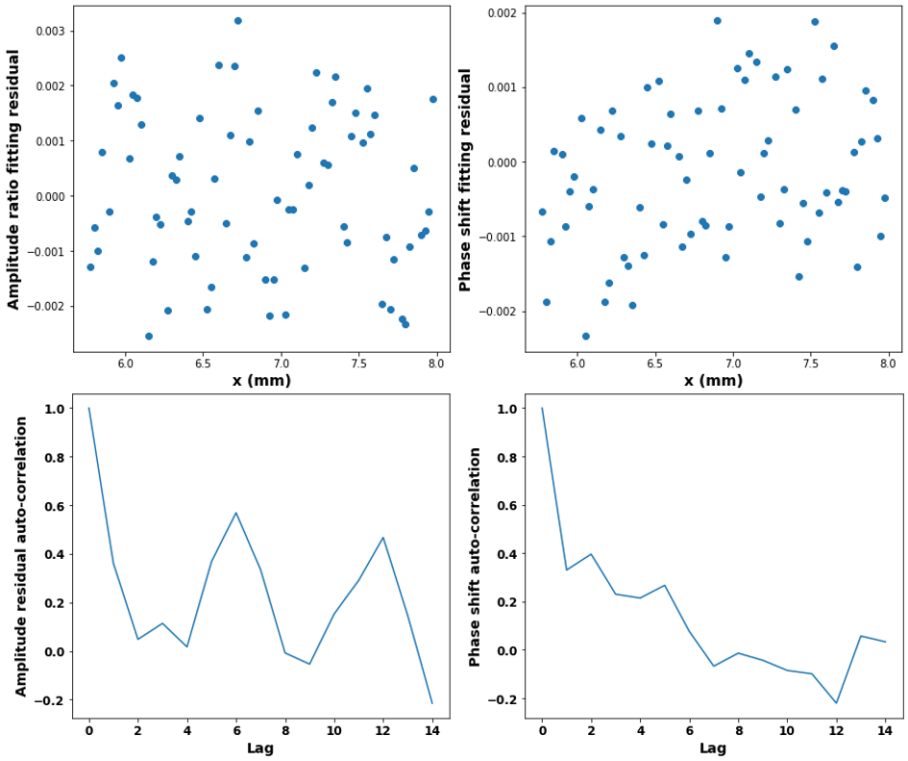

Figure 2.12: Top row: fitting residuals for amplitude decay and phase shift. Bottom row: auto-correlation for the residuals of amplitude decay and phase shift

As observed from the top row in Fig. 2.12, the residual oscillate near zero, which indicates that the analytical solution is accurate to model the underlying physics. The second row shows the auto-correlation for the residual of amplitude decay and phase shift respectively. We observe that majority of the fitting residuals do not exhibit high auto-correlations, and the independent assumption is reasonable to model the measurement process.

2.6.5 Applicability for poor thermal conductors

We have further explored physical limitations of this method for thermal diffusivity measurement by calculating the sensitivity ratio for different ranges of α. We considered a relatively poor thermal conductor (quartz) with the same dimension as the copper strip. We allowed α to vary over a relatively narrow range $[1.3 - 1.5] \times 10^{-6}\,\mathrm{m}^2/\mathrm{s}$ but allowed h to vary over a much wider range $[2 - 20]\,\mathrm{W/m^2K}$; then we repeated the previous analysis, and the results

are shown in Table 2.2.

Table 2.2: Parameter sensitivity at different heating frequencies for quartz

Heating frequency (Hz)	$\frac{\text{amplitude sensitivity}(\alpha)}{\text{amplitude sensitivity}(h)}$	$\frac{\text{phase sensitivity}(\alpha)}{\text{phase sensitivity}(h)}$
0.1	0.12	0.13
0.5	2.97	2.92
1.0	11.97	11.54

We note that with 0.5 Hz heating frequency, amplitude ratio and phase shift are more sensitive to α than h within the defined range. The thermal penetration depth under this heating frequency is [140]:

$$L = \sqrt{\frac{\alpha}{\omega}} = \sqrt{\frac{1.4 \times 10^{-6}\text{m}^2/\text{s}}{0.5\,\text{Hz}}} = 1.7\,\text{mm} \tag{2.15}$$

The temperature profiles within the thermal penetration depth can be resolved using a close-up lens ($25\,\mu$m resolution, 1.7 mm corresponds to 68 pixels).

Next, we considered an even more thermally insulating material, PTFE, with $\alpha = 1.24 \times 10^{-7}\text{m}^2/\text{s}$. We allowed α to vary over a relatively narrow range $[1.1 - 1.3] \times 10^{-7}\,\text{m}^2/\text{s}$ but allowed h to vary over a much wider range $[2 - 20]\,\text{W/m}^2\text{K}$; then we repeated the previous analysis and the results are given in Table 2.3.

Table 2.3: Parameter sensitivity at different heating frequencies for PTFE

Heating frequency (Hz)	$\frac{\text{amplitude sensitivity}(\alpha)}{\text{amplitude sensitivity}(h)}$	$\frac{\text{phase sensitivity}(\alpha)}{\text{phase sensitivity}(h)}$
0.01	0.01	0.01
0.1	0.24	0.24
0.5	5.64	5.62

We note that with 0.5 Hz heating frequency, satisfactory sensitivities can be achieved. However, the thermal penetration depth under this heating frequency is:

$$L = \sqrt{\frac{\alpha}{\omega}} = \sqrt{\frac{1.24 \times 10^{-7}\text{m}^2/\text{s}}{0.5\text{Hz}}} = 0.5\,\text{mm} \tag{2.16}$$

The temperature profiles within the thermal penetration depth are difficult to resolve using the close-up lens. Therefore, lower heating frequency must be used to obtain reliable temperature ratios and phase shifts. As a result, in order to increase the sensitivity in α, h must be tightly controlled (e.g., under vacuum). Therefore, the lowest thermal diffusivity that can be determined using the reported system should be higher than $10^{-7}\,\mathrm{m}^2/\mathrm{s}$.

2.6.6 Effect of film thickness

The theoretical model assumes that temperature is uniform in the through-thickness direction (i.e., the fin approximation). For the copper strip sample used in this study, the fin approximation is valid (approx. 0.2% error compared to the true solution) when the Biot number satisfies the following condition [72],

$$Bi = \frac{hL_c}{k} < 0.01 \tag{2.17}$$

where L_c indicates sample thickness. This condition can be satisfied if the sample is thin. For the highest h we obtained using forced convection (approx. 110 $\mathrm{W/m^2K}$), the maximum thickness is $L_c = 26$ mm and is much greater than the sample thickness.

No theoretical lower limit exists for sample thickness, but the particular experimental setup may introduce some constraints. First, in this study the sample under test was copper, which has a reflective surface with low emissivity. Therefore, a thin layer of flat black paint must be applied to the sample's surface so that temperature can be measured using an infrared camera. In the theoretical model this layer is not considered, and as a result, if the thickness of the sample is comparable to that of the paint (approx. 12 μm), the theoretical model is no longer valid. However, if the material has relatively high emissivity ($\sim$ 0.75), such high emissivity paint is not required. As demonstrated in the foregoing sections, amplitude ratio and phase shift can be accurately detected even if the emissivity is not known precisely. Second, the one-dimensional heat conduction assumption requires the sample to remain straight during measurements. For thin samples, stretching might be required so that the sample does not bend. However, this might introduce unexpected

deformation in the sample and lead to different thermal diffusivity results [75].

To conclude, we believe this approach is feasible for thin samples with relatively high emissivity. However, extra caution should be taken during experiments such that samples do not deform significantly.

2.7 Conclusion

In this work we report a modified Ångström's method for in-plane thermal diffusivity measurements of short, thin-film samples. As compared to previous studies performed under vacuum conditions, temperatures were measured in noisy ambient conditions to demonstrate the robustness and convenience of the method. To quantify and reduce uncertainties caused by temperature fluctuations, we employed a Bayesian framework with a Metropolis algorithm for data analysis. We verified the accuracy of the system using a short copper 110 thin film (25.0 mm$\times$ 7.0 mm$\times$ 76.5 μm), and demonstrated uncertainty reduction with increased number of measurements. The application of Bayesian inference in this work provides rigorous uncertainty quantification with demonstrated low uncertainty for Ångström's method. We expect that this general approach will be applicable to other situations, such as at high-temperature environments [14], in which the realization of a tightly controlled thermal environment for property evaluation is impractical.

CHAPTER 3

High-temperature thermal diffusivity characterizations using a modified Ångström's method with transient infrared thermography

3.1 Physical system modeling

Existing Ångström's methods for high temperature characterization employ linearized radiation loss models[106][13][42][60]. These methods can be accurate if the sample's temperature T remains uniform along the direction of heat conduction and if the temperature oscillation amplitude is negligible compare to T. In this work, a thin disk sample (88.50 mm OD) is partially heated using a concentrated light source and relatively significant temperature gradient exists along the heat conduction direction. Therefore, radiation losses can not be linearized, and we instead develop a numerical solution to account for non-linear radiation loss.

The schematic of our system is shown in Fig. 3.2A. The concentrated light source is a 10 kW Xenon short arc lamp with Lorentzian intensity distribution[53][14]. The power of the concentrated light source is controlled using a 0-10 V external control voltage. The heat flux of the light source is given as:

$$q_s^{"}(r,V) = \frac{A(V)}{\pi}\frac{\sigma_{solar}}{\sigma_{solar}^2 + r^2} \tag{3.1}$$

where $A(V)$ is nominal peak heat flux and is determined by the control voltage V, and σ_{solar} indicates the width of the distribution and is determined by the reflector of the light source and is relatively independent of V; r is the radius on the sample. We use a function generator

to produce sinusoidal voltage signals to control the light source to output periodic heat flux. Details for characterizing and modeling the light source are provided in the Supplemental Materials S1.

In our study the concentrated light source is partially blocked by three annular tungsten rings (referred to as light blockers) so that only the center of the sample is exposed to the light source. A custom tray tracing code[14] was employed to evaluate the intensity distribution of the concentrated light source as truncated by the light blockers. The simulated intensities with and without truncation are shown in Fig. 3.1B. A window function, defined by the ratio of intensities with and without light blocker are shown in Fig. 3.1C. As shown by the the window function, the light blockers only affect the intensity distribution near the inner edge of the light blocker. The window function in Fig. 3.1C shows the simulated truncated intensity distribution with the light blockers.

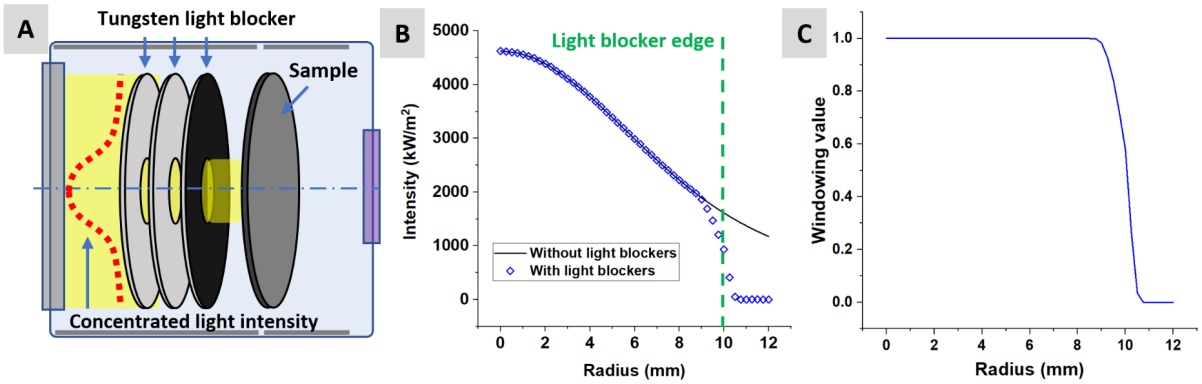

Figure 3.1: (A) Schematic of the experimental system for thermal diffusivity characterization. (B) Ray tracing study for intensity distribution of the concentrated light source with and without light blockers. (C) A window function to model the truncated Lorentzian intensity distribution.

Having introduced the concentrated light source, we present a finite difference solver for the transient heating process, under the following assumptions to simplify the analysis:

1. Fin approximation for the thin disk samples.

2. All surfaces are gray and diffuse.

3. Thermal expansion of the sample is not considered.

4. Heat loss via conduction and convection are neglected.

5. To facilitate IR thermography, a thin layer of high-emissivity coating was applied to the back side of the sample. This layer contributes approx. 2% to the total sample mass and is not considered in the model.

6. We use the following expression[104][82][12] for temperature-dependent thermal diffusivity:

$$\alpha(T) = \frac{1}{A_\alpha \times T + B_\alpha} \tag{3.2}$$

A schematic of the finite difference network is shown in Fig. 3.2A along with a control volume (dashed green box) for a node m at time step p.

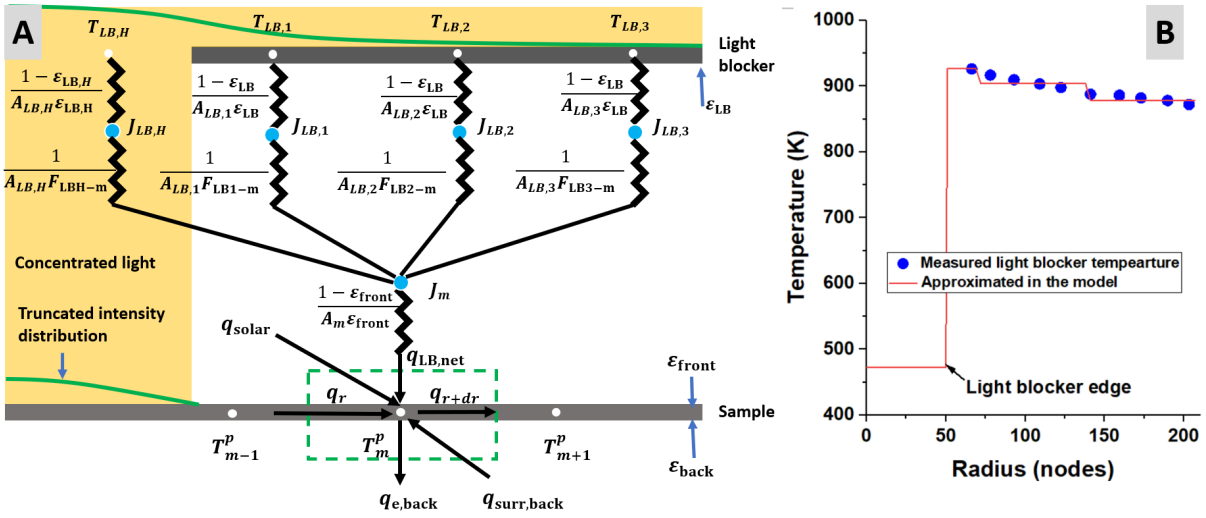

Figure 3.2: Finite difference scheme for the transient heating process with the radiation network. The green dashed rectangular box indicates a control volume for node m on the sample at time step p.

Applying conservation of energy to the control volume shown in Fig. 3.2A we obtain:

$$q_r - q_{r+dr} + q_{solar} + q_{lb,net} - q_{e,back} + q_{surr,back} = \dot{E} \tag{3.3}$$

where q_r and q_{r+dr} indicate heat transfer via conduction, expressed as:

$$q_r = r\, d\theta\, dz\, q_r^{"}\,, \text{where } q_r^{"} = -k\frac{\partial T}{\partial r} \tag{3.4}$$

$$q_{r+dr} = q_r + \frac{\partial q_r}{\partial r}dr = q_r - \frac{\partial(r\, d\theta\, dz\, k\, \frac{\partial T}{\partial r})}{\partial r}dr \tag{3.5}$$

q_{solar} indicates energy absorbed from the concentrate light source:

$$q_{solar} = \eta\, q_s^{"}\, d\theta\, r\, dr \tag{3.6}$$

where η indicates sample absorptivity from the concentrated light source, and $q_s^{"}$ is given in Eq. 3.1.

The net heat flow between the light blocker and the sample, $q_{lb,net}$, is calculated using a radiation network as shown in Fig. 3.2A. Based on experimental observations (see Supplemental Materials S3 for light blocker temperature measurements), the temperature gradient of the light blocker along the radial direction is typically low (approx. 50K). Therefore, we use three discrete constant temperatures to approximate the light blocker temperature distribution in different regions as shown in Fig. 3.2B. We assign $T_{lb,1}$ as the temperature between radius $R_{lb,H}$ and $R_{lb}/3$, where $R_{lb,H}$ is the radius of the light blocker's hole and R_{lb} is the radius of the light blocker. Similarly we assign $T_{lb,2}$, $T_{lb,3}$ and $T_{lb,H}$ for the region bounded by $R_{lb}/3$ to $2R_{lb}/3$, $2R_{lb}/3$ to R_{lb} and 0 to $R_{lb,H}$, respectively. $q_{lb,net}$ is expressed as:

$$\begin{aligned} q_{lb,net} =& \frac{\sigma T_{lb1}^{p4} - T_m^{p4}}{\frac{1-\epsilon_s}{\epsilon_s A_m} + \frac{1}{A_{lb1} F_{lb1-m}} + \frac{1-\epsilon_{lb}}{\epsilon_{lb} A_{lb1}}} + \frac{\sigma T_{lb2}^{p4} - T_m^{p4}}{\frac{1-\epsilon_s}{\epsilon_s A_m} + \frac{1}{A_{lb2} F_{lb2-m}} + \frac{1-\epsilon_{lb}}{\epsilon_{lb} A_{lb2}}} \\ &+ \frac{\sigma T_{lb3}^{p4} - T_m^{p4}}{\frac{1-\epsilon_s}{\epsilon_s A_m} + \frac{1}{A_{lb3} F_{lb3-m}} + \frac{1-\epsilon_{lb}}{\epsilon_{lb} A_{lb3}}} + \frac{\sigma T_{lbH}^{p4} - T_m^{p4}}{\frac{1-\epsilon_s}{\epsilon_s A_m} + \frac{1}{A_{lbH} F_{lbH-m}} + \frac{1-\epsilon_{lb}}{\epsilon_{lb} A_{lbH}}} \\ &= q_{m,lb} - C_{m,lb}\, \sigma\, T_m^{p4} \end{aligned} \tag{3.7}$$

where σ is the Stefan-Boltzmann constant; ϵ_{lb} is the emissivity of the light blocker; and ϵ_{front} is the emissivity of the front side of the sample. A_{lbH}, A_{lb1}, A_{lb2} and A_{lb3} are the light blocker areas corresponding to discrete temperatures T_{lbH}, T_{lb1}, T_{lb2} and T_{lb3} respectively. F_{lbH-m}, F_{lb1-m}, F_{lb2-m}, F_{lb3-m} are view factors from A_{lbH}, A_{lb1}, A_{lb2} and A_{lb3} to the differential ring

element at node m. $C_{m,lb}$ and $q_{m,lb}$ are expressed as:

$$\begin{aligned} C_{lb,m} =& \frac{1}{\frac{1-\epsilon_s}{\epsilon_s A_m} + \frac{1}{A_{lb1} F_{lb1-m}} + \frac{1-\epsilon_{lb}}{\epsilon_{lb} A_{lb1}}} + \frac{1}{\frac{1-\epsilon_s}{\epsilon_s A_m} + \frac{1}{A_{lb2} F_{lb2-m}} + \frac{1-\epsilon_{lb}}{\epsilon_{lb} A_{lb2}}} \\ &+ \frac{1}{\frac{1-\epsilon_s}{\epsilon_s A_m} + \frac{1}{A_{lb3} F_{lb3-m}} + \frac{1-\epsilon_{lb}}{\epsilon_{lb} A_{lb3}}} + \frac{1}{\frac{1-\epsilon_s}{\epsilon_s A_m} + \frac{1}{A_{lbH} F_{lbH-m}} + \frac{1-\epsilon_{lb}}{\epsilon_{lb} A_{lbH}}} \end{aligned} \tag{3.8}$$

$$\begin{aligned} q_{lb,m} =& \frac{\sigma T_{lb1}^{p4}}{\frac{1-\epsilon_s}{\epsilon_s A_m} + \frac{1}{A_{lb1} F_{lb1-m}} + \frac{1-\epsilon_{lb}}{\epsilon_{lb} A_{lb1}}} + \frac{\sigma T_{lb2}^{p4}}{\frac{1-\epsilon_s}{\epsilon_s A_m} + \frac{1}{A_{lb2} F_{lb2-m}} + \frac{1-\epsilon_{lb}}{\epsilon_{lb} A_{lb2}}} \\ &+ \frac{\sigma T_{lb3}^{p4}}{\frac{1-\epsilon_s}{\epsilon_s A_m} + \frac{1}{A_{lb3} F_{lb3-m}} + \frac{1-\epsilon_{lb}}{\epsilon_{lb} A_{lb3}}} + \frac{\sigma T_{lb4}^{p4}}{\frac{1-\epsilon_s}{\epsilon_s A_m} + \frac{1}{A_{lbH} F_{lbH-m}} + \frac{1-\epsilon_{lb}}{\epsilon_{lb} A_{lbH}}} \end{aligned} \tag{3.9}$$

$q_{e,back}$ indicates radiation loss at the back side of the sample:

$$q_{e,back} = \epsilon_{back}\, \sigma\, T^4\, d\theta\, r\, dr \tag{3.10}$$

where ϵ_{back} is the emissivity of the back side of the sample.

$q_{surr,back}$ indicates the rate of radiation absorbed by the back side of the sample. We assume the surrounding temperature in the vacuum chamber at the back side of the sample is constant. Therefore, $q_{surr,back}$ is also a constant. More details for calculating $q_{surr,back}$ are provided in the supplemental material S1.

The energy accumulation term $\dot{E}$ is expressed as:

$$\dot{E} = d\theta\, r\, dr\, dz\, \rho\, c_p\, \frac{\partial T}{\partial t} \tag{3.11}$$

Substitution of Eqs. 3.4-3.11 into the governing equation Eq. 3.3 yields:

$$\frac{\partial}{\partial r}\left(k\frac{\partial T}{\partial r}\right) + \frac{1}{r}\left(k\frac{\partial T}{\partial r}\right) + \frac{q_s^{"}}{dz} - \frac{(\epsilon_{back} + C_{lb,m}/(d\theta\, r\, dr))\sigma\, T^4}{dz} + \frac{q_{lb,m} + q_{surr,back}}{r\, dr\, d\theta\, dz} = \rho\, c_p \frac{\partial T}{\partial t} \tag{3.12}$$

The initial (IC) and the boundary (BC) conditions are:

$$\begin{cases} \text{IC: } t = 0,\ T(x,0) = T_i & \text{(3.13a)} \\ \text{BC: } r = R,\ -k\dfrac{\partial T}{\partial r} = \sigma(\epsilon T^4 - \eta\, T_W^4) & \text{(3.13b)} \\ \text{has to satisfy: } \dfrac{\partial T}{\partial r}|_{r=0} = 0 & \text{(3.13c)} \end{cases}$$

where T_W indicates the temperature of the vacuum chamber wall. Eq. 3.12 is discretized using a central-difference implicit finite difference scheme. A detailed discussion of the finite difference scheme and the implicit Newton-Raphson solver are given in the supplemental material S2. A mesh independence analysis has been performed to ensure the convergence of the numerical solution (see Supplemental Materials S2). The total number of nodes along the radial direction is 220, and the model form error is neglected in this study.

Having obtained the simulated temperature profiles, we next extract amplitude and phase from the simulation results. First, we choose a reference radius R_0 that is close to the inner diameter of the light blocker but not irradiated by the concentrated light source. We also choose a region of analysis bounded by the reference radius R_0 and an outer bound R_N, in which significant amplitude decay is observed. Our code automatically detects quasi steady-state oscillation when the maximum mean temperature rise within one cycle is less than 0.1% compared to the oscillation amplitude, as shown in Fig. 3.3A. Amplitude decay and phase shift for all nodes are calculated with respect to the temperature profile at the reference radius. Representative amplitude decay and phase shift plots are shown in Fig. 3.3B and 3.3C respectively.

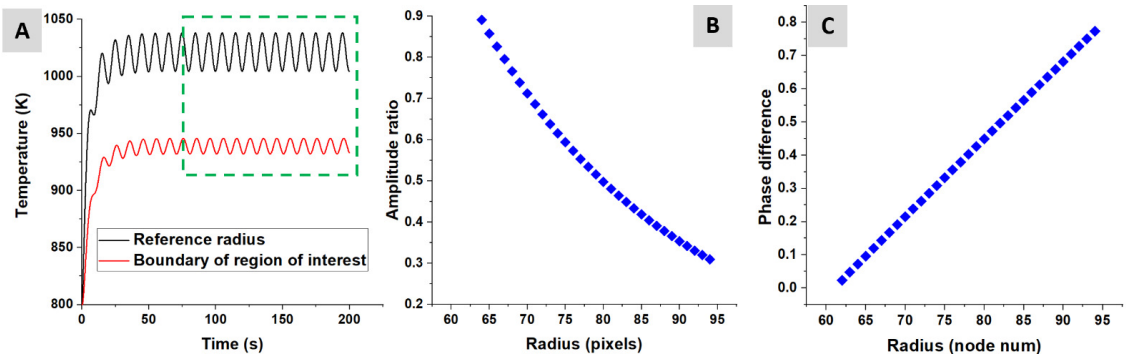

Figure 3.3: (A) Simulated temperature profile at the reference radius and the boundary of the region of analysis. (B) Amplitude decay of temperature profiles within the region of analysis. (C) Phase shift of temperature profiles within the region of analysis.

3.2 Experimental techniques

3.2.1 Experimental setup

In this work, the samples under test are thin disks (graphite: 0.92 mm, copper: 0.79 mm) with 88.50 mm outer diameter. Measurements were conducted under vacuum, and the vacuum level was approx. 0.05 Torr. The heat source is a 10 kW Xenon short arc lamp (Superior: SQP-SX10000FXT), and an electroformed parabolic reflector (Optiforms, Ag coated) concentrates the light. The inner diameter of the light blockers is 20.0 mm, and the distance between neighboring light blockers is 0.90 mm. A sample holder is designed to hold the light blockers and the sample concentrically as shown in Fig. 3.4A. The sample is fixed to the sample holder using four pairs of small thermally insulating ceramic washers to minimize heat losses via conduction. The distance between the sample and the neighboring light blocker is 1.60 mm. We use three light blockers so that temperature oscillation on the last light blocker is minimal. The last light blocker facing the sample is coated with a thin layer of high-emissivity coating (Aremco 840CMX) to reduce radiative reflection from the sample and enable temperature measurements using IR themography. We use an IR camera (Flir A655sc, calibrated to 2000 °C) for temperature measurements. A schematic of the system is shown in Fig. 3.4B, and a photograph of the system is shown in Fig. 3.4C.

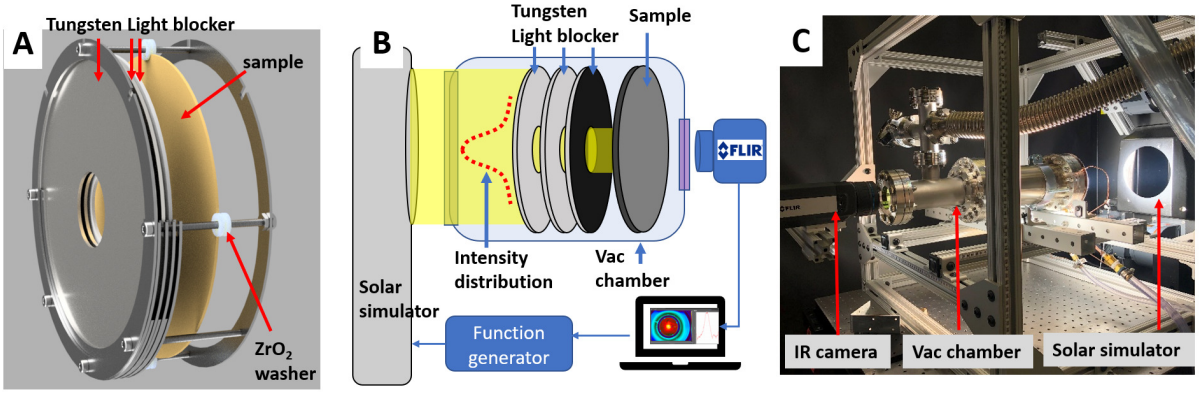

Figure 3.4: (A) Tungsten light blockers and the sample holder for measurements. (B) Schematic of the system. (C) a photograph of the system.

The concentrated light source is powered by a 3-phase power supply with fixed 110 V with programmable current ranging from 100 to 200 A. The operating current is controlled externally using a 0-10 V function generator. Within the range of operation, the concentrated light source exhibits a linear relationship between external control voltage and the operating current. To heat the sample to high temperatures, we first control the solar simulator to produce steady heat flux. Upon reaching steady temperature (typically in 10 min), we modulate the function generator to output biased sinusoidal control voltage signals. Because of the linear relationship between external control voltage and the operating current, the concentrated light source also outputs biased sinusoidal heat flux. When the system reaches quasi steady-state oscillation (approx.1 min after introducing the oscillating heat flux), we start recording the temperature profiles using the IR camera.

3.2.2 IR thermography and processing

To facilitate IR thermography, the back side of the sample is coated with a thin layer of high-emissivity coating (Aremco, 840MX). Our IR camera uses uncooled microbolometer detector with spectral range between 7.5-14 μm. From the spectral emissivity of the coating between 7.5-14 μm[2], we estimated the total emissivity in the IR camera's range is between 0.88 and 0.92. Because the coating's spectral emissivity is relatively independent of temperature, we measured its emissivity using a thermocouple (type K, $\pm$0.75% accuracy) and the IR camera at relatively lower temperatures (370 °C), and the emissivity was 0.92. Therefore, we use 0.92 as the sample's emissivity for IR measurement. The temperature measurement error for the IR camera is approx. $\pm$2%[5].

Because of symmetry, the isothermal lines in the IR image are concentric circles, as shown in Fig. 3.5A. At steady state, temperature measured for a pixel located at R_0 exhibits much stronger noise in a high temperature environment as compared to a room temperature condition, as illustrated in Fig. 3.5B. To reduce high random noise, we developed a computationally efficient method using bi-linear interpolation to obtain the average temperature at a given radius. The averaged temperature profiles at two representative locations R_0 and R_N

are shown in Fig. 3.5C. Details of the IR image processing are available in the supplemental material S4. We employ a parallel approach to average all the IR images in a recorded video, and the time required to fully process an IR recording consists of 500 images is less than one minute.

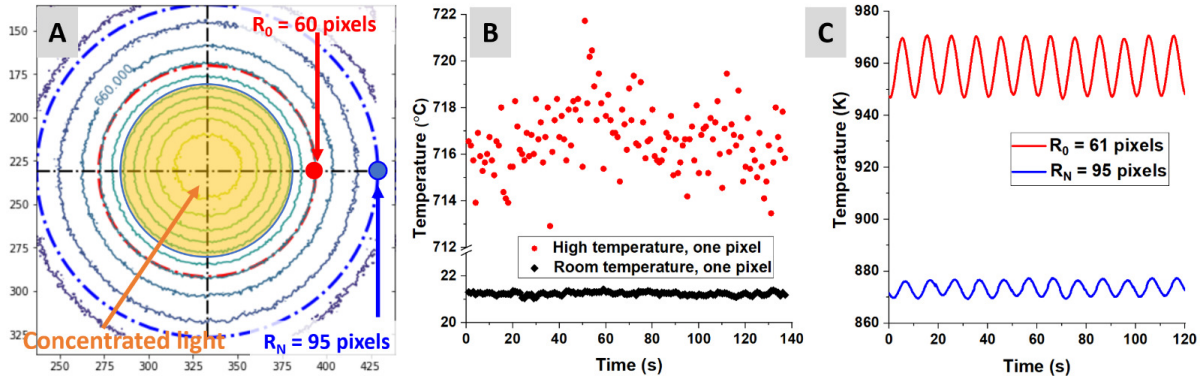

Figure 3.5: (A) Temperature contour plot of a sample. The area exposed to the concentrated light source is indicated by the yellow circle. (B) Steady temperature profile at pixel R_0 at room and high temperatures. (C) Averaged temperature profile at two representative radii R_0 and R_N.

Having obtained averaged temperature profiles at different radii, we extract amplitude decay and phase shift with respect to the reference radius R_0. We employ a Fourier transform to calculate amplitude decay and phase shift for two sinusoidal temperature signals[65]. The main benefit of working with amplitude decay and phase shift instead of absolute temperature is the robustness against emissivity[120][58][67]. For the high-emissivity coating, a slight variation of the emissivity setting in the IR camera from 0.92 to 0.88 causes approx. 20 K difference in absolute temperature, as shown in Fig. 3.6A. Because emissivity affects only absolute temperature and does not change the shape of the oscillating temperature profiles, intuitively, the phase of a sinusoidal temperature profile is not affected by the emissivity setting in the IR camera. Therefore, phase difference can be accurately measured even if emissivity is not known precisely, as shown in Fig. 3.6B.

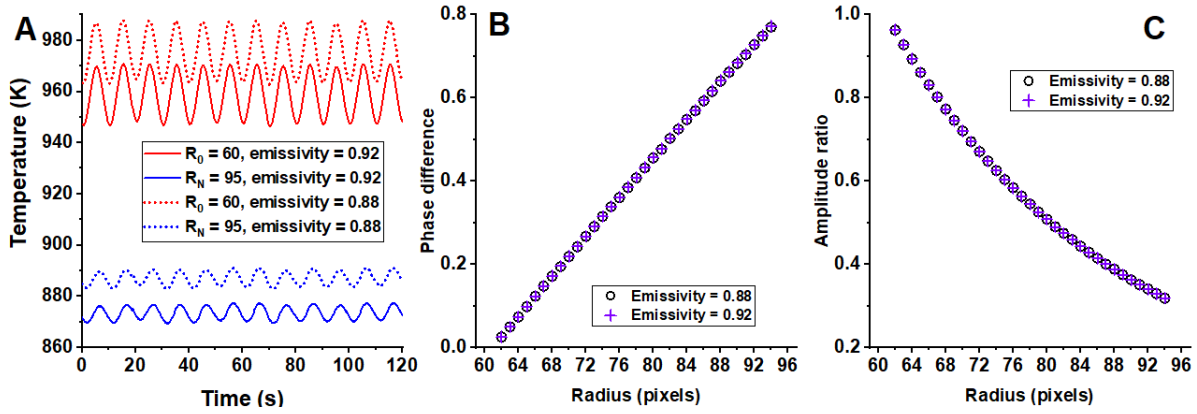

Figure 3.6: (A) Temperature profiles measured at R_0 and R_N using different emissivity settings. (B) Phase difference calculated using temperature profiles between R_0 and R_N under different emissivity settings. (C) Amplitude decay calculated using temperature profiles between R_0 and R_N under different emissivity settings.

For amplitude decay, we consider arbitrary locations R_x on the sample. If we neglect the effect of the surroundings, the radiation measured by the IR camera is proportional to the radiation emission at R_x. We denote the true emissivity at R_x as ϵ and true temperature as T_x, whereas the emissivity setting in the IR camera is $\epsilon^{'}$ and the corresponding measured temperature is $T_x^{'}$. The following equation assumes that the IR camera measures radiance correctly:

$$\sigma\epsilon^{'}T_x^{'4} = \sigma\epsilon T_x^4 \tag{3.14}$$

Because of oscillating heat flux, the true peak-to-valley temperature change is ΔT, and the temperature change observed in the IR camera is $\Delta T^{'}$. Considering two locations on the sample R_0 and R_x, and based on Eq. 3.14, we obtain the following relationships:

$$\begin{cases} \sigma\epsilon^{'}(T_0^{'} + \Delta T_0^{'})^4 = \sigma\epsilon(T_0 + \Delta T_0)^4 & \text{(3.15a)} \\ \sigma\epsilon^{'}(T_x^{'} + \Delta T_x^{'})^4 = \sigma\epsilon(T_x + \Delta T_x)^4 & \text{(3.15b)} \end{cases}$$

The amplitude decay can be expressed as:

$$\frac{\Delta T_x^{'}}{\Delta T_0^{'}} = \frac{\gamma(T_x + \Delta T_x) - T_x^{'}}{\gamma(T_0 + \Delta T_0) - T_0^{'}} \tag{3.16}$$

where $\gamma = (\epsilon/\epsilon^{'})^{1/4}$. Based on Eq. 3.14, we also have:

$$\sigma\epsilon^{'}(T_0^{'})^4 = \sigma\epsilon(T_0)^4,\ T_0^{'} = \gamma T_0 \tag{3.17}$$

As a result, γ cancels, and the ratio of oscillation amplitude shows no dependence on emissivity. Fig. 3.6C shows that amplitude decay extracted from temperature profiles does not depend on emissivity.

$$\frac{\Delta T_x^{'}}{\Delta T_0^{'}} = \frac{\Delta T_x}{\Delta T_0} \tag{3.18}$$

To summarize, the averaging of the IR image over the radius significantly reduces random noise in the high-temperature environment. The averaging approach is computationally efficient and requires less than 1 min to process an IR recording typically consisting of 500 IR images. We demonstrate that amplitude decay and phase shift extracted from measured temperature profiles are not affected by errors in emissivity, and therefore we work with amplitude decay and phase shift instead of absolute temperature profiles.

3.3 Model sensitivity analysis

In this study, we employ a full factorial design of experiments at two levels[85] to investigate the sensitivity of the physical model output (amplitude decay and phase shift) to the parameter of interest (thermal diffusivity). Here we use graphite's properties for demonstration. In addition to the parameter of interest, we are uncertain about several others. First, the intensity distribution of the concentrated light source is difficult to characterize precisely. Based on a previous study for a similar concentrated light source[14] and our preliminary investigation using a calorimetry method, the estimated intensity distribution width (σ_{solar}) is 0.01 m. We assume a $\pm 30\%$ variation associated with σ_{solar}. Secondly, in our study the light blocker temperature T_0 is difficult to measure precisely. We assume a $\pm 5\%$ variation associated with T_0 and assume the light blocker temperature is uniform and constant for sensitivity analysis. Lastly, we treat thermal diffusivity as a temperature-independent parameter for sensitivity analysis. For a typical graphite sample the estimated thermal diffusivity α at 1000 K is $2.2 \times 10^{-5}\,\mathrm{m}^2/\mathrm{s}$. We assigned a relatively low range of variation ($\pm 5\%$) for α.

Table 3.1 shows a summary of these parameters and the corresponding range of variations.

Table 3.1: Parameters for a two level full factorial design of experiment

Parameter	Definition	Range
α	Thermal diffusivity	(2.09,2.31) $\times 10^{-5}$m^2/s, 5% variation
σ_{solar}	Light source intensity distribution	(0.7,1.3)$\times 10^{-2}$ m, 30% variation
T_0	Light blocker temperature	(950, 1050) K, 5% variation

We employ a main effect approach [85] to quantify model output sensitivity to an input parameter θ. For a two-level design, the main effect $ME(\theta)$ is expressed as:

$$ME(\theta) = \frac{1}{2}\left(f(\theta+) - f(\theta-)\right) \tag{3.19}$$

where f indicates the model, and $\theta+$ and $\theta-$ indicate the model at 'high' and 'low' parameter values. We evaluate the main effect of parameters defined in Table 3.1 to understand how model outputs (amplitude decay and phase shift) are influenced by input parameter changes. We choose an area ($R_0 = 60$ pixels with 12 pixels span) that is not irradiated by the concentrated light for amplitude and phase calculations. This area is chosen because of high signal-to-noise ratio based on experimental observation. A prior study showed that increased heating frequency is beneficial to enhance sensitivity in thermal diffusivity[67].

In this study, the concentrated light source is modulated sinusoidally to apply periodic heating to samples. We limit the periodic heating frequency to 0.15 Hz due to safety and operational stability of the Xenon light bulb[11]. The lower limit of the heating frequency is 0.02 Hz because of the lengthy measurement time at low heating frequencies. The main effect results for amplitude decay of selected input parameters are shown in Fig. 3.7 (top row). Similar to a prior study[67], sensitivity in thermal diffusivity increases with the heating frequency. For relatively fast heating frequencies ($f_{heating} \geq 0.08$ Hz), emissivity and light blocker temperature exhibit low sensitivity. We also observe that the intensity distribution width σ_{solar} contributes little to the main effect. This finding is advantageous compared to Hatta et al.'s approach[60], Cowan's approach[42] and the laser flash method[95], each

of which are sensitive to the intensity distribution of the light source. The main effect results calculated using phase shift are shown in Fig. 3.7 (bottom row). Similarly, faster heating frequencies are advantageous for thermal diffusivity detection, and σ_{solar} makes an insignificant contribution to the main effect.

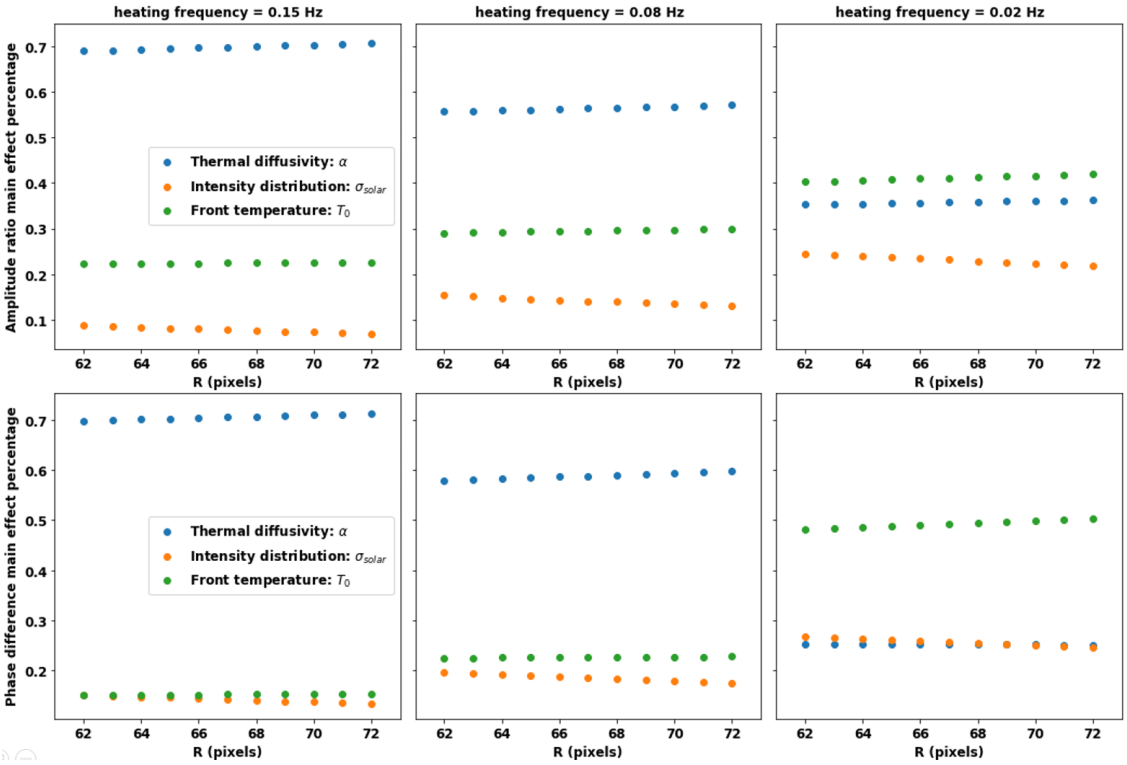

Figure 3.7: Top row: percentage main effect for amplitude ratio of different parameters at several heating frequencies. Bottom row: percentage main effect for phase difference of different parameters at several heating frequencies

The foregoing results indicate that high sensitivity for thermal diffusivity can be achieved with $f_{heating} \geq 0.08$ Hz for a graphite sample. The results also indicate that amplitude and phase are insensitive to the intensity distribution of the light source σ_{solar}.

3.4 Uncertainty quantification and results

3.4.1 Uncertainty quantification using a Bayesian framework

In this study we estimate thermal diffusivity using amplitude decay and phase shift measurements. Conventional parameter estimation methods convert an inverse problem to an optimization problem by minimizing residuals between measurement results and the physical model. In this case the inverse problem is ill-posed, and the solution is not unique. Also such methods lack rigorous uncertainty estimates for parameters. This study employs a Bayesian framework that incorporates prior knowledge of parameters and measurement processes to produce a complete statistical description of the parameters. Growing interest exists in applying the Bayesian framework to inverse heat transfer problems, and several studies have demonstrated its benefits[67][122][101][131].

The Bayesian framework is based on the Bayes' theorem. Consider a set of parameters θ and measurement results D; the posterior distribution for θ after observing D is expressed using Bayes' theorem:

$$p(\theta|D) = \frac{p(D|\theta)p(\theta)}{p(D)} \tag{3.20}$$

In this work, D consists of amplitude, phase measurements within a region of analysis and average temperature profiles at inner (R_0) and outer bounds (R_N) of the region. θ consists of four parameters: A_α, B_α, σ_{solar} and T_{bias}. A_α and B_α are the coefficients for temperature-dependent thermal diffusivity and are defined in Eq. 3.2. In our study, the intensity distribution of the concentrated light source is difficult to characterize precisely. Therefore, we treat σ_{solar} as a unknown parameter and update our state of knowledge for σ_{solar} using the Bayesian framework. Lastly, the light blocker temperature measured using the IR camera (see Supplemental Materials S3 for details) also suffers slight system error because the measurement process differs from real experiments. Therefore, we introduce another parameter T_{bias} to augment the measured light blocker temperature to model the light blocker temperature under real measurement conditions.

The posterior distribution is proportional to the likelihood function $p(D|\theta)$ and the prior

distribution $p(\theta)$. The likelihood function $p(D|\theta)$ models the measurement process and indicates the probability of observing data D given parameter θ and measurement noise σ_D. First we consider amplitude decay measurements. We denote measured amplitude decay at radius R_i as ΔA_i and assume that it follows a Gaussian distribution with mean $A[f(\theta)]$ and standard deviation $\sigma_{\Delta A,i}$. $A[f(\theta)]$ indicates the amplitude decay from the physical model f evaluated using parameter θ. For amplitude decay at R_i, the likelihood function is given by.

$$p(\Delta A_i|\theta) \sim \mathcal{N}\left(\mu = \Delta A_i - A[f(\theta)]_i, \Sigma = \sigma_{\Delta A,i}\right) \tag{3.21}$$

Assuming amplitude measurements at different radii are independent, then for all amplitude decay measurements ΔA within the region of analysis, the likelihood function is:

$$p(\Delta A|\theta) \sim \prod_{i=1}^{N} \mathcal{N}\left(\mu = \Delta A_i - A[f(\theta)]_i, \Sigma = \sigma_{\Delta A,i}\right) \tag{3.22}$$

The likelihood functions for all phase shift measurements $\Delta\phi$ within the region of analysis are derived similarly. $\phi[f(\theta)]$ indicates the phase shift from the physical model f evaluated using parameter θ:

$$p(\Delta\phi|\theta) \sim \prod_{i=1}^{N} \mathcal{N}\left(\mu = \Delta\phi_i - \phi[f(\theta)]_i, \Sigma = \sigma_{\Delta\phi,i}\right) \tag{3.23}$$

In addition, the likelihood functions for the mean temperature profiles at the inner ($T_{mean,R0}$) and outer ($T_{mean,RN}$) bounds of the region of analysis are treated as follows. $T_m([f(\theta)])$ indicates the mean temperature obtained from the physical model f evaluated using parameter θ. σ_T indicates the standard deviation in mean temperature measurements. Unlike amplitude and phase measurements, we manually choose $\sigma_T = 2$ K to ensure the mean simulated temperatures within the region of analysis match experimental measurements. Because we use temperature-dependent properties in this study, matching simulated and experimentally measured mean temperatures is important. The likelihood function becomes:

$$\begin{aligned} p(T_{mean}|\theta) = &\mathcal{N}\left(\mu = T_{mean,R0} - T_m([f(\theta)])_0, \Sigma = \sigma_T\right) \\ &\times \mathcal{N}\left(\mu = T_{mean,RN} - T_m([f(\theta)])_N, \Sigma = \sigma_T\right) \end{aligned} \tag{3.24}$$

By further assuming that ΔA, $\Delta\phi$, $T_{mean,R0}$ and $T_{mean,RN}$ are statistically independent, the simplified likelihood function becomes:

$$p(D|\theta) = p(\Delta A, \Delta\phi, T_{mean,R0}, T_{mean,RN}|\theta) = p(\Delta A|\theta)p(\Delta\phi|\theta)p(T_{mean,R0}|\theta)p(T_{mean,RN}|\theta) \tag{3.25}$$

The prior distribution $p(\theta)$ represents the prior knowledge for θ. We assume A_α, B_α, σ_{solar} and T_{bias} are statistically independent. Therefore, $p(\theta)$ is expressed as:

$$p(\theta) = p(A_\alpha)p(B_\alpha)p(\sigma_{solar})p(T_{bias}) \tag{3.26}$$

Substituting the likelihood function (Eq. 3.25) and the prior distribution (Eq. 3.26) into the Bayes posterior defined in Eq. 3.20, the posterior distribution is expressed as:

$$\begin{aligned}
p(\theta|D) &= p(A_\alpha, B_\alpha, \sigma_{solar}, T_{bias}|\Delta A, \Delta\phi, T_{mean,R0}, T_{mean,RN}) \\
&= \frac{p(\Delta A, \Delta\phi, T_{mean,R0}, T_{mean,RN}|A_\alpha, B_\alpha, \sigma_{solar}, T_{bias})p(A_\alpha, B_\alpha, \sigma_{solar}, T_{bias})}{p(\Delta A, \Delta\phi, T_{mean,R0}, T_{mean,RN})} \\
&\sim \prod_{i=1}^{N} \mathcal{N}\left(\mu = \Delta A_i - A[f(\theta)]_i, \Sigma = \sigma_{\Delta A,i}\right) \mathcal{N}\left(\mu = \Delta\phi_i - \phi[f(\theta)]_i, \Sigma = \sigma_{\Delta\phi,i}\right) \\
&\times \mathcal{N}\left(\mu = T_{mean,R0} - T_m([f(\theta)])_0, \Sigma = \sigma_T\right) \mathcal{N}\left(\mu = T_{mean,R0} - T_m([f(\theta)])_N, \Sigma = \sigma_T\right) \\
&\times p(A_\alpha)p(B_\alpha)p(\sigma_{solar})p(T_{bias})
\end{aligned} \tag{3.27}$$

For an arbitrary distribution with unknown normalization constant, the Markov chain Monte Carlo (MCMC) method is typically used to obtain random samples to reconstruct such a distribution. The most commonly used MCMC algorithm is random walk Metropolis[81] because of its simplicity[122][101][67]. However, this algorithm suffers poor convergence and low efficiency for problems with large parameter spaces[32]. To expand the exploration of the parameter space and to improve convergence of the Markov chain, our work employs a No-U-Turn(NUT) sampler[63]. In addition, MCMC requires frequent evaluations of the physical model to calculate the likelihood function. This becomes infeasible for numerical models that require lengthy execution times. A previous study[101] demonstrated significant time efficiency improvement using polynomial chaos for an inverse heat transfer problem. In this

study, we develop a non-intrusive polynomial chaos (order 4) surrogate model using a python module "chaospy"[48] to accelerate the original finite difference model. The surrogate model exhibits high accuracy (maximum 0.5% error) for steady temperature profiles, amplitude decay, and phase shift predictions, yet the execution time is reduced to a few milliseconds from several minutes. The error in the surrogate model is neglected in this study. We employ the python module pymc3 [103] with custom modifications[7] to implement the NUT sampler.

3.4.2 NUT sampler's results using a graphite sample

To demonstrate the Bayesian framework and NUT sampler, we first tested an isotropic graphite sample (manufacturer:Entegris, grade:TM). The sample's thickness is 0.92 mm with outer diameter 88.50 mm. The density of the graphite sample is 1740 kg/m^3. We used a polynomial fit for specific heat [3] as:

$$c_p(T) = 2245 + 4.56 \times 10^{-2}T - 5.61 \times 10^5/T + 2.77 \times 10^7/T^2 \tag{3.28}$$

The gray emissivity of the graphite is 0.77, and we coated a layer of thin layer of diffuse high-emissivity (0.88) material on the back side of the sample to facilitate IR thermography. We modulated the light source using a 0.1 Hz voltage signal to achieve relatively high sensitivity in thermal diffusivity. We heated the sample from room temperature to high temperature with 119 A solar simulator current. Steady temperatures were obtained after 10 min, and then a 0.1 Hz oscillation current signal with amplitude 22 A was superimposed on the 110 A bias current. We started the IR recording after approx. one to two minutes when the sample exhibited quasi-steady-state oscillations.

Here we analyze a region on the IR image bounded by $R_0 = 61$ and $R_N = 73$ pixels to obtain temperature profiles and corresponding amplitude decay and phase shift. This region is chosen for high signal-to-noise ratio in both amplitude ratio and phase shift. In addition, the region is chosen to be relatively narrow to keep the temperature difference low (approx. 40 K), such that Eq. 3.2 remains valid to model thermal diffusivity as a function of

temperature.

The results obtained using the NUT sampler are shown in Fig. 3.8. The top row of subfigures contains the trace plots for four unknown parameters. A trace plot shows the sequential value of a parameter obtained from the NUT sampler. The trace plots exhibit good mixing, and different chains for each parameter oscillate around nearly the same constant value, indicating convergence of the sampling process. The middle row contains histograms obtained from the trace plots of corresponding parameters. The normalized histograms represent the posterior distribution of parameters and indicate the updated state of knowledge given the prior knowledge and the measurement process. The bottom row contains the auto-correlation of the corresponding trace plots in the top row. The auto-correlation decreases rapidly to zero for all parameters, indicating high sampling efficiency.

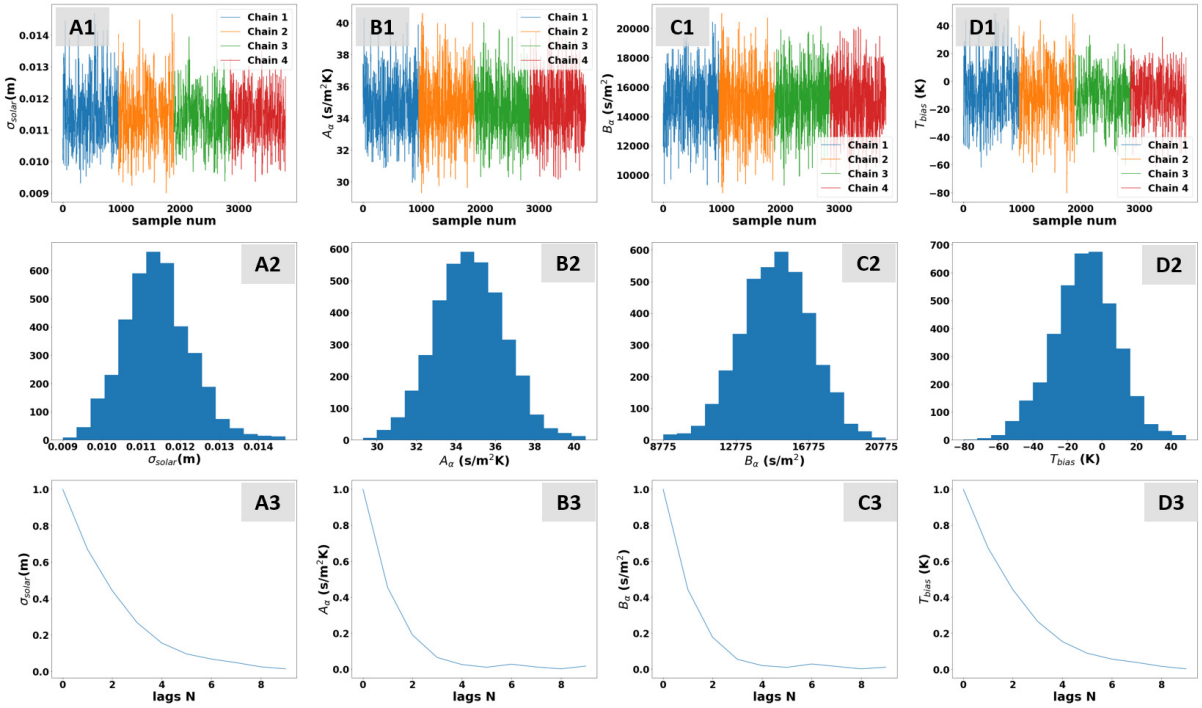

Figure 3.8: Top row: Trace plots of parameters. (A1) Intensity distribution width for the concentrated light source σ_{solar}. (B1) and (C1) Parameters for temperature-dependent thermal diffusivity A_α and B_α. (D1) Bias temperature of the light blocker T_{bias}. Middle row: Histograms of the trace plots in the top row. Bottom row: auto-correlation of the trace plots in the top row.

Given the posterior distributions of A_α and B_α, the temperature-dependent thermal diffusivity within the region of analysis (ROA) is shown in Fig. 3.9. The mean temperatures of the inner and the outer boundary of the ROA are approx. 960 K and 1000 K respectively. The solid line indicate the posterior mean for thermal diffusivity, and the blue band indicates corresponding uncertainty. The same grade graphite samples have been measured using the laser flash method by the manufacturer[3] and are shown as green lines. Good agreement between the posterior results and reference values[3] is observed for the entire temperature range within the ROA.

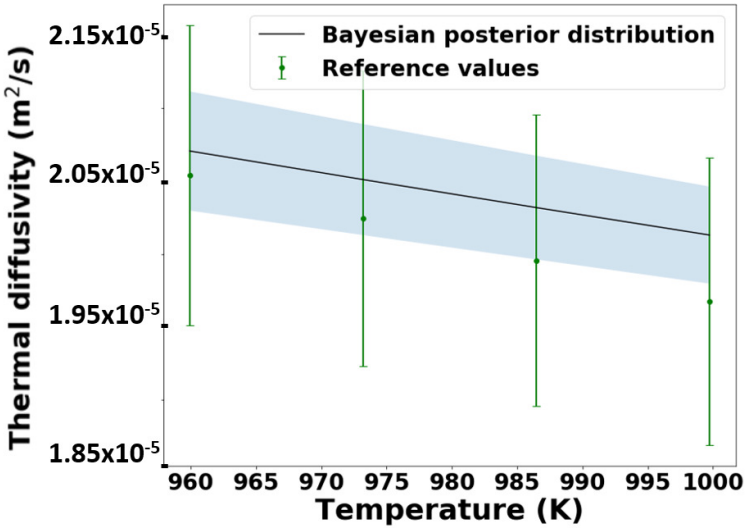

Figure 3.9: Thermal diffusivity as a function of temperature evaluated using A_α and B_α (solid black line) and corresponding uncertainties (blue shade) and reference values [3].

The fitted amplitude (Fig. 3.10A), phase (Fig. 3.10B) and temperatures (Fig. 3.10C) are plotted using the parameters' posterior means, and they match well with experimental measurements.

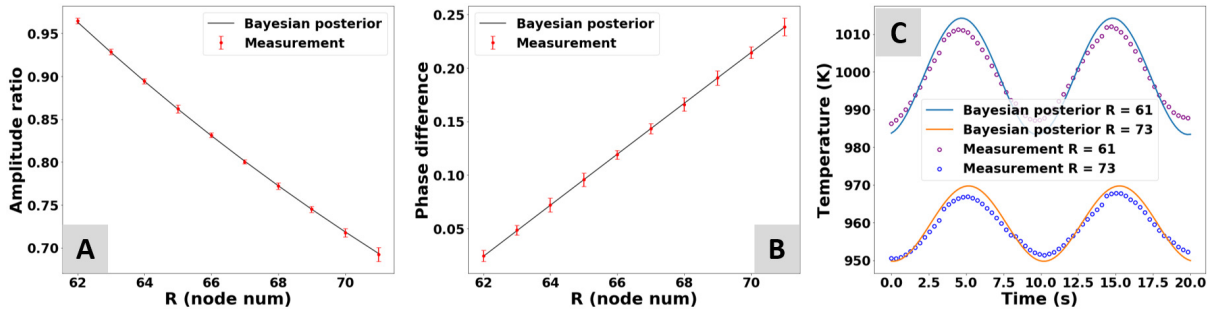

Figure 3.10: Fitted amplitude decay (A), phase shift (B) and temperature profiles at inner and outer boundary of the ROA (C) using the posterior means of parameters from Fig. 3.8C

3.4.3 Results for graphite at different frequencies and bias voltages

We fixed the bias current of the solar simulator at 119 A and measured multiple graphite samples at different frequencies. Here the tested frequency range is from 0.08 Hz to 0.14

Hz to achieve relatively high sensitivity in thermal diffusivity. We analyze amplitude decay and phase shift within $R_0 = 61$ and $R_N = 73$ pixels, and the results are shown in Fig. 3.11 in which thermal diffusivity values exhibit good consistency among the different frequencies and multiple samples.

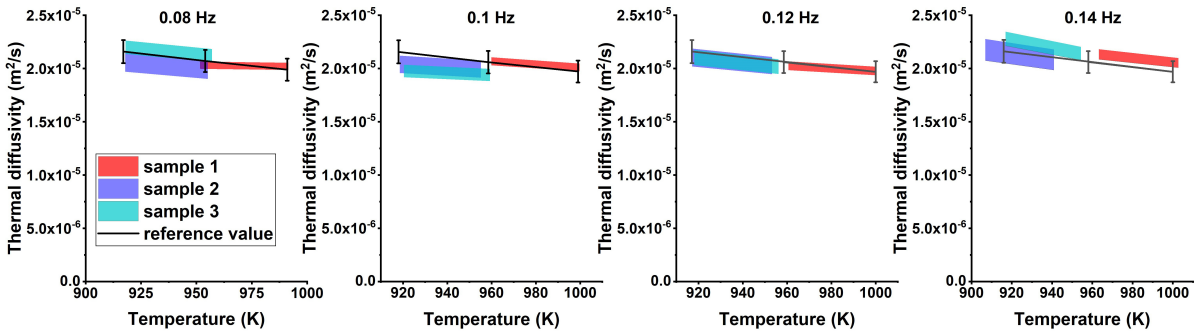

Figure 3.11: Thermal diffusivity measured at different frequencies for multiple graphite samples compared to reference values[3].

Next, we fixed heating frequency at 0.1 Hz and changed the bias current. Here we choose 119, 152 and 179 A as bias current for the solar simulator and 22 A as the oscillation amplitude. We also explore different region of analysis on the sample. In addition to the region bounded by $R_0 = 61$ and $R_N = 73$ pixels used in previous sections, we analyze another region bounded by $R_0 = 73$ and $R_N = 85$ pixels shown as region 2 in Fig. 3.12A. This region exhibits lower signal-to-noise ratio compared to region 1, but it also experiences lower temperatures and can extend the temperature measurement range for each test. The results for different currents and different regions are shown in Fig. 3.12B. We achieve thermal diffusivity measurements over a broader temperature range (220 K) using a wider range of bias currents. The results obtained under different bias currents exhibit good agreement with the reference values[3] over 900 - 1120 K.

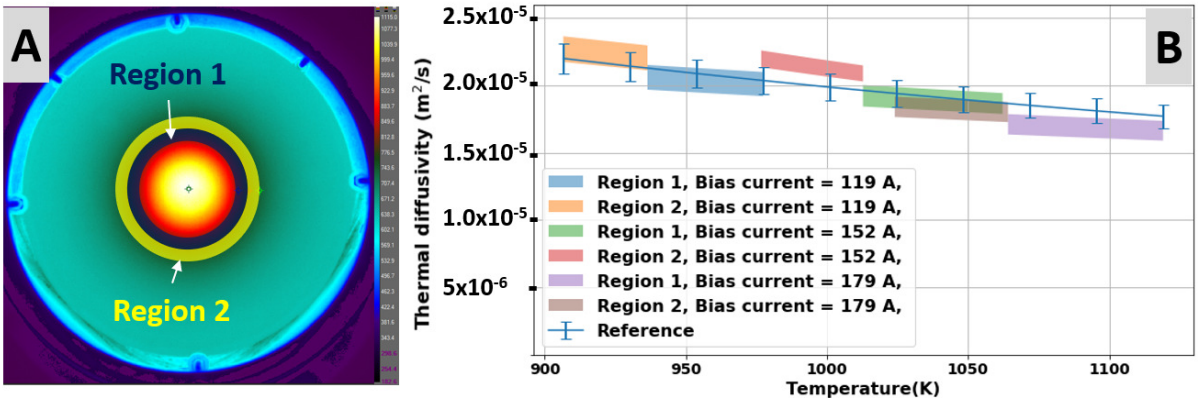

Figure 3.12: (A) Region of analysis in an IR image. Region 1 bounded by $R_0 = 61$ and $R_N = 73$ pixels. Region 2 bounded by $R_0 = 73$ and $R_N = 85$ pixels. (B) Thermal diffusivity measured under different bias currents and in different regions, compared to reference values[3].

3.4.4 Results for a copper sample

We also tested a copper sample (certified copper 110, 99.9% purity). The sample's thickness is 0.79 mm with outer diameter 88.50 mm. We use a polynomial fit for temperature-dependent specific heat [126]. The copper sample's front and back surfaces were coated with a thin layer of diffuse high-emissivity (0.88) coating (Aremeco, 840MX). The weight contribution of the coating is less than 2% of the sample's total weight and is neglected. The copper sample was measured using 119 A bias current under several different frequencies. The results are shown in Fig. 3.13, and good agreement with reference values[118] is observed.

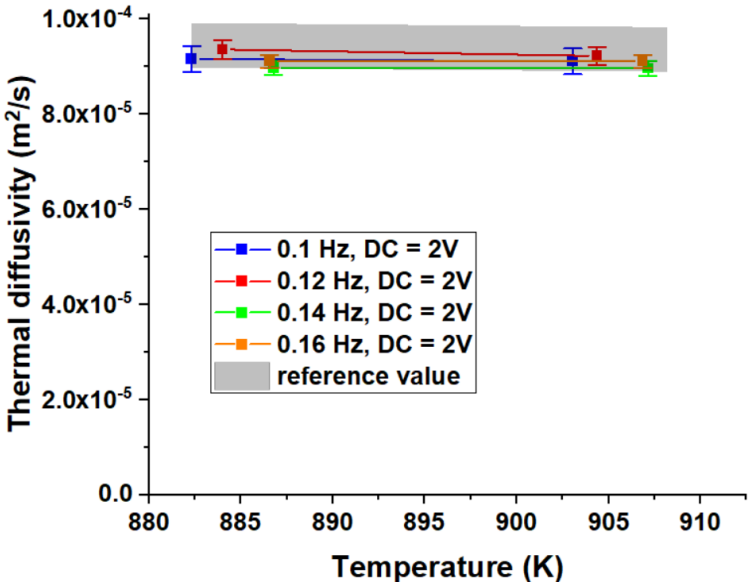

Figure 3.13: Thermal diffusivity of copper measured at different heating frequencies.

3.5 Conclusions

In this work, we present a custom instrument for characterizing thermal diffusivity at high temperatures using a modified Ångström's method. The sample under test is heated directly using a concentrated light source and reaches steady high temperatures rapidly (approx. 10 mins). This is advantageous compared to existing methods that heat samples from surroundings and typically require hours to reach steady high temperatures. We employ non-contact, non-destructive and data-rich IR thermography to measure quasi steady-state oscillating temperature profiles, and an efficient averaging method to process the noisy IR images and obtain temperature profiles with low noise. Amplitude and phase results extracted from such temperature profiles are robust against errors in emissivity. For uncertainty quantification, a surrogate-accelerated Bayesian framework and a NUT sampler are developed to obtain statistical distributions for parameters of interest. For several graphite and copper samples under test, we observe good agreement with reference values under different heating frequencies. We also measure different temperature ranges by adjusting solar simulator current. In general, the results obtained using the custom instrument exhibit approx. 5%

difference compared to reference values obtained using the laser flash method. The custom instrument's time efficiency, accuracy, inherent ability to quantify uncertainty rigorously, and relatively low overall cost are expected to benefit researchers for characterizing thermal diffusivity at high temperatures.

CHAPTER 4

Surrogate-accelerated Bayesian framework for high-temperature thermal diffusivity characterization

4.1 Bayesian framework for uncertainty quantification

With the rapid performance improvement of computational resources the Bayesian framework is becoming increasingly popular in solving inverse heat transfer problems. Early works demonstrated the effectiveness of the Bayesian framework for identifying unknown heat sources in conduction[122] and radiation[124] for hypothetical problems. Recently, the Bayesian framework has been adopted in thermophysical property metrology applications, especially for the laser flash method[19][101][71], and we have previously reported a Bayesian framework for Ångström's method under ambient conditions[67]. For high-temperature conditions with strong nonlinear radiation losses, Bayesian analysis has not yet been reported. The challenges involve probing the posterior distribution using computationally expensive numerical modeling and achieving convergence in the MCMC sampling process for nonlinear problems with many unknowns. In the following section, we employ a parametric surrogate model using polynomial chaos to accelerate the original model. Then, we outline the configuration of our Bayesian framework and employ a No-U-Turn sampler to enhance the convergence of the sampling process.

4.1.1 Physical model acceleration

In our study, evaluating the original finite difference model requires approx. 40 s. Therefore, probing the posterior distribution using the original model is infeasible because MCMC

requires numerous and successive model evaluations. Merely 1000 such evaluation requires approx. 10 hours. As a result, computational speed must be significantly increased to enable the Bayesian analysis for practical use.

Generally, two approaches are used to accelerate the computational speed of a physical model. The first approach is model order reduction (MOR), and commonly used techniques include proper orthogonal decomposition (POD)[78], Krylov-subspace methods[49] and balanced truncation[87]. Krylov-subspace methods and balanced truncation are applicable in linear systems. POD is applicable to nonlinear systems[26] in which a large system of equations are projected to a reduced subspace. The model is solved efficiently in the reduced subspace and the solution is transformed back to the original space. In our study the total number of nodes is approx. 200, which is rather low compared to existing studies using POD. Therefore, the original model space is difficult to be reduced significantly to achieve dramatic computational improvement.

The second approach is to approximate the original physical model using a computationally efficient surrogate model. Commonly used surrogate models include the Gaussian process (GP) and polynomial chaos (PC) expansion[26][92]. In general, both approaches can produce excellent approximation to the original physical model. An thorough comparison between these two approaches is given in [92]. In this study we employ PC because of its simplicity and faster online execution performance compared to GP and POD. PC can be further categorized into intrusive and non-intrusive approach. The intrusive approach is generally more computationally efficient but requires significant work to derive the system of equations for the PC coefficients from the governing equations. The non-intrusive approach treats the physical model as a black-box and computes PC coefficients by evaluating the physical model at quadrature points, which is much more convenient. Therefore, we employ a non-intrusive approach to construct the parametric surrogate model as discussed below.

In this work, four parameters in the physical model are treated as random variables. The first two parameters are A_α and B_α that define the temperature-dependent thermal diffusivity (Eq. 3.2). The third parameter is the intensity distribution of the solar simulator

σ_{solar}(Eq. 3.1). The fourth parameter is T_{bias}, which models the system error introduced when measuring the light blocker temperature. We assume the prior distributions for all parameters follow uniform distributions. That is,

$$A_\alpha \sim U(A_{\alpha,\text{lower}}, A_{\alpha,\text{upper}}) \tag{4.1}$$

$$B_\alpha \sim U(B_{\alpha,\text{lower}}, B_{\alpha,\text{upper}}) \tag{4.2}$$

$$\sigma_{solar} \sim U(\sigma_{solar,lower}, \sigma_{solar,upper}) \tag{4.3}$$

$$T_{bias} \sim U(T_{bias,lower}, T_{bias,upper}) \tag{4.4}$$

We further assume that these parameters are statistically independent, and we denote $\theta = \{A_\alpha, B_\alpha, \sigma_{solar}, T_{bias}\}$.

We denote the parametric surrogate model as $\hat{f}(r,t,\theta)$, where r indicates sample radius and t indicates time. By definition,

$$\hat{f}(r,t,\theta) = \sum_{i=0}^{M} C_i(r,t)\Psi_i(\theta) \tag{4.5}$$

where $C_i(r,t)$ are PC coefficients (also known as Fourier coefficients). $\Psi_i(\theta)$ are orthogonal polynomials with respect to the joint probability density function (PDF) of θ:

$$< \Psi_i(\theta), \Psi_j(\theta) >= \int \Psi_i(\theta)\Psi_j(\theta)p(\theta)d\theta = \delta_{ij} \text{ , for } i,j = 0, \cdots, M \tag{4.6}$$

The orthogonal polynomials are determined here using a python module "chaospy"[48], and we employ the Askey-Wilson scheme to construct such polynomials given the joint PDF of θ. The infinite PC series is truncated to finite $M+1$ terms as determined by the number of unknown parameters N_θ and the PC order(N_P):

$$M + 1 = \frac{(N_\theta + N_P)!}{N_\theta! N_P!} \tag{4.7}$$

PC coefficients are calculated using the spectral projection approach[54] from $f(r,t,\theta)$, which indicates the original physical model:

$$C_i(r,t) =< f(r,t,\theta), \Psi_i(\theta) >= \int \Psi_i(\theta) f(r,t,\theta)p(\theta)d\theta \text{ , for } i = 0, \cdots, M \tag{4.8}$$

Integrating Eq. 4.8 analytically is impractical. In this work, we use Gaussian quadrature and "chaospy"[48] to evaluate the integral numerically.

$$C_i(r,t) = \int \Psi_i(\theta) f(r,t,\theta) p(\theta) d\theta \approx \sum_{k=1}^{K} f(r,t,\theta_k)\Psi_i(\theta_k) w_k \text{ , for } i = 0, \cdots, M \tag{4.9}$$

where θ_k ($k = 1$ to K) indicates quadrature points, and w_k are the corresponding quadrature weights.

After calculating all PC coefficients, the surrogate models can rapidly and accurately predict model outputs for any θ within the joint prior probability distribution $p(\theta)$. In this study, we develop three PC surrogate models to simulate quasi-steady state temperature profiles, amplitude decay and phase shift within a region of analysis (ROA) on a sample. The model form error for the finite difference solver and the error in the surrogate models are not considered in this study.

4.1.2 Bayesian inverse problem and the No-U-Turn sampler

In this study we aim to estimate the temperature-dependent thermal diffusivity from amplitude decay and phase shift measurements obtained with our custom instrument. Specifically, we modulated the concentrated light source using a 0.12 Hz control voltage signal and measured the temperature response of a thin isotropic graphite disk (POCO graphite, manufacturer: Entegris, grade TM)[3] at approx.1000 K. The data D consist of temperature profiles at quasi-steady state and corresponding amplitude decay phase shift extracted from these temperature profiles. We mostly rely on amplitude decay and phase shift because they are robust against uncertainty in emissivity of the sample's surface[67].

The Bayesian approach to formulate the inverse problem is to construct the posterior distribution $p(\theta|D)$ using Bayes theorem given the prior distribution $p(\theta)$ and the likelihood function $p(D|\theta)$.

$$p(\theta|D) = \frac{p(D|\theta)p(\theta)}{p(D)} \tag{4.10}$$

The prior distribution reflects our knowledge of the parameters before observing measurement results. It also serve as a mechanism of regularization for the inverse problem[47][122].

The likelihood function describes the measurement process. In the following sections, we illustrate the prior distribution, the formulation of the likelihood function and the posterior distribution.

4.1.2.1 Prior distribution

In section 4.1.1, we introduce the four unknown parameters in the model. We first consider the intensity distribution parameter of the solar simulator σ_{solar}. Based on a previous study which characterize a similar concentrated light source[14], the estimated σ_{solar} is 0.01 m. We assign a wide uniform prior distribution to cover possible values for σ_{solar} in Eq. 4.11.

$$p(\sigma_{solar}) = U(0.004, 0.018) \text{ ,unit (m)} \tag{4.11}$$

Next we consider T_{bias}, which models the bias error for measuring the light blocker temperature. Considering unknown reflections from the surroundings (approx. 20 K error), and intrinsic error in the IR camera for high-temperature measurements (approx. 20 K), we assign a wide uniform prior distribution for T_{bias} in Eq. 4.12.

$$p(T_{bias}) = U(-100, 100) \text{ ,unit (K)} \tag{4.12}$$

Lastly we consider the coefficients for temperature dependent thermal diffusivity A_α and B_α. For isotropic graphite, we expect at 1000 K, thermal diffusivity must be positive and must be less than commonly reported thermal diffusivity at room temperatures, which is approx. 10^{-4} m^2/s [18]. We also anticipate the thermal diffusivity of graphite to decrease when temperature increases because of increased scattering. Therefore, A_α must be positive. We constrained the minimum of B_α to be 1000 for numerical stability. We construct two wide uniform prior distribution for A_α and B_α respective in Eq. 4.13 and Eq. 4.14.

$$p(A_\alpha) = U(0, 100) \text{ ,unit } (s/m^2K) \tag{4.13}$$

$$p(B_\alpha) = U(1000, 40000) \text{ ,unit } (s/m^2) \tag{4.14}$$

We assume that these parameters are statistically independent and the simplified prior distribution $p(\theta)$ is expressed as:

$$p(\theta) = p(A_\alpha)p(B_\alpha)p(\sigma_{solar})p(T_{bias}) \tag{4.15}$$

4.1.2.2 Likelihood function

The likelihood function $p(D|\theta)$ models the measurement process subject to additive noise. Fig. 4.1A shows an IR image of a graphite sample, and Fig. 4.1B shows the corresponding temperature contour plot. The region exposed to the concentrated light source is shown by the yellow circle in Fig. 4.1B. We extract amplitude decay and phase shift from a ROA bounded by the green annulus shown in Fig. 4.1B. The extracted amplitude decay and phase shift are shown in Fig. 4.1C and Fig. 4.1D respectively. Different series indicate amplitude and phase extracted from regions bounded by different angles indicated by the blue dashed lines in Fig. 4.1B.

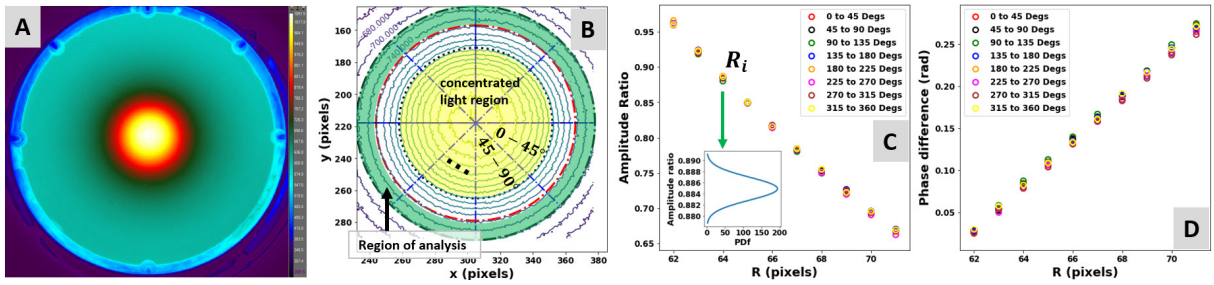

Figure 4.1: (A) An IR image of a graphite sample. (B) Temperature contour plot of (A). (C) Amplitude decay results as a function of radius at multiple regions (shown as different data series) bounded by different angles shown in (B). (D) Phase shift results as a function of radius at multiple regions bounded by different angles shown in (B)

To develop the likelihood function, we first consider the amplitude decay results. Fig. 4.1C shows amplitude decay measurements at different radial locations from R_0 to R_N. For a given radius R_i, we assume that the amplitude decay follows a Gaussian distribution with mean ΔA_i and standard deviation $\sigma_{\Delta A_i}$. Therefore, the probability of observing ΔA_i given the

parameter θ and the surrogate model $\hat{f}(t, r, \theta)$ is expressed as:

$$p(\Delta A_i|\theta) = \mathcal{N}\left(\Delta A_i|\mu = \Delta A[\hat{f}(\theta, r, t)], \Sigma = \sigma_{\Delta A,i}\right) \tag{4.16}$$

where $\Delta A[\hat{f}(\theta, R_i, t)]$ indicates amplitude decay computed using the surrogate model at R_i. We assume amplitude decay results are independent at different radii. Therefore, the likelihood function for amplitude decay for all radii within the ROA is expressed as:

$$p(\Delta A|\theta) = \prod_{i=1}^{N} \mathcal{N}\left(\Delta A_i|\mu = \Delta A[\hat{f}(\theta, R_i, t)], \Sigma = \sigma_{\Delta A,i}\right) \tag{4.17}$$

For phase shift measurements $\Delta\phi$ shown in Fig. 4.1D, the likelihood function is similarly expressed in Eq. 4.18.

$$p(\Delta\phi|\theta) = \prod_{i=1}^{N} \mathcal{N}\left(\Delta\phi_i|\mu = \Delta\phi[\hat{f}(\theta, R_i, t)], \Sigma = \sigma_{\Delta\phi,i}\right) \tag{4.18}$$

Lastly, we consider the mean temperatures at the inner and outer boundaries of the ROA, $T_{m,R0}$ and $T_{m,RN}$. In this study, thermal properties such as specific heat and thermal diffusivity are temperature-dependent. Therefore, matching simulated and experimentally measured mean temperatures within the ROA is important. Similar to amplitude decay and phase shift, we model the likelihood function of mean temperature using Gaussian distributions. However, we manually choose a low standard deviation $\sigma_{Tm} = 2$ K to enforce simulated temperatures to match experimental measurements. The likelihood function for mean temperature is given in Eq. 4.19, where $T_m[\hat{f}(\theta, R_i, t)]$ indicates mean temperature computed using the surrogate model at R_i.

$$\begin{aligned} p(T_m|\theta) = &\mathcal{N}\left(T_{m,R0}|\mu = T_m([\hat{f}(\theta, R_0, t)]), \Sigma = \sigma_{Tm}\right) \\ &\times \mathcal{N}\left(T_{m,RN}|\mu = [T_m(\hat{f}(\theta, R_N, t), \Sigma = \sigma_{Tm}\right) \end{aligned} \tag{4.19}$$

We further assume that amplitude decay, phase shift and mean temperatures are independent; the likelihood function is simplified as:

$$p(D|\theta) = p(\Delta A, \Delta\phi, T_{m,R0}, T_{m,RN}|\theta) = p(\Delta A|\theta)p(\Delta\phi|\theta)p(T_{m,R0}|\theta)p(T_{m,RN}|\theta) \tag{4.20}$$

We substitute Eq. 4.17-4.19 into Eq. 4.20 to obtain the expression for the likelihood function:

$$p(D|\theta) = \prod_{i=1}^{N} \mathcal{N}\left(\Delta A_i|\mu = \Delta A[\hat{f}(\theta, R_i, t)], \Sigma = \sigma_{\Delta A,i}\right) \mathcal{N}\left(\Delta\phi_i|\mu = \Delta\phi[\hat{f}(\theta, R_i, t)], \Sigma = \sigma_{\Delta\phi,i}\right)$$
$$\times \mathcal{N}\left(T_{m,R0}|\mu = T_m([\hat{f}(\theta, R_0, t)]), \Sigma = \sigma_{Tm}\right) \mathcal{N}\left(T_{m,RN}|\mu = [T_m(\hat{f}(\theta, R_N, t), \Sigma = \sigma_{Tm}\right) \tag{4.21}$$

4.1.3 Posterior distribution and the No-U-Turn sampler

The posterior distribution defined in Eq. 4.10 is expressed using the prior distribution in Eq. 4.15 and the likelihood function in Eq. 4.21:

$$\begin{aligned} p(\theta|D) = \frac{p(D|\theta)p(\theta)}{p(D)} = &\prod_{i=1}^{N} \mathcal{N}\left(\Delta A_i|\mu = \Delta A[\hat{f}(\theta, R_i, t)], \Sigma = \sigma_{\Delta A,i}\right) \\ &\times \mathcal{N}\left(\Delta\phi_i|\mu = \Delta\phi[\hat{f}(\theta, R_i, t)], \Sigma = \sigma_{\Delta A,i}\right) \\ &\times \mathcal{N}\left(T_{m,R0}|\mu = T_m([\hat{f}(\theta, R_0, t)]), \Sigma = \sigma_{Tm}\right) \\ &\times \mathcal{N}\left(T_{m,RN}\mu = [T_m(\hat{f}(\theta, R_N, t), \Sigma = \sigma_{Tm}\right) \\ &\times p(A_\alpha)p(B_\alpha)p(\sigma_{solar})p(T_{bias})/p(D) \end{aligned} \tag{4.22}$$

Here $p(D)$ is a normalizing constant. MCMC is commonly used to draw random samples from an arbitrary distribution up to a normalizing constant. The most commonly used MCMC approach, random walk Metropolis-Hasting, has produced satisfactory results for inverse heat transfer problems[123][19][101][16][67]. However, random walk becomes inefficient because the volume of the parameter space increases dramatically with a huge number of parameters[32][25]. For example, if large step size is used to propose new parameters, then the proposed state is strongly biased towards the space outside the target distribution, causing high rejection in the sampling process. Conversely if the proposal step size is kept low to reduce rejection in the sampling process, the resulting accepted states will concentrate tightly around the current state, which leads to poor exploration of the target distribution and high auto-correlation in accepted samples. Hamiltonian Monte Carlo (HMC)[45] is a more efficient sampling approach that models the target distribution using a Hamiltonian potential and explores the parameter space using Hamiltonian dynamics. An thorough in-

troduction to HMC is given in [25]. Instead of randomly exploring the target distribution, HMC introduces an auxiliary variable and decouples the sampling process into two phases: stochastic exploration of different levels of the Hamiltonian and deterministic exploration within a fixed Hamiltonian. This enables the sampling process to move away from the current state efficiently to unexplored region of the target distribution. In practice however, HMC is not widely used for two reasons. First, HMC requires significant hyperpameter tuning to achieve efficient sampling. Second, after a finite number of steps, HMC can travel back to its starting point, also known as U-turn behavior. The No-U-Turn (NUT) sampler[63] is based on HMC and addresses these two inherent flaws. In this work, we employ a NUT sampler to sample the posterior distribution defined in Eq. 4.22, and we employ a python module "pymc3" [103] to construct the NUT sampler. Currently, "pymc3" is only compatible with Theano-based functions, and we use [7] to construct the custom likelihood function to be compatible with our PC surrogate models. We have developed an open-source python module "pyangstromHT"[68] for experimental data extraction, surrogate model development and posterior distribution sampling.

4.2 Results

4.2.1 Conventional optimization approach

First, we solve the inverse problem using the classical nonlinear regression approach, in which the inverse problem is converted to an optimization problem and the unknown parameters are determined by minimizing regression residual[79][28][139]. The residual function is defined in Eq. 4.23, which takes similar form as the likelihood function defined in Eq. 4.21.

$$\begin{aligned} L(\theta) = \sum_{i=0}^{N} \left\{ \left(\frac{\Delta A[f(\theta, R_i, t)] - \Delta A_i}{\sigma_{\Delta A_i}} \right)^2 + \left(\frac{\Delta \phi[f(\theta, R_i, t)] - \Delta \phi_i}{\sigma_{\Delta \phi_i}} \right)^2 \right\} \\ + \left(\frac{T_m[f(\theta, R_0, t)] - T_m(R_0)}{\sigma_{Tm}} \right)^2 + \left(\frac{T_m[f(\theta, R_N, t)] - T_m(R_N)}{\sigma_{Tm}} \right)^2 \end{aligned} \tag{4.23}$$

Similarly, $\Delta A[f(\theta, R_i, t)]$,$\Delta \phi[f(\theta, R_i, t)]$ and $T_m[f(\theta, R_i, t)]$ indicate computing amplitude decay, phase shift and mean temperature at radius R_i with the original physical model using

parameter θ. ΔA_i and $\Delta\phi_i$ indicate experimentally measured amplitude decay and phase shift at radius R_i. $T_m(R_0)$ and $T_m(R_N)$ indicate experimentally measured mean temperatures at the inner and the outer radius of the ROA. $\sigma_{\Delta A_i}$ and $\sigma_{\Delta\phi_i}$ indicate standard deviation of amplitude decay and phase shift measurement at R_i. σ_{Tm} is chosen manually here as 2 K to enforce the simulated mean temperatures to match experimental measurements.

Nonlinear regression Levenberg–Marquardt algorithm is used here, and we employed a python module "lmfit"[90] to obtain the regression results. Here we examine five different initial values for θ and the corresponding final regression results are given in Table 4.1. We note that the regression results are not unique given different initial values for each parameter. The amplitude and phase fitting results are shown in Fig. 4.2, each column

Table 4.1: Initial parameter values and corresponding regression results

	Initial values				Regression results			
Regression #	σ_{solar} (m)	A_α (s/m^{2}K)	B_α (s/m^2)	T_{bias} (K)	σ_{solar} (m)	A_α (s/m^{2}K)	B_α (s/m^2)	T_{bias} (K)
1	0.0077	25	-488	20	0.0103	43.8	1081	8.5
2	0.0099	36.4	11900	10	0.0105	41.1	9961	13.8
3	0.0174	42.7	9750	0	0.0148	44.0	9616.4	54.9
4	0.0126	30.0	4000	15	0.0120	42.2	6372.3	7.6
5	0.0080	28.1	20000.0	-10.0	0.0101	31.8	18423.9	-6.0

corresponds to a specific initial condition indicated in table 4.1.

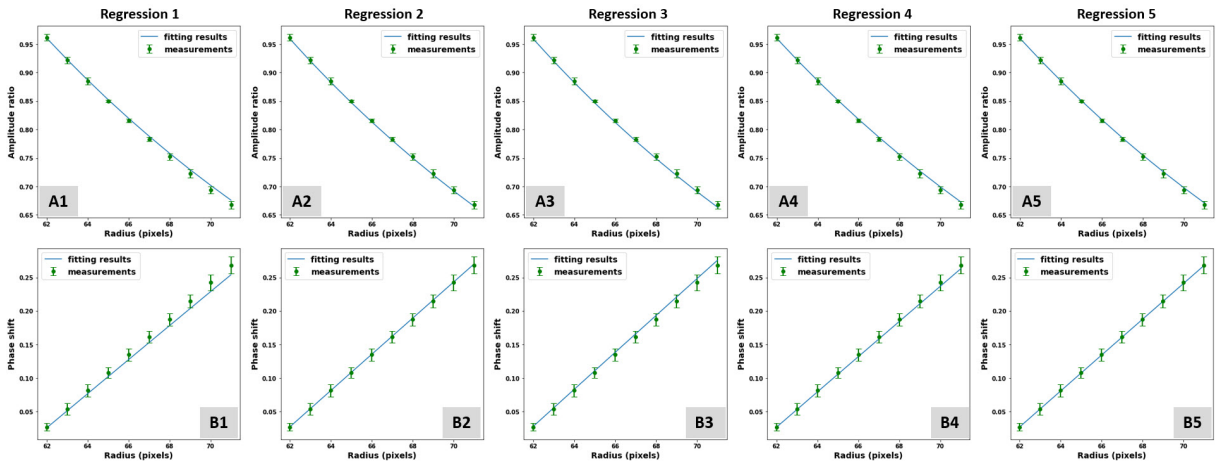

Figure 4.2: (A1-A4) Fitted amplitude decay vs experimental measurements. (B1-B4) Fitted phase shift simulation results with fitted parameter values vs experimental measurements.

To summarize, the solutions obtained via nonlinear regression are not unique, which is expected because for nonlinear problems multiple local minima exists. In addition, conventional regression techniques do not provide an uncertainty estimate for each parameter. Though a confidence interval for a parameter can be approximated using the covariance matrix, this typically does not work well for nonlinear problems because computing the covariance matrix requires linearing the physical model[26]. In the next section, we treat the unknown parameters as random variables and employ a Bayesian approach to solve the inverse problem.

4.2.2 Bayesian approach

4.2.2.1 PC surrogate model

In this study we employ PC as surrogate models to accelerate the Bayesian analysis. This involves developing the parametric PC surrogate models in an offline process and then implement the surrogate models in the "online" Bayesian analysis. Here we evaluate the online performance of such surrogate models in terms of accuracy and speed enhancement. We first examine their accuracy in the parameter space defined by the prior distributions in Eq. 4.15.

Here we use Latin hypercube to randomly generate 100 parameters $[\theta_1, ...\theta_{100}]$ within the joint prior distribution in Eq. 4.15. For each randomly generated θ_i, we evaluate the following quantities using both the surrogate model and the original model, and we calculate the maximum absolute relative error:

1. Amplitude decay as a function of radius
2. Phase shift as a function of radius
3. Temperature profile at radius R_0 as a function of time
4. Temperature profile at radius R_N as a function of time

Take $\theta_1 = \{0.01 \text{ m}, 35 \text{ s/m}^2\text{K}, 1000 \text{ s/m}^2, 10 \text{ K}\}$ for example. In Fig. 4.3 the top row shows simulated amplitude decay, phase shift and temperature profiles using a fourth order PC and the original physical model. The second row shows the relative absolute error and we highlight the maximum relative error in red for each quantity.

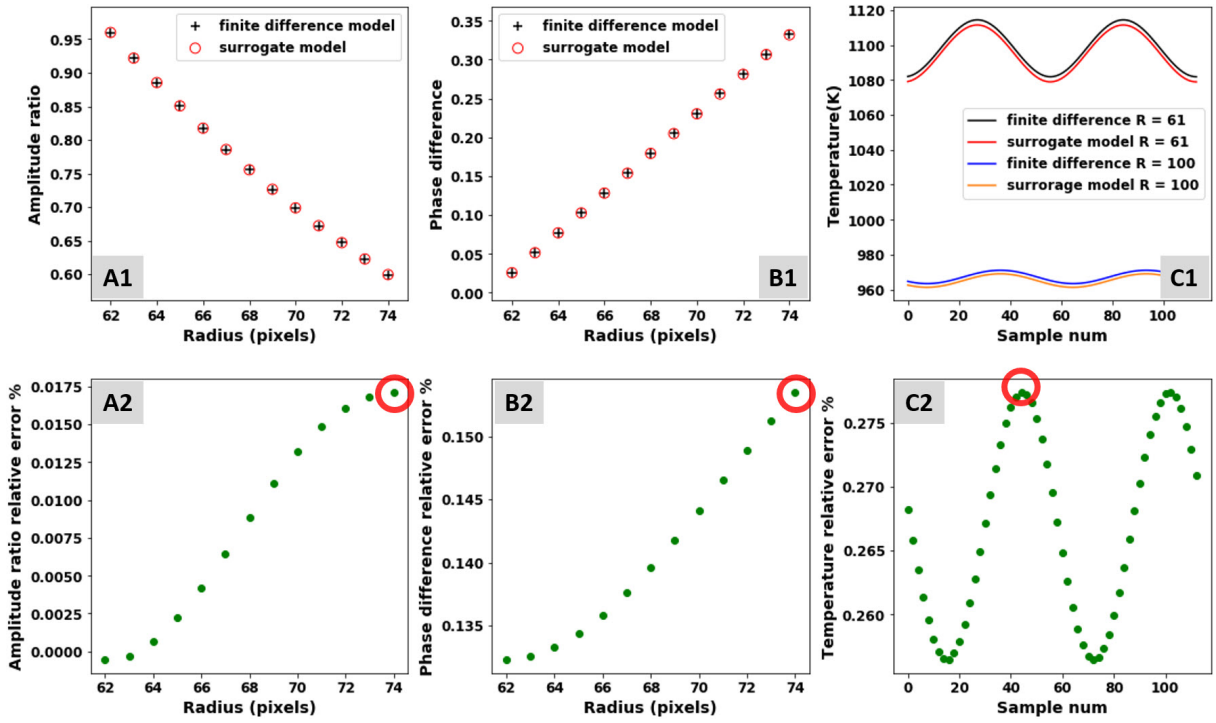

Figure 4.3: Top row: Simulated Amplitude decay (A1), phase shift (B1) and Temperature profiles at radius R_0 and R_N (C1) using both the fourth order PC and the original finite difference model. Bottom row: Relative error of amplitude decay (A2), phase shift (B2) and temperature profiles at radius R_0 and R_N (C2).

After obtaining the maximum relative errors for randomly generated $[\theta_1, ...\theta_{100}]$, we investigate these maximum relative errors by computing the mean, and global maximum for different PC orders. The results are shown in Fig. 4.4A and B respectively.

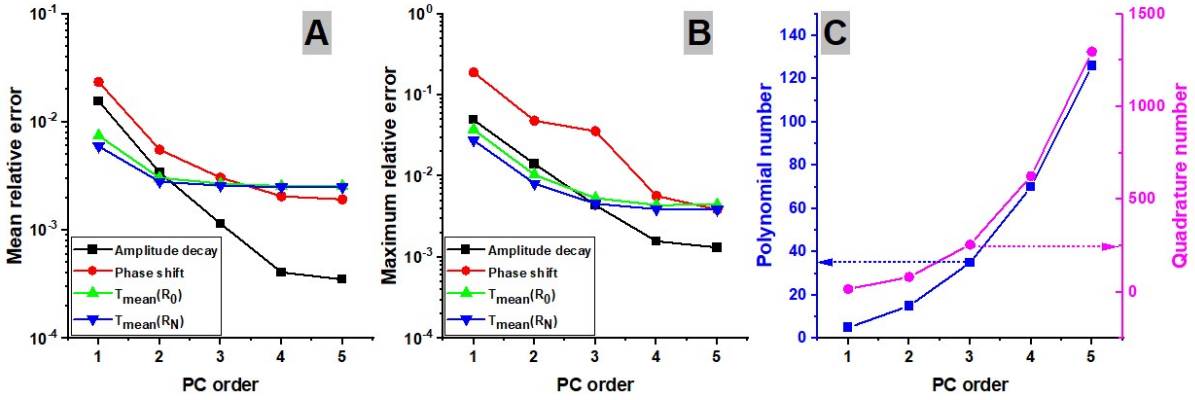

Figure 4.4: (A) Mean and (B) global maximum value for maximum relative errors as a function of PC order obtained by simulating 100 random Latin hypercube design. (C) The number of polynomials and the total number of Gaussian quadrature as a function of PC order.

We note that on average, the maximum relative error decreases as the order of the PC increases, as shown in Fig. 4.4A. For amplitude decay results, on average the maximum error decrease significantly from 1.6% to 0.041% when the PC order increases from one to four, and then decreases marginally to 0.035% if the PC order is increased to five. The global maximum relative error also decrease significantly from 5% to 0.16% when the PC order increases from one to four, and then decreases marginally to 0.13% if the PC order is further increased to five. Similarly for other quantities, the maximum global errors are less than 0.5% for the fourth order PC. Further increasing the PC order only narrowly improve its accuracy at the cost of significant increase in computational requirement. Fig. 4.4C indicates the number of polynomials and the total number of quadrature required to calculate the PC coefficients. For a model with N_θ parameters and approximated using PC with order N_P, the total number of polynomials required is $\frac{(N_\theta+N_P)!}{N_\theta!N_P!}$. If the order of quadrature is P_Q to compute the polynomial coefficients numerically, the total number of quadrature requires is $(P_Q+1)^{N_P}$. Therefore, in this work we use the fourth order PC for high accuracy and manageable total run time in the offline process.

On average, the time required to execute the original physical model is approx. 35 s,

whereas evaluating the surrogate model takes only 3.75 ms. The speed improvement using the surrogate model is more than 9,000 times. To conclude, given high accuracy over the entire joint prior distribution $p(\theta)$ and significant speed improvement, we employ the fourth order PC as the parametric surrogate model to accelerate the Bayesian analysis in the following sections.

4.2.2.2 The random walk Metropolis-Hasting sampler

Having obtained computationally efficient surrogate models, first we employ the commonly used random walk Metropolis-Hasting algorithm to sample the posterior distribution defined in Eq. 4.22 with four chains. We optimized the random walk step size to reduce auto-correlation between sequential samples while maintaining reasonable acceptance rate. The optimized step size is $\sigma = \{2 \times 10^{-4}\ \text{m}, 0.4\ \text{s/m}^2\text{K}, 160\ \text{s/m}^2, 0.8\ \text{K}\}$, and the acceptance rate for the sampling process is approx. 14%. The trace plot for all four parameters are shown in Fig. 4.6A1-A4 and we removed 30% of the initial samples in each chain as burn-in. Mixing for all parameters are relatively poor as observed from the trace plots, and high auto-correlations are observed as shown in Fig. 4.6B1 and B4. We employ the Gelman-Rubin criteria[51], which compares within-chain and between-chain variance, to check the convergence of the sampling process. We employ a python module "chainconsumer"[62] to implement the Gelman-Rubin criteria. All four parameters pass the convergence test. The $\hat{R}$ value for parameters $A_\alpha, B_\alpha, \sigma_{solar}, T_{bias}$ are 1.008, 1.002, 1.002 and 1.007 respectively, with $\hat{R} \approx 1$ indicating convergence. The histograms of the random samples obtained from the posterior distribution are shown in Fig. 4.6C1-C4, indicating the updated confidence interval for these parameters given the prior knowledge and the measurement process.

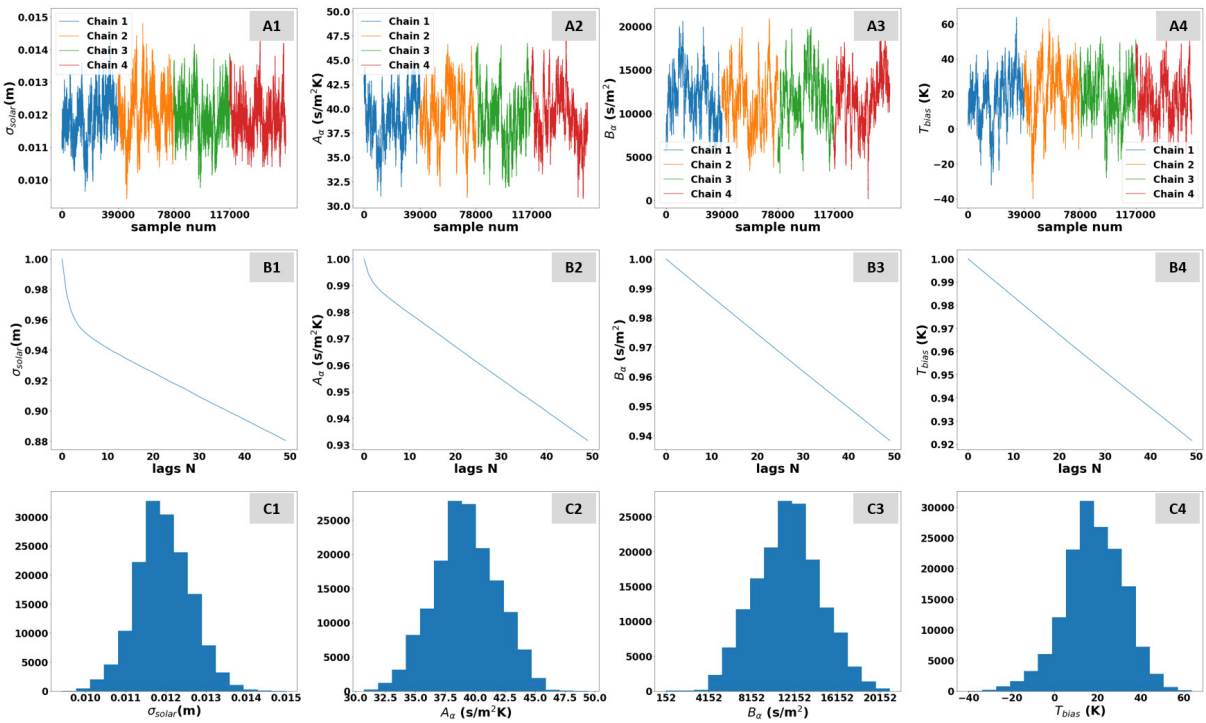

Figure 4.5: Random walk Metropolis-Hasting sampling results. (A1-A4) Trace plots for $A_\alpha, B_\alpha, \sigma_{solar}, T_{bias}$ for four different chains. (B1-B4) Auto-correlation of the trace plots in (A1-A4). (C1-C4) Histogram plots for random samples for $A_\alpha, B_\alpha, \sigma_{solar}, T_{bias}$ respectively, in (A1-A4).

Based on the posterior distribution of A_α and B_α, we plot the corresponding 99% confidence interval for thermal diffusivity as a function of temperature, which is shown as the blue band in Fig. 4.6A. The posterior distribution for thermal diffusivity matches well with the reference thermal diffusivity values[3] obtained using the laser flash method. Using the posterior mean for all four parameters, we obtain the simulated amplitude decay, phase shift and temperature profiles at R_0 and R_N, as shown in Fig. 4.6B, C and D respectively, and they all match excellently with experimental observations.

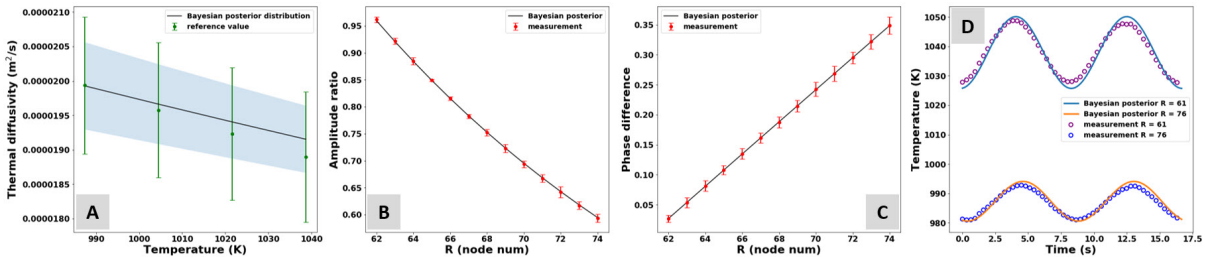

Figure 4.6: Random walk Metropolis-Hasting sampler results: (A) Estimated thermal diffusivity as a function of temperature vs reference values[3]. (B) Simulated amplitude decay vs experimental measurements. (C) Simulated phase shift vs experimental measurements. (D) Simulated temperature profiles at R_0 and R_N vs experimental measurements.

Conventional random walk Metropolis-Hasting sampler produces acceptable results. However, relatively high auto-correlation still exist for all four parameters as shown in Fig. 4.5B1-B4, and even after more than 500 accepted samples, high auto-correlation are observed. To achieve better mixing and lower auto-correlation for all parameters, a different mechanism to explore the posterior distribution other than locally constrained random walked is required. In the next section, we demonstrate improved results using a NUT sampler.

4.2.2.3 The No-U-Turn sampler

We employ the python module "pymc3"[103] to construct the NUT sampler, and we customize the code[7] to be compatible with the PC surrogate models. We use four different chains to sample the posterior distribution in Eq. 4.22 and the trace plots are shown in Fig. 4.7A1-A4. Better mixing for all four parameters are observed, and the corresponding auto-correlation shown in Fig. 4.7B1-B4 are significantly lower compared to that obtained with random walk (Fig. 4.5B1-B4). The histograms are given in Fig. 4.7C1-C4 respectively. The Gelman-Rubin criteria is also employed here to examine the convergence of the sampling process. The $\hat{R}$ value for parameters $\sigma_{solar}, A_\alpha, B_\alpha, T_{bias}$ are 1.007, 1.001, 1.001 and 1.007 respectively, indicating good convergence.

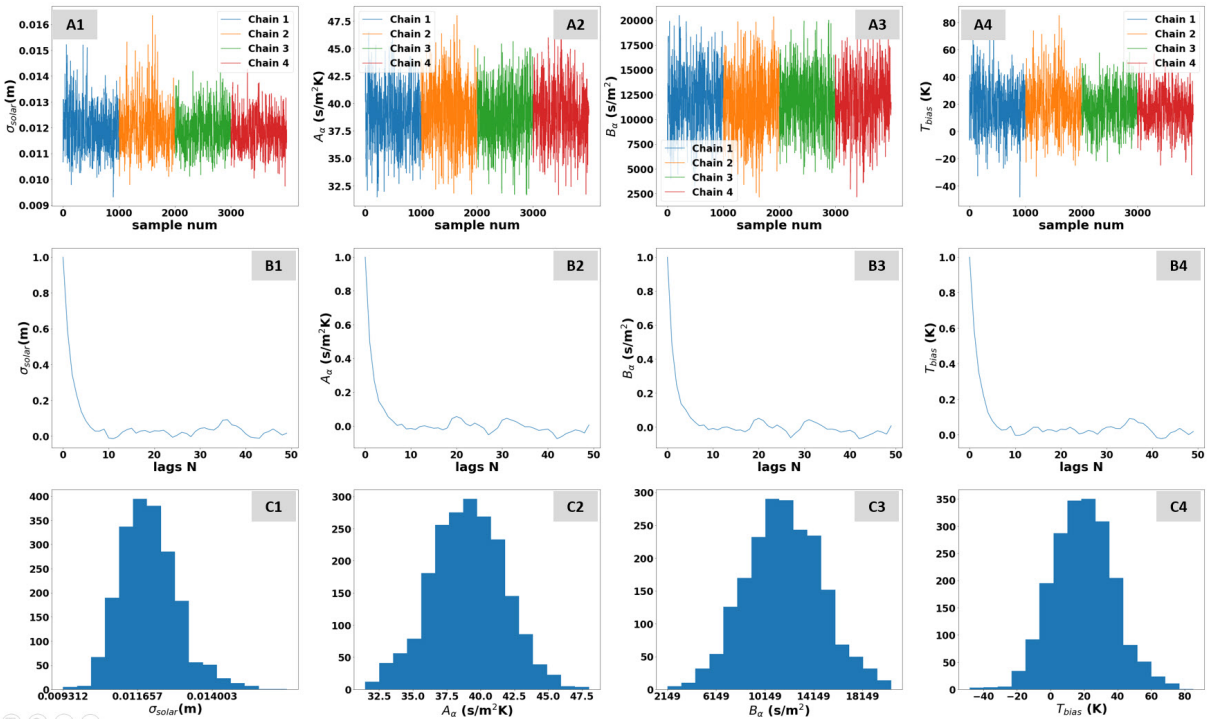

Figure 4.7: NUT sampling results. (A1-A4) Trace plots of $A_\alpha, B_\alpha, \sigma_{solar}, T_{bias}$ using four chains. (B1-B4) Auto-correlation of the trace plots in (A1-A4). (C1-C4) Histogram plots of the random samples shown in (A1-A4).

The posterior distribution for the temperature-dependent thermal diffusivity is comparable to that obtained using the random walk Metropolis-Hasting method, and the result also matches well with reference values of the graphite sample[3] as shown in Fig. 4.8A. The simulated amplitude decay, phase shift and temperature profiles using the posterior means of θ also match well with experimental measurements, as shown in Fig. 4.8 B-D.

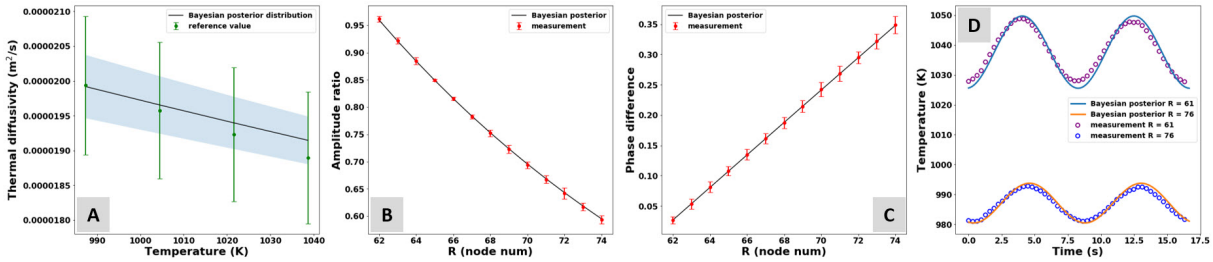

Figure 4.8: NUT sampler results: (A) Estimated thermal diffusivity as a function of temperature vs reference values[3]. (B) Simulated amplitude decay vs experimental measurements. (C) Simulated phase shift vs experimental measurements. (D) Simulated temperature profiles at R_0 and R_N vs experimental measurements.

We further examine the pairwise plot for all four parameters as shown in Fig. 4.9. We note σ_{solar} has relatively strong positive correlation with T_{bias} and is uncorrelated with A_α and B_α. This matches with the physical intuition. With increased σ_{solar}, less energy flows into the sample from the light source, and T_{bias} must increase to irradiate more power from the surroundings so that simulated temperature profiles match with experimental measurements. A_α and B_α exhibit strong negative auto-correlation but show little dependence on σ_{solar} and T_{bias}. This is also expected from the model because according to Eq. 3.2, an increase in the value of A_α must lead to the reduction of B_α for a specific thermal diffusivity value. The pairwise plot provides insights to the physical model that are difficult to acquire from conventional regression approaches[101].

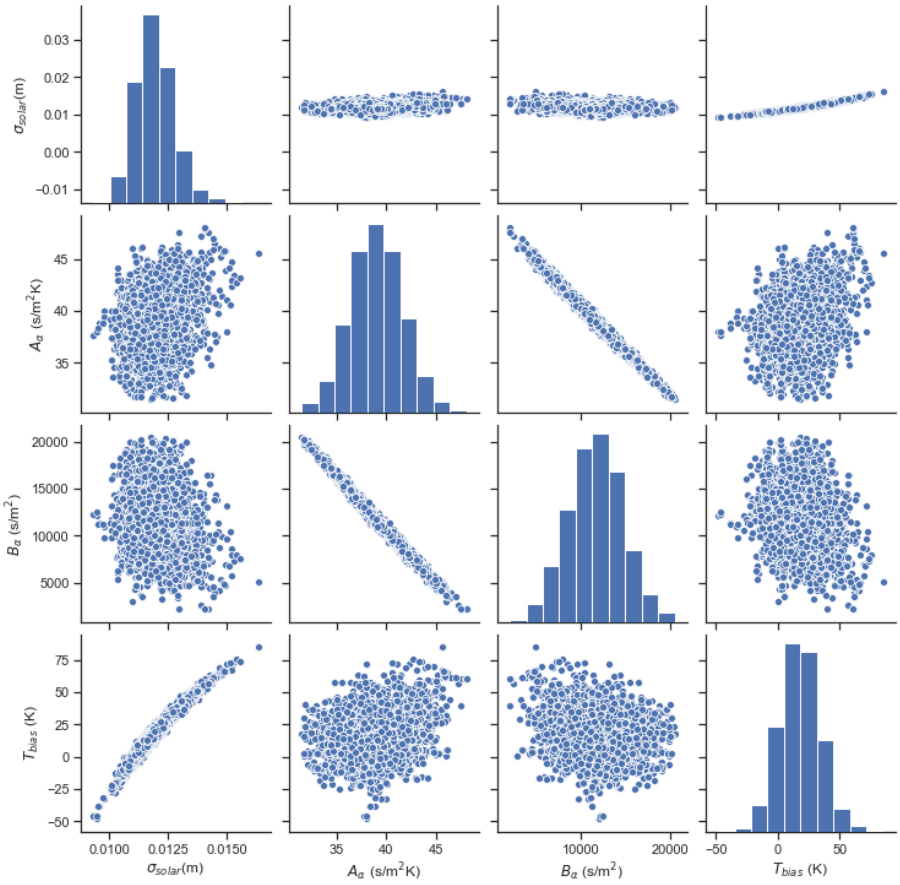

Figure 4.9: Pairwise plot for random samples obtained using the NUT sampler. The plots on the diagonal are histograms for each parameter and the off-diagonal pairwise plots indicate correlation between all pairs of unknown parameters.

4.3 Conclusion

In this study, we present several approaches to solve the inverse problem to characterize thermal diffusivity at high temperatures using a modified Ångström's method. Conventional regression approach attempts to uncover the "true" underlying values of unknown parameters. However, because of the nonlinear nature of the system, increased number of unknown parameters and the existence of noise in the observed data, obtaining an unique solution is impossible. Therefore, we treat the unknown parameters as random variables and employ a Bayesian framework for uncertainty quantification. Two major challenges

are addressed in this study. First, sampling the posterior distribution requires extensive and successive evaluation of the physical model, which is infeasible if the physical model is computationally expensive. We present a computationally cheap surrogate model using a fourth order polynomial chaos, which offers both high accuracy (approx. 0.5% maximum relative error) and nearly four orders of magnitude of speed improvement. Second, for commonly used random walk Metropolis-Hasting sampler, with increased number of unknown parameters, exploring the posterior distribution using random walk becomes inefficient. We employ a NUT sampler which explores the parameter space much more thoroughly and does not require any hyperparameter tuning. Better mixing and significantly lower autocorrelation are obtained compared to the random walk Metropolis-Hasting approach. The posterior distribution of thermal diffusivity matches excellently with reference values. Meanwhile, simulated amplitude decay, phase shift and temperature profiles using the posterior means fit well to experimental measurements. We created an open-source python module "pyangstromHT"[68] for this project to benefit researchers with similar experimental setups to analyze their results using the surrogate-accelerated Bayesian framework.

CHAPTER 5

Rapid Analytical Instrumentation for Electrochemical Impedance Spectroscopy Measurements

5.1 Experimental setup

This section presents the hardware with an adaptive shunt resistance and the corresponding impedance measurement procedure that enables accurate EIS measurements over the frequency band from 10 mHz to 2 kHz.

5.1.1 Experimental hardware

The impedance of a supercapacitor is commonly measured using Ohm's law with a four-probe circuit, as shown in Fig. 5.1A. Here, the supercapacitor is connected in series with a shunt resistor with known resistance R_S. A voltage perturbation of amplitude V is applied across the shunt resistor and the supercapacitor, and the impedance Z_C is determined from the voltage drop across the shunt resistor V_S and the supercapacitor V_C using Ohm's Law:

$$Z_C = \frac{V_C}{I_C} = \frac{V_C}{V_S} R_S = \frac{V - V_S}{V_S} R_S \tag{5.1}$$

This method is accurate when both the voltage across the shunt resistor and the voltage across the supercapacitor can be accurately measured. However, when the impedance of the supercapacitor is significantly higher or lower than the shunt resistor, because the total amplitude V is fixed, then V_S or V_C becomes too low to measure accurately, given random noise and quantization error in the circuit (see Fig. 5.1B). For a supercapacitor, its impedance changes by orders of magnitude over a broad frequency band. Therefore, measuring EIS

using a fixed shunt resistance is inappropriate over the entire frequency band.

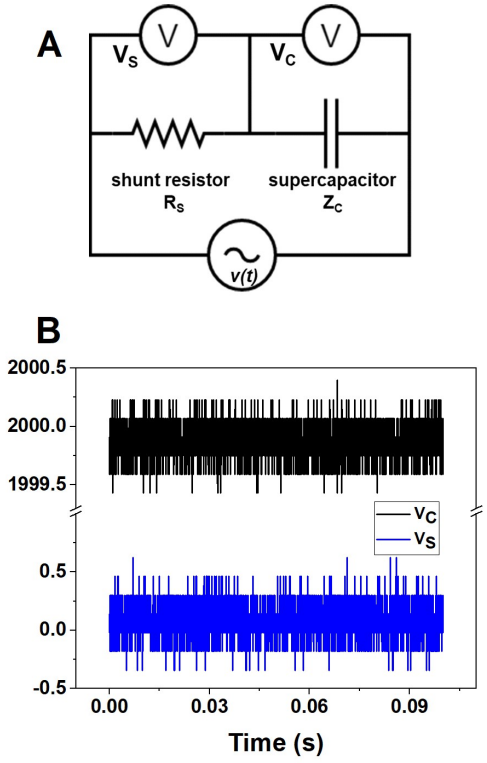

Figure 5.1: (A) A typical four-probe circuit for measuring impedance of a capacitor (Z_C) via a shunt resistor (R_S). (B) Random voltage noise across the shunt resistor $v_S(t)$ and the fully charged (at 2 V) supercapacitor $v_C\,(t)$ before perturbation signals are applied to the circuit.

To illustrate this effect with a chirp voltage signal as the perturbation signal, the impedance of a commercial supercapacitor (manufacturer: Nichicon, capacitance: 1 mF) was measured using the circuit shown in Fig. 5.1A with fixed shunt resistance of 99.9 Ω. First, we performed EIS measurements at low frequencies from 10 mHz to 1 Hz. The details of signal processing and EIS calculations using chirp signals are given in the Supplemental Materials (section S1).

Here an exponential chirp perturbation (f_0=10 mHz, f_1=1 Hz, T=150 s) was chosen was the input voltage $v\,(t)$, and the voltages across the shunt resistor $v_S(t)$ and the supercapacitor $v_C(t)$ were measured and are shown in Fig. 5.2A. The frequency of the chirp signal as

a function of time is shown as a dashed blue line. For $t < 80$ s, which corresponds to frequencies from 10 mHz to 0.1 Hz, the impedance of the supercapacitor is much higher than the shunt resistance. Therefore, the voltage across the shunt resistor $v_S(t)$ is too low to be measured accurately, as indicated by the shaded area in Fig. 5.2A. As a result, EIS results calculated using $v_S(t)$ and $v_C(t)$ are also inaccurate, as shown in Fig. 5.2B, in which measurement results obtained using the custom instrument significantly deviate from those obtained by a commercial instrument (Gamry, interface 1010B).

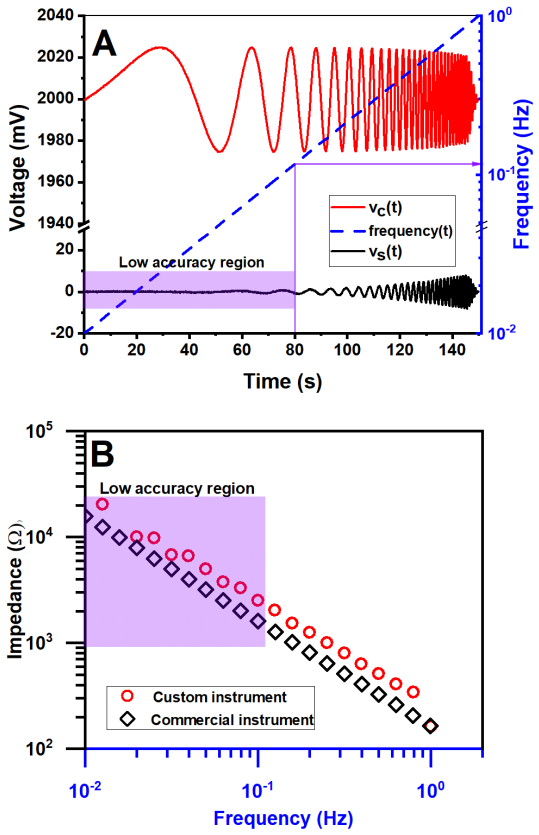

Figure 5.2: EIS measurement for the commercial supercapacitor from 10 mHz to 1.0 Hz. (A) Voltage across the shunt resistor $v_S(t)$, voltage across the supercapacitor $v_C(t)$ and frequency of the chirp signal as functions of time. The shaded area indicates the low accuracy region, in which $v_S(t)$ is too low to measure accurately. (B) Bode plots for impedance results measured using the custom and commercial instruments; the shaded area indicates the frequency band for the low accuracy region in (A).

Similarly, we measured EIS at relative higher frequencies (1 Hz to 2 kHz) for the same supercapacitor using the same shunt resistance. Here an exponential chirp perturbation ($f_0 = 1$ Hz, f_1=2 kHz, $T = 1$ s) was applied to the circuit, and the measured $v_S(t)$ and $v_C(t)$ are shown in Fig. 5.3A. Note for $t > 0.55$s, which corresponds to frequencies from 100 Hz to 2 kHz, the impedance of the supercapacitor is much lower than the shunt resistance. As a result, $v_C(t)$ is too low to be measured accurately, as indicated by the shaded region in Fig. 5.3. Consequently, the EIS results computed from $v_S(t)$ and $v_C(t)$ also deviate from those obtained from the commercial instrument, as shown in the shaded region in Fig. 5.3B.

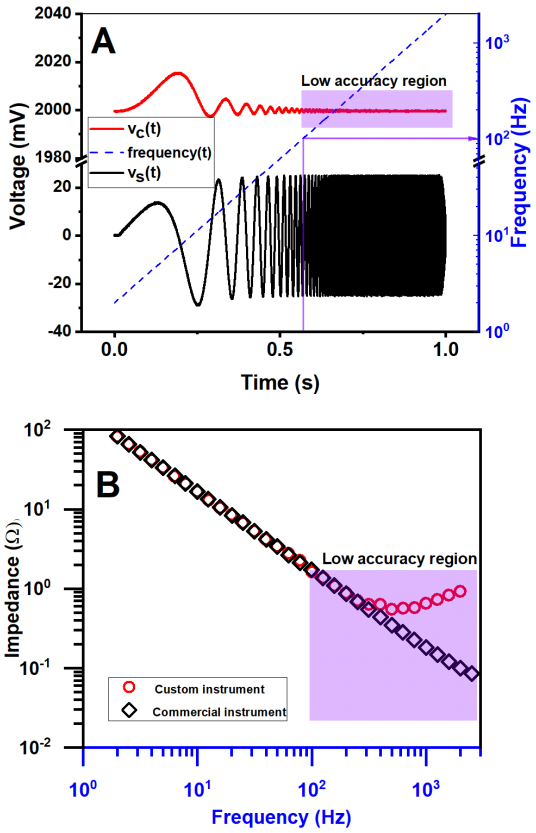

Figure 5.3: EIS measurement for the commercial supercapacitor from 1 Hz to 2 kHz. (A) Voltage across the shunt resistor $v_S(t)$, voltage across the supercapacitor $v_S(t)$ and frequency of the chirp signal as functions of time. The shaded area indicates the low accuracy region, in which $v_C(t)$ is too low to measure accurately. (B) Bode plots for impedance results measured using the custom and commercial instruments, the shaded area indicates the frequency band for the low accuracy region in (A).

As previously demonstrated, a four-probe circuit with fixed shunt resistance cannot achieve accurate EIS results over broad frequency bands for supercapacitors. To overcome this problem, different shunt resistances should be assigned for EIS measurements in different frequency subbands. The shunt resistance should be comparable to the impedance of the supercapacitor in each frequency subband, to ensure that voltages across both the shunt resistor and the supercapacitor are much higher than the random noise in the circuit and quantization error of the data acquisition system. Consequently, we implemented a resistor

bank that consists of approximately logarithmically scaled resistances. The resistors are all high-precision metal film resistors: 2.73 Ω, 10.10 Ω, 99.9 Ω, 998.5 Ω, 10.0 kΩ, 100 kΩ. Each resistor is connected to a signal relay in series, and six such resistor-relay units are connected in parallel. Assigning a shunt resistance to the circuit is achieved by switching on appropriate relays, which are controlled by a digital I/O module of the data acquisition (DAQ) board (National Instruments, USB-6351). The relays are single pole single throw (SPST) low signal relays (Omron, G6L-1P DC5) with very low contact resistance. A schematic of the resulting circuit is shown in Fig. 5.4.

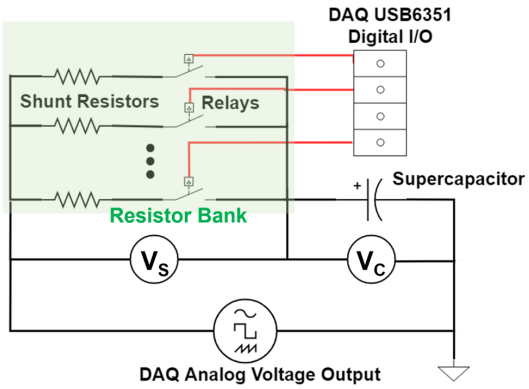

Figure 5.4: Schematic of the circuit for current measurement. The shaded area indicates resistor bank, which connects an appropriate shunt resistor to the circuit via a signal relay.

To measure the impedance of a supercapacitor, it is connected in series with the resistor bank as shown in Fig. 5.4. An exponential chirp voltage signal is applied across the resistor bank and the supercapacitor using an analog voltage output channel of the DAQ board; the voltages across the resistor bank and the supercapacitor are measured by two differential analog voltage input channels of the DAQ board. To achieve reliable electrical connections, the shunt resistors and signal relays are soldered onto a printed circuit board with screw terminals to connect to the DAQ board. Previous studies demonstrate effective electrochemical instrumentation using LabVIEW software [111]. In this work, the instrument is automatically controlled via LabVIEW software and details of the software architecture and user interface are presented in the Supplemental Materials (section S2).

5.1.2 Adaptive measurement algorithm

This section presents details of an adaptive algorithm that works in concert with the custom circuit board, i.e., to split a frequency band for EIS measurements into subbands and to assign appropriate chirp signals and shunt resistances accordingly. In the software of the custom instrument, a user is required to specify a frequency band [f_{min}, f_{max}], bias voltage V_{DC} for EIS measurements and estimated capacitance $\hat{C}$ of the supercapacitor (that need not be accurate). The user-specified frequency band [f_{min}, f_{max}] is divided into subbands such that adaptive shunt resistances and different chirp signals can be applied in each frequency subband. In this work, each subband is two decades wide initially (e.g., the first frequency subband is [f_{min}, $100 \times f_{min}$]), and measurements begin from the lowest frequency f_{min} and end at the highest frequency f_{max}. To select a shunt resistor for the first frequency subband, the resistance value is chosen according to the estimated impedance of the supercapacitor based on the estimated capacitance $\hat{C}$:

$$\hat{Z}_C \approx \left| \frac{1}{2\pi f \hat{C}} \right| \tag{5.2}$$

where f is the frequency. According to Eq. 5.2, the maximum impedance is obtained at the lowest frequency in the frequency band. Therefore, based on user input, the estimated maximum impedance in the first frequency subband is $\hat{Z}_{C,max} \approx \left| 1/2\pi f_{min} \hat{C} \right|$. Based on $\hat{Z}_{C,max}$, the instrument selects a shunt resistance that is comparable to the maximum impedance:

$$x_s < \left| \hat{Z}_{C,max} / R_S \right| < x_b \tag{5.3}$$

where R_S is the shunt resistance, and x_s and x_b are lower and upper bounds and set to 1.5 and 15, respectively. These limits ensure that the maximum impedance is at least 1.5 times larger than the shunt resistance but no more than 15 times larger within a given frequency subband. The performance of the instrument is relatively insensitive to the specific values of x_s and x_b. The choice of x_s can be any value between 1 and 3; however, x_b should satisfy $x_b = 10x_s$ to be compatible with the logarithmically scaled shunt resistances in the resistor bank.

Based on the estimated impedance of the supercapacitor using Eq. 5.2, the instrument connects a shunt resistor (computed using Eq. 5.3) from the resistor bank to the circuit using signal relays. The instrument then applies a chirp signal to the circuit ($f_0, = f_{min}$, $f_1 = 100 \times f_{min}$, $T = 3/(2f_{min})$) and simultaneously measures the voltage across the shunt resistor $v_S(t)$ and the supercapacitor $v_C(t)$. The impedance spectrum is then calculated (see Supplemental Materials section S1 for details) within this frequency subband. If the actual measured maximum impedance $Z_{C,max}$ does not satisfy Eq. 5.3, possibly because of incorrect estimation of the capacitance from the user input, the instrument selects a different shunt resistor using Eq. 5.3 based on the updated EIS results $Z_{C,max}$, and EIS measurements are repeated for the same frequency subband. If $Z_{C,max}$ satisfies Eq. 5.3, the instrument checks if impedances in the entire frequency subband are comparable to R_S using the same criteria:

$$x_s < |Z_C(f)/R_S| < x_b \tag{5.4}$$

Because the impedance of supercapacitors decreases when frequency increases, Eq. 5.4 may not hold for the entire frequency subband. In this case, the software computes the frequency f^* up to which the impedance of the supercapacitor is comparable to the shunt resistance:

$$|Z_C(f^*)/R_S| \approx x_s \tag{5.5}$$

EIS results from f_0 to f^* are saved, and EIS results from f^* to f_1 are discarded to guarantee that the measured impedance is not significantly lower than the shunt resistance. The instrument then continues EIS measurements from f^*. First it selects an appropriate shunt resistance for the new frequency subband ($f_0 = f^*$, $f_1 = 100 \times f^*$) according to Eq. 5.4 to account for reduced impedance with increased frequencies. Then the instrument waits until bias voltage stabilizes at V_{DC} and applies a chirp signal ($f_0 = f^*$, $f_1 = 100 \times f^*$, $T = 3/(2f^*)$) for EIS measurements in the new frequency subband. The same procedure repeats until the entire frequency band is scanned. The pseudo-code for the adaptive EIS measurement algorithm and an example that demonstrates the algorithm step-by-step using a commercial supercapacitor (manufacturer: Nichicon, 1mF) are presented in the Supplemental Materials (section S3).

5.2 Results and Discussions

5.2.1 Adaptive algorithm and EIS results for a commercial supercapacitor

The commercial supercapacitor (Manufacturer: Nichicon, capacitance 1 mF) was measured using the adaptive algorithm. The frequency band of EIS measurements is from 10 mHz to 2 kHz under 2.0 V bias voltage, and the corresponding EIS results are shown in Figs. 5.5A and B. The data from the custom instrument are shown as red circles, and the corresponding uncertainties are shown as blue shaded bands. The details of computing measurement uncertainties are presented in the Supplemental Materials (section S4). Fig. 5.5C indicates the automatically selected shunt resistance used for impedance measurements in different frequency subbands. To verify measurements obtained by the custom instrument, EIS were also performed using the commercial instrument (Gamry interface 1010B) under identical conditions, and the results are shown as solid black lines. Because of appropriate application of shunt resistance in different frequency subbands, high signal-to-noise ratios for $v_S(t)$ and $v_C(t)$ are obtained over the entire frequency band (10 mHz to 2 kHz). Therefore, EIS results (impedance and phase results) match well with those obtained from the commercial instrument. The detailed procedure to reproduce Figs. 5.5A and B using the adaptive algorithm is provided in the Supplemental Materials (section S3).

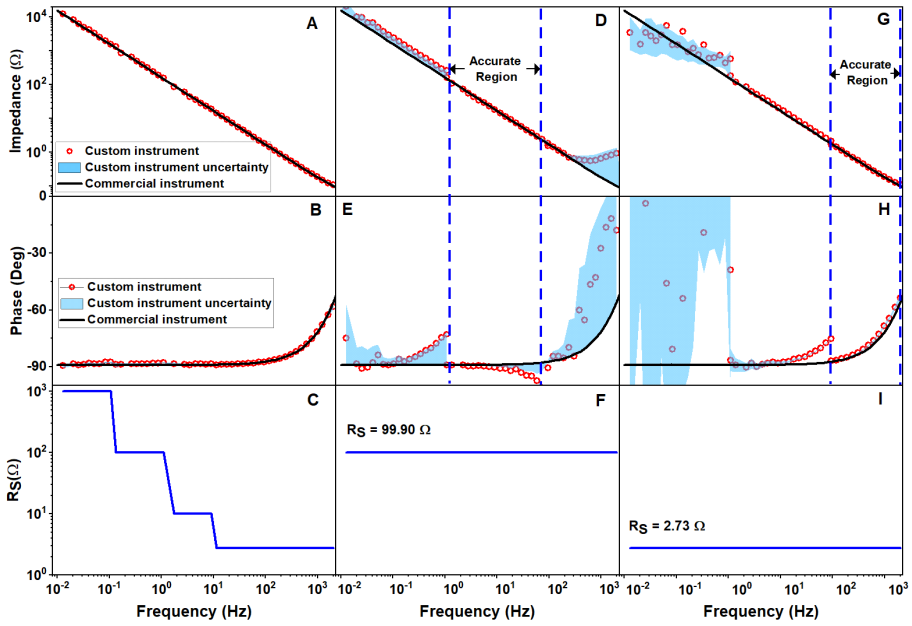

Figure 5.5: EIS results for a commercial supercapacitor (manufacturer: Nichicon, capacitance: 1 mF). Left panel): Impedance (A), phase (B) and shunt resistance (C) at different frequencies for EIS conducted using adaptive shunt resistances. (Center panel): Impedance (D), phase (E) and shunt resistance (F) at different frequencies for EIS conducted using fixed 99.9 Ω shunt resistance. (Right panel): Impedance (G), phase (H) and shunt resistance (I) at different frequencies for EIS conducted using fixed 2.73 Ω shunt resistance.

To demonstrate the benefits of the adaptive shunt resistance, EIS measurements were also conducted using a fixed shunt resistance of $R_S = 99.9\Omega$ and $R_S = 2.73\Omega$ respectively. Note that these two resistances were applied in Fig. 5.5C, but only for a portion of the entire frequency band. The results are shown in Figs. 5.5D, E and Figs. 5.5G, H, respectively. Here the frequency band (10 mHz to 2 kHz) was scanned by 2 decades each time ([10 mHz - 1 Hz], [1 Hz - 100 Hz], [100 Hz - 2 kHz]), but the shunt resistance remained the same. In Figs. 5.5D and E, for a shunt resistance of 99.9Ω, the EIS results are accurate only when the impedance of the supercapacitor is comparable to the shunt resistance, as indicated by the region between the two dashed lines. Similarly, in Figs. 5.5G and H, for a shunt resistance of 2.73Ω, the EIS results are accurate only at high frequencies where the supercapacitor

impedance is low, as indicated by the region between two dashed lines.

To conclude, because supercapacitor impedance typically varies by several orders of magnitude at different frequencies, EIS measurements using one shunt resistance yields satisfactory results only at frequencies for which the impedance of the supercapacitor is comparable to the shunt resistance. This illustrates the need for using adaptive shunt resistance in EIS measurements over broad frequencies. In the following section, six laboratory-fabricated carbon nanotube (CNT) based supercapacitors were measured to further asses the effectiveness of the custom instrument.

5.2.2 EIS Results for laboratory-fabricated CNT-based supercapacitor pouch cells

To validate the performance of the custom instrument, EIS scans of six CNT-based supercapacitor cells fabricated at YTC America were performed. EIS scans for the pouch cells were also performed by the commercial instrument (Gamry Interface 1010B) under identical conditions for comparison. Detailed information regarding the pouch cells is available in previous studies [135][29][30]. Among the six pouch cells, three used acetonitrile (ACN) electrolyte, and the other three used propylene carbonate (PC) electrolyte. The ESR (impedances at 1 kHz) for ACN and PC cells were approximately 200 mΩ and 500 mΩ respectively. The capacitances of ACN and PC cells were approximately 40 mF. The frequency band for the EIS measurement was from 10 mHz to 2 kHz, ten data points were collected per frequency decade, and the bias voltage was 2.0 V. The impedance and phase measurement results for ACN and PC cells are shown in Figs. 5.6 and 5.7 respectively. The red circles indicate EIS results obtained using the custom instrument, and the solid black lines indicate results obtained using the commercial instrument. Measurement uncertainties for the custom instrument are shown as blue shaded bands. Magnified uncertainty interval is shown for samples ACN #1 and PC #1.

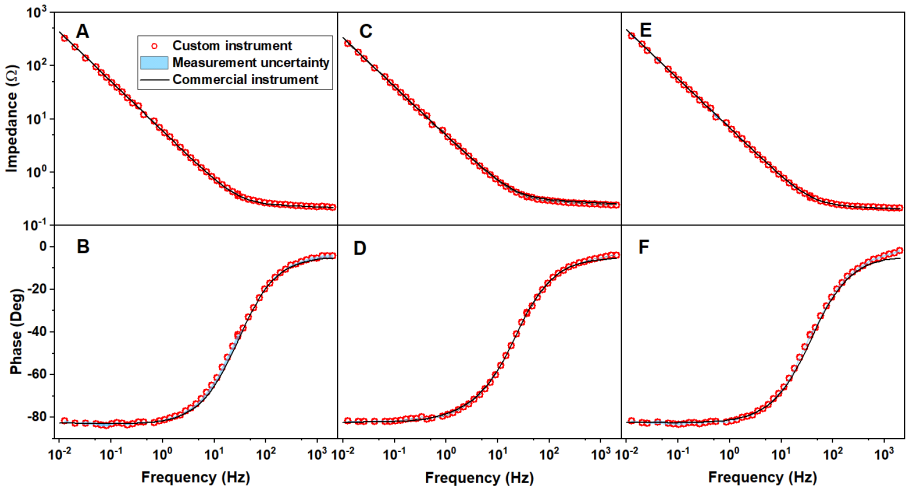

Figure 5.6: EIS measurement results for ACN samples: (A-B) Impedance and phase results for ACN sample 1. (C-D) Impedance and phase results for ACN sample 2. (E-F) Impedance and phase results for ACN sample 3.

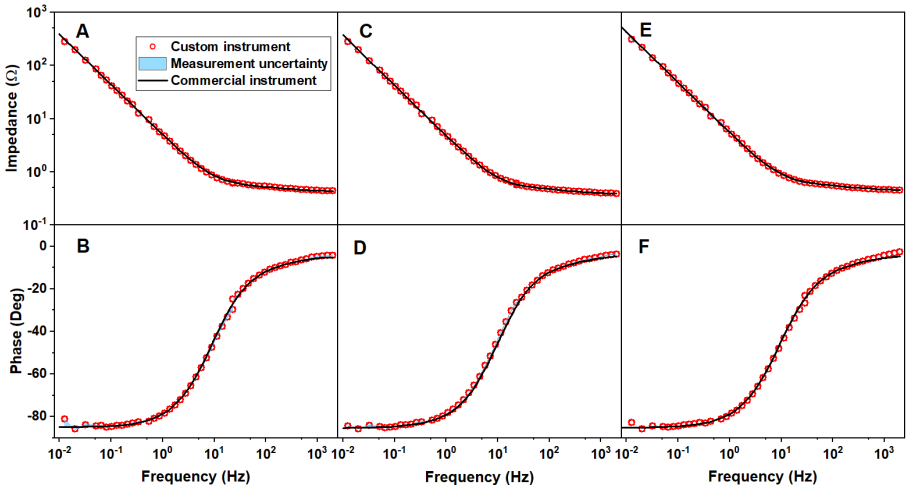

Figure 5.7: EIS measurement results for PC samples: (A-B) Impedance and phase results for PC sample 1. (C-D) Impedance and phase results for PC sample 2. (E-F) Impedance and phase results for PC sample 3.

As indicated, EIS measurements for all six pouch cells exhibit good agreement with the results from the commercial instrument, as well as low uncertainties over the entire frequency

band, as indicated by narrow blue shaded bands in Figs. 5.6 and 5.7.

5.2.3 Measurement time reduction

Compared to a sinusoidal sweep, measurement time is significantly reduced using the exponential chirp signal for two reasons:

1. A chirp signal scans a broad band of frequencies, whereas the sinusoidal sweep scans only one frequency at a time.

2. Multiple periods are typically required to obtain satisfactory results at one frequency using sinusoidal sweep. In the chirp signal approach, satisfactory measurement results can usually be achieved with a single scan. More scans are required in the presence of measurement outliers. The instrument detects outliers by calculating the second-order central difference of both impedance and phase results as a function of frequency, and repeats the measurement should outliers are detected.

The cumulative time for EIS measurement for the commercial supercapacitor (see Figs. 5.5A, B and C) is illustrated in Fig. 5.8A. EIS measurements start at low frequency and end at high frequency, and the cumulative time indicates time required to scan from the initial to current frequency f.

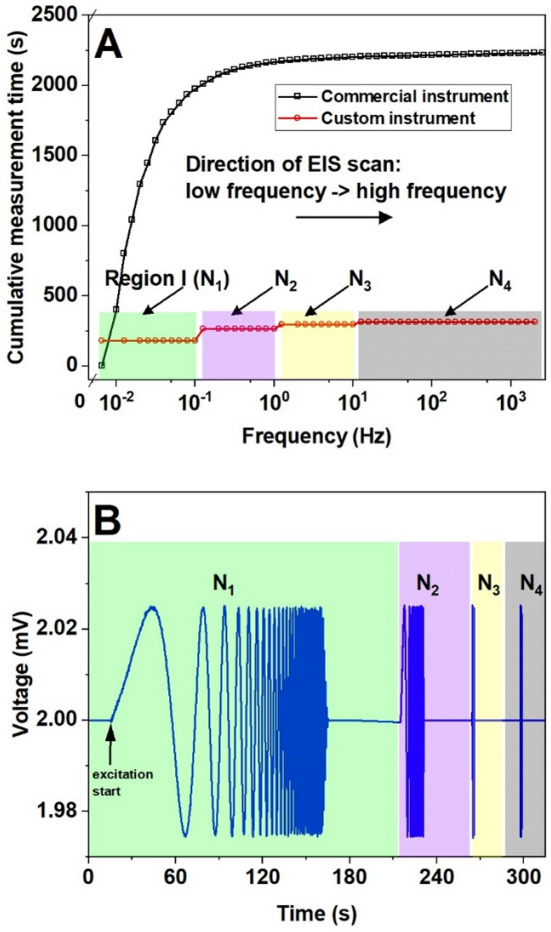

Figure 5.8: (A) Cumulative EIS measurements over time for a commercial instrument (black line) and the custom instrument (red line). EIS results were obtained using four chirp excitations, and the frequency range for the EIS results are N_1, 10 mHz to 0.1 Hz (green region); N_2, 0.1 Hz to 1 Hz (purple region); N_3, 1 Hz to 10 Hz (yellow region); N_4, 10 Hz to 2000 Hz (gray region). (B) Chirp excitation signals applied to obtain EIS results in the corresponding frequency region of (A). With each chirp excitation and response measurement, EIS results are acquired over the range of frequencies in the corresponding chirp signal with a single scan.

As shown in Fig. 5.8A, most of the measurement time for the sinusoidal scan is spent at low frequencies (10 mHz to 0.1 Hz). EIS results in this frequency range (N1, highlighted in green) can be covered using a chirp signal in a single scan. In an exponential chirp

signal, the device is excited by voltage signals spanning a given frequency range, and the corresponding impedance data are recorded. For example, the excitation chirp signal shown in Fig. 9B (green region) was applied to the circuit with the response voltage measurements on both the supercapacitor and the shunt resistor. Based on the response signals, EIS results for this frequency range were calculated and shown in Fig. 5.8A in the green region. EIS results in N_2, N_3 and N_4 in Fig. 5.8A were similarly obtained, and the corresponding chirp excitation signals are shown in Fig. 5.8B. Therefore, several step profiles are observed in the cumulative time plot. The flat portion between chirp excitations indicate waiting period for the instrument to reach steady state under dc bias before applying the next chirp excitation.

The overall measurement time for the chirp signal approach using the custom instrument was 314 sec, as compare to 2231 sec for the sinusoidal sweep approach using the commercial instrument in the same frequency range.

Similarly, EIS measurement times for the CNT-based supercapacitors (see Figs. 5.6 and 5.7) were reduced by 73 % on average compared to the measurement times of the commercial instrument. A comparison of measurement times between the custom instrument and the commercial instrument is shown in Fig. 5.9.

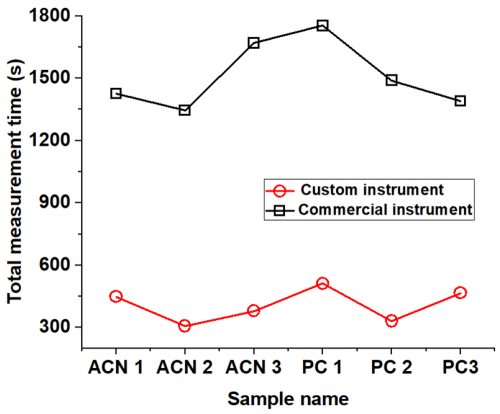

Figure 5.9: Measurement time for CNT-based supercapacitor samples.

5.2.4 Other potential applications:

EIS characterizations are widely used in other electrochemical studies, such as Li-Ion batteries, fuel cells, solar cells and gas sensing. Here, we briefly discuss how the custom instrument could be potentially used in these applications.

Several recent Li-Ion battery studies measured EIS results from a few hertz to several kilohertz [116][89]. The current densities were relatively low and can be accommodated using the custom instrument. However, as compared to supercapacitors, the impedance of Li-Ion batteries is typically lower. To enable precise low impedance measurements, several high-precision shunt resistors with low resistance would be required in the resistor bank. Also, higher resolution (18-24 bit) of the analog voltage inputs and outputs would be required to acquire smaller voltage perturbations due to low impedance. With these modifications, the custom instrument would be a reliable tool for EIS measurements for Li-Ion batteries.

Fuel cells are also an applicable field for the custom instrument. Typically, EIS scans are measured from millihertz to kilohertz ranges [52][99]. Like supercapacitors, the impedance of fuel cells changes significantly in different frequency ranges. Therefore, the custom instrument would potentially efficient for such measurements. However, for fuel cells, currents are typically much higher (>1A) in EIS experiments. To increase the current capability, a programmable power amplifier could be employed to work with the other hardware for this application.

Solar cells are another promising research area for EIS diagnostics. Previous studies have typically measured EIS over millihertz to kilohertz frequency ranges [38][76]. Like supercapacitors, the impedance of solar cells changes significantly over different frequencies. In addition, the current levels in EIS measurements are relatively low. Therefore, the custom instrument could be potentially adapted for solar cell characterizations.

Another applicable field for the custom instrument is EIS gas sensing. A recent study employing EIS techniques for ammonia sensing [80] measured impedance under bias voltage from a few hertz to several MHz. The maximum sampling rate of the hardware of the present

instrument is 1 MHz; therefore the maximum frequency signal for reliable EIS results is approximately 100 kHz. However, the frequency band in which impedance is sensitive to gas concentration typically ranges from approximately 10 Hz to 100 kHz. Therefore, the present instrument would likely produce meaningful results.

5.3 Conclusion

In this work, an adaptive and versatile instrument has been developed to perform EIS measurements. The instrument employs adaptively selected shunt resistors from a resistor bank and different chirp signals to conduct EIS measurements over different frequency subbands, enabling accurate impedance measurements for a broader frequency band (10 mHz to 2 kHz) as compared to previous studies employing chirp signals. Accurate results were shown for six laboratory-fabricated CNT-based supercapacitors and a typical commercial supercapacitor under 2.0 V bias voltage. The frequency band scan strategy enables accurate EIS measurements over a broad frequency band. Therefore, the approach is also likely to be suitable for other electrochemical systems, such as Li-Ion batteries, solar cells, fuel cells and gas sensors. However, in rare cases, when impedance oscillates significantly within a frequency subband, the adaptive algorithm will require the splitting of frequency subbands significantly, resulting in lower measurement efficiency. Another concern with this EIS approach is that the hardware must have a sufficient number of digital output channels. This limitation may prevent researchers from taking advantage of common hardware, such as oscilloscopes and function generators. However, the overall cost of the instrument is about $1500, which is much more affordable than regular commercial EIS instruments (typical cost > $15,000). And the custom instrument reduces measurement time by 70 % to 80 % as compared to a commercial instrument under identical EIS measurement conditions. The custom instrument's accuracy, time efficiency, customizability and low cost are expected to benefit electrochemical researchers across wide application areas of electrochemical studies.

CHAPTER 6

Suggested standards for reporting power and energy density in supercapacitor research

6.1 Introduction

Supercapacitors, with high power and energy density, long cycle life, low minimum working temperature, are widely used in hybrid vehicles, emergency electrical backup, and engine starters for low temperature applications [34]. The growing supercapacitor market stimulates researchers to develop robust and high surface area materials as electrodes that enable high power density and energy density.

Based on Google scholar data, more than 20,000 papers have been published on supercapacitors since 2014, and continuously increasing power and energy density have been reported. However, after scrutinizing published data, some inconsistencies are apparent between different papers. First, multiple methods exist for capacitance and equivalent series resistance (ESR) measurements. The most widely used techniques are three-electrode measurements for testing a single electrode sample and two-electrode techniques for sandwiched electrodes. For the same sample, the three-electrode measurement yields twice the capacitance and half the ESR compared to two-electrode measurements. Occasionally, the method used is omitted from the reporting. Second, the basis upon which power and energy density are computed are sometimes arbitrarily chosen [136]. The commonly used bases are: mass or volume of active material; mass or volume of electrode. Different basis yield orders of magnitude differences in power and energy density, yet it is not uncommon to omit the details of the bases. Third, different researchers use different scan rates for capacitance measurement.

Typically, lower scan rate yields higher capacitance and thereby higher energy density, especially for supercapacitors with pseudocapacitance. However, this should be avoided since supercapacitors typically work at very high rate of charge and discharge, as pointed out in a prior article of the field [107]. Therefore, a universal standard for reporting power and energy density is required to compare research work fairly and reduce the confusion of calculations and comparisons.

6.2 A proposed standard for reporting power and energy density

In contrast to laboratory devices, comparing power and energy density of commercial supercapacitor modules is convenient, since most of them have the same output voltage (typically 16V for DC applications) and the dimension and weight of the supercapacitor modules are available. Similarly, to make fair comparisons emerging laboratory prototypes, the power and energy density of the final product (supercapacitor modules with the same output voltage) should be evaluated. Typically, such a requirement is difficult to fulfill for research laboratories that often lack final packaging and integration solutions. Therefore, this approach suggested here 'virtually' performs the assembly process of supercapacitors and computes the power and energy density of the 'finished' supercapacitor module.

The assembly process consists of three steps as shown in Fig.6.1. First a unit electrode sample with known properties (ESR, capacitance, maximum voltage) is obtained. Multiple such unit electrodes are connected to increase surface area to achieve lower ESR and higher capacitance, as shown in Fig.6.1A [128] and 6.1B [1]. Second two electrodes from the first step are sandwiched to form a supercapacitor device, as shown in Fig.6.1B. The last step is to connect supercapacitors from step 2 in series as a supercapacitor module to achieve a given output voltage, as demonstrated in Fig.6.1C [8].

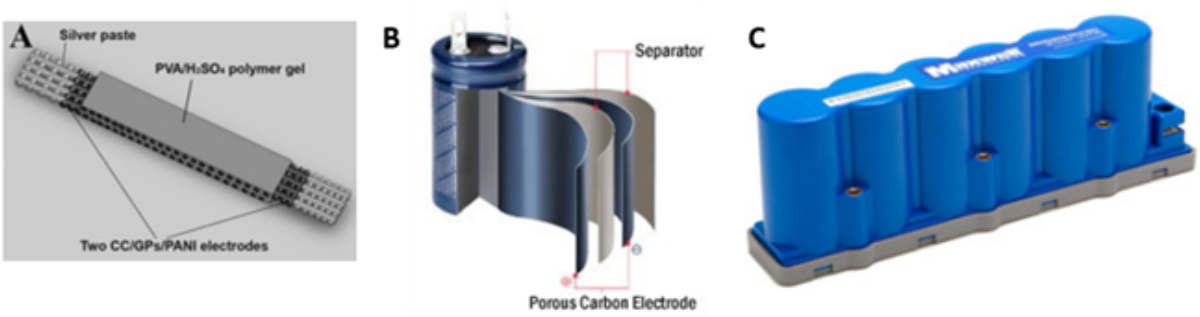

Figure 6.1: Supercapacitor module assembly process, reprinted with permission

6.2.1 Power and energy density for electrode samples measured with three-electrode setups

6.2.1.1 Extend electrode surface area

We first assume that the properties of a unit electrode are measured using three-electrode setup with equivalent series resistance R_0, capacitance C_0, and maximum working voltage V_0. The extensive property of the unit electrode, either mass or volume, is B_0. Z_0 is the impedance of the unit electrode, ω is the angular frequency, and j is the imaginary unit number. In this work, the supercapacitor is considered an ideal capacitor connected in series with an equivalent series resistor. However, most double-layer supercapacitors are represented very well by De Levie's model [44], which is essentially an infinitely parallel connection of units consisting of series connections of an ideal resistor and an ideal capacitor. Therefore, the result derived in this section is also applicable to double-layer supercapacitor.

The first step is to create a larger electrode from the sample electrode to increase capacitance as well as to reduce ESR. Assuming that the extensive property of this larger electrode (subscript 1) is B1, the impedance is:

$$Z_0 = R_0 + \frac{1}{jC_0\omega} \tag{6.1}$$

$$Z_1^{-1} = \frac{B_1}{B_0} Z_0^{-1} \tag{6.2}$$

$$Z_1 = \frac{B_0}{B_1} Z_0^{-1} \tag{6.3}$$

Therefore, the ESR is $R_0 B_0 / B_1$ and the capacitance is $C_0 B_1 / B_0$. The maximum voltage does not change because it is determined by the electrolyte.

6.2.1.2 Extend electrode surface area

The second step is to construct a full cell supercapacitor device (subscript 2) using the electrode obtained in step 1,

$$Z_2 = Z_1 + Z_1 = 2Z_z = \frac{2B_0}{B_1} R_0 + \frac{1}{j(CB_1/(2B_0))\omega} \tag{6.4}$$

Therefore, the ESR is $2B_0 R_0 / B_1$, and the capacitance is $C_0 B_1 / 2B_0$, while the maximum voltage remains the same. The extensive property is $B_2 = 2B_1$, because two individual electrodes are required to build a full cell.

6.2.1.3 Assemble into modules

The last step is to assemble the supercapacitor device from step 2 and form a supercapacitor module (subscript 3) to achieve the target voltage V_3. To achieve this goal, the supercapacitor devices must be connected in series, and the number of such device required is V_3/V_1.

$$Z_3 = \frac{B_3}{B_2} Z_2 = \frac{B_3}{B_2} R_2 + \frac{1}{j(B_2 C_2 / B_3)\omega} = \frac{4B_3}{B_0} R_0 + \frac{1}{j(B_0 C_0 / (4B_3)\omega} \tag{6.5}$$

The power density of the supercapacitor module is:

$$\frac{P_3}{B_3} = \frac{V_3^2}{4R_3 B_3} = \frac{V_3^2}{4\frac{4B_3}{B_0} R_0 B_3} = \frac{V_0^2 B_3^2 / B_0^2}{16 B_3^2 R_0 / B_0} = \frac{V_0^2}{16 R_0 B_0} \tag{6.6}$$

Similarly, for energy density:

$$\frac{E_3}{B_3} = \frac{C_3 V_3^2}{2B_3} = \frac{\frac{B_0 C_0}{4B_3} (V_0^2 B_3^2 / B_0^2)}{2B_3} = \frac{C_0 V_0^2}{8B_0} \tag{6.7}$$

As shown in Eqs. 6.6 and 6.7 the power and energy density of the supercapacitor module depends only on the properties of the unit electrode sample. Therefore, in addition to reporting equivalent series resistance and capacitance of the sample (using a three-electrode setup), the extensive property of the electrode (mass and volume) must also be reported.

6.2.2 Power and energy density for electrode samples measured with two-electrode setups

Some researchers prefer reporting the result of sandwiched electrodes using a two-electrode setup. Here, we assume that ESR is R_f, capacitance is C_f and maximum working voltage is V_f, and the extensive property of the device is B_f. The full device is assembled into a supercapacitor module with output voltage of V_3 and extensive property B_3. Exactly the same calculation steps yield the following results for energy and power density.

$$\frac{P_3}{B_3} = \frac{V_f^2}{4R_f B_f} \tag{6.8}$$

$$\frac{E_3}{B_3} = \frac{C_f V_f^2}{2B_f} \tag{6.9}$$

6.2.3 Summary

To summarize, the power and energy density can be obtained using the expression below to make objective comparisons.

$$\frac{P}{B} = \begin{cases} \frac{V_0^2}{16R_0B_0}, & \text{three } - \text{ electrode setup} \\ \frac{V_f^2}{4R_fB_f}, & \text{two } - \text{ electrode setup} \end{cases} \tag{6.10}$$

$$\frac{E}{B} = \begin{cases} \frac{C_0V_0^2}{8B_0}, & \text{three } - \text{ electrode setup} \\ \frac{C_fV_f^2}{2B_f}, & \text{two } - \text{ electrode setup} \end{cases} \tag{6.11}$$

Both results depend only on the intrinsic properties of the unit electrode or unit supercapacitor cell. The results also em-phasize the importance of reporting the appropriate exten-sive property of the unit electrode or the unit supercapacitor cell; preferably both mass and volume should be reported.

Based on Eqs. 6.10 and 6.11, power and energy density of a few widely used commercial supercapacitors [6],[8] from GreenCap, Maxwell Technologies and AVX are calculated. Currently the unit cost for the listed supercapacitor is 1.5$, 8.38$ and 3.33$ respectively. Some published results [128][74][102] where power and energy density are calculated based on

device volume are also presented in Fig.6.2. As observed all the listed commercial supercapacitors exhibit higher energy density, and in general also possess higher power density. The primary reason is lack of professional packaging and inte-gration solutions for laboratory prototypes. Still, based on the comparison laboratory prototypes still need more improvement on both power and energy density to compete with current commercial supercapacitors.

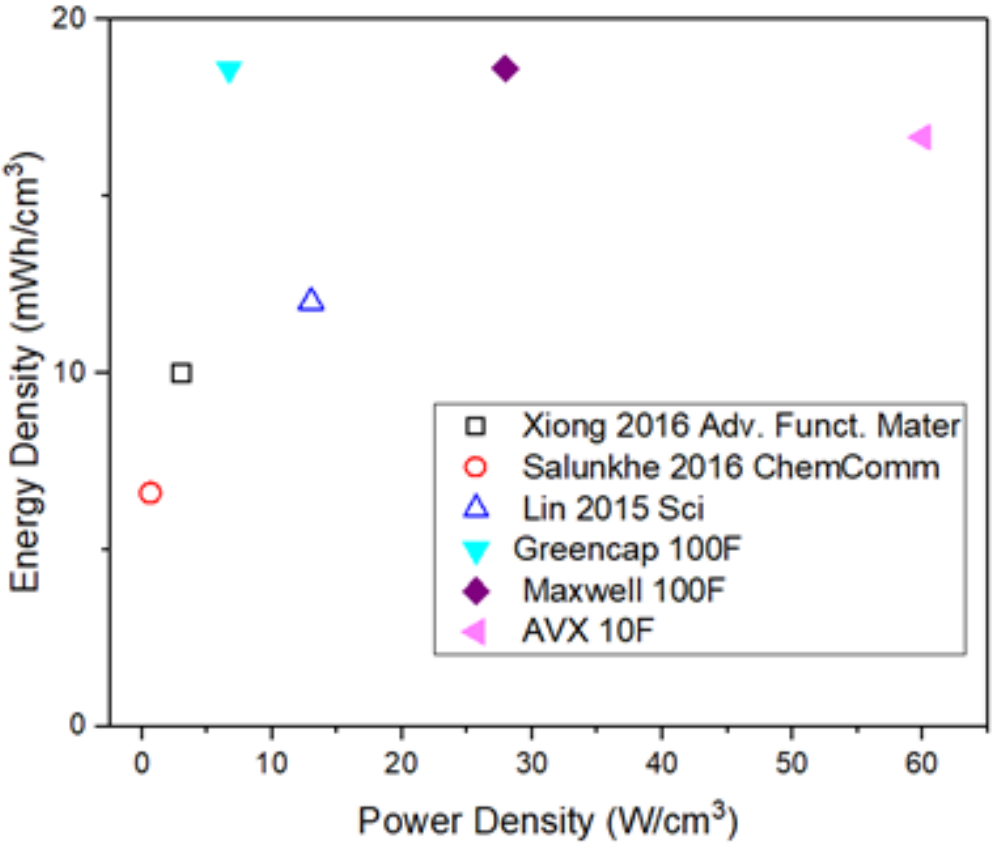

Figure 6.2: Ragone plot for commercial supercapacitors [6][8] as well as some published results [128][74][102]. The power and energy densities are calculated based on Eqs. 6.10 and 6.11.

6.3 Discussion of a widely used power density calculation method

The generally accepted approach to calculate supercapacitor power is [70]:

$$P = V^2/4R \tag{6.12}$$

where R represents the equivalent series resistance. This approach computes the maximum possible power distributed to the load, when the resistance of the load matches the ESR of the supercapacitor. Another common approach in literature [128] [84][15] for power density calculations uses the following equation:

$$P = E/\Delta t \tag{6.13}$$

$$E = CV^2/2B \tag{6.14}$$

Where V is the applied voltage, C is the capacitance of the supercapacitor, B is the extensive property of the electrode, and Δt is the discharge time under constant current.vThe flaw with using this approach is that, because the supercapacitor is discharged using a galvanostatic instrument, the discharge time does not always reflect the true current-carrying capability of the supercapacitor being tested. For galvanostatic discharge, the discharge time is:

$$\Delta t = \frac{V}{I/C} \tag{6.15}$$

where I is the galvanostatic discharge current. According to Eqs. 6.13 and 6.14:

$$P = \frac{E}{\Delta t} = \frac{CV^2 I}{2BVC} = \frac{VI}{2B} \tag{6.16}$$

The power density computed from this approach therefore depends on the current setting of galvanostatic instrument. If the current is set to higher than the shorting current, the power density obtained using Eq. 6.16 exceeds the maximum possible power output of the supercapacitor, instead of its intrinsic capacitive performance. Therefore, power density computed based on discharge in Eq. 6.13 should be avoided, and Eq. 6.12 should be used whenever possible.

6.4 Conclusions

A method for reporting power and energy density for supercapacitor research is proposed, such that objective comparisons can be made between different research studies as well as commercial products. In addition to convention-ally reported metrics such as equivalent

series resistance and capacitance, the extensive property (mass and volume) of the sample is also required. Power and energy density using this new approach are calculated for some widely used commercial supercapacitors, both results are found to be higher than some recent publications in general. Therefore, for laboratory prototypes, higher capacitance and lower ESR are needed to compete with commercial supercapacitors. Last, a commonly used approach in literature for power density computing is discussed and shown to be potentially erroneous under circumstances in which the arbitrarily chosen galvanostatic current exceeds the intrinsic capabilities of the sample under test.

CHAPTER 7

Characterizing other thermal systems

7.1 Gold nanostar laser energy heat conversion estimation

Gold nanostars (AuNSTs) have large surface areas, biocompatible and are ideal for bilogical applications. Upon irradiation with near-infrared light, AuNSTs exhibit high efficiency for light to heat conversion. Such localized heating can be controlled by laser light intensity and flow conditions, and can further facilitate cell detachment from capillary walls. The AuNST platform are potentially promising for chemical and biological sensing and drug delivery. Therefore, precise characterize light to heat conversion is crucial to understand system's thermal response under different input conditions.

We employ conservation of energy to estimate the power converted from laser to heat. Consider the control volume shown in Fig. 7.1A. Because the temperature rise (typically less than 5°C is relatively low; we neglect heat loss to the ambient air. In addition, because the thermal conductivity of the capillary tube is low (1.2W/m K) we neglect heat losses via capillary conduction. Therefore, the laser power converted to heat is approximately represented by the temperature difference of water between the inlet and the outlet of the control volume. Because the capillary wall is thin (0.070 mm thickness), we also neglect the temperature difference between the inner and outer surface of the capillary; consequently, the temperature of the water is approximated by the temperature of the outer surface of the capillary. Capillary surface temperatures were recorded by an infrared (IR) camera (A655sc, 25 μm close-up lens), and an IR image for the capillary with water flow under laser heating is shown in Figure 7.1B.

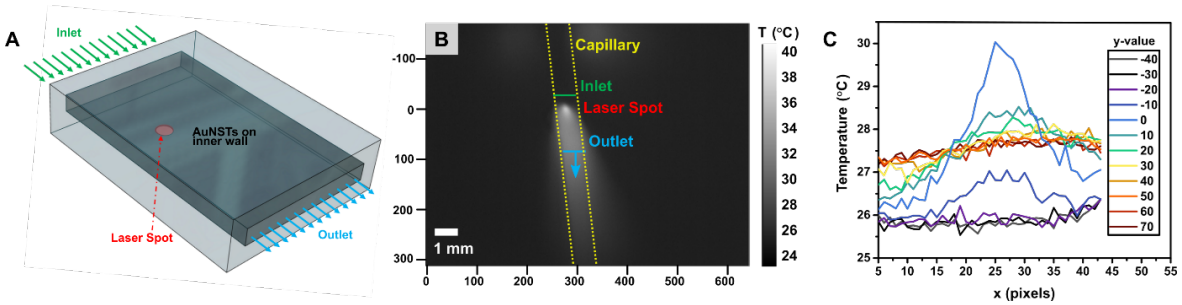

Figure 7.1: A: Schematic of system. B: Thermal image showing capillary under irradiation C: Temperature profiles at y-values from -40 to 70 pixels for determination of outlet.

Consider the control volume shown in Fig.7.1A. We denote the volumetric flow rate as $\dot{V}$, and the temperature difference between the inlet and outlet as ΔT. At steady state, the laser power converted into heat q can be estimated using Equation 1:

$$q = \dot{V}\rho C_p \Delta T \tag{7.1}$$

where ρ indicates water density and C_p indicates water specific heat. $\dot{V}$ was controlled by the syringe pump, and ρ and C_p are both known constants. We need to measure ΔT to estimate q and rely on IR thermography to determine the former quantity.

Fig. 7.1B shows a temperature field measured by the IR camera (x and y axis units in pixels). We use $y = 0$ to indicate the plane exposed to the laser. Steady-state temperature distributions at several y locations on the capillary surface are shown in Fig. 7.1C. Positive y values indicate capillary positions downstream of the laser spot whereas negative y values indicate upstream positions of the laser spot. To determine ΔT, we first determine the inlet and outlet boundaries of the control volume (shown in Figure 7.1A), and corresponding temperatures at these boundaries. Based on Fig. 7.1C, either y = -40 or y = -30 can be used as the boundary for the flow inlet, because the temperatures at these y locations do not vary significantly along the x direction. Similarly, y = 50, 60, or 70 can be used as the boundary for the flow outlet. The stable temperature profiles at different y locations indicate steady-state flow and also supports the assumption of neglecting heat loss because temperature decreases little in the y direction within the capillary region.

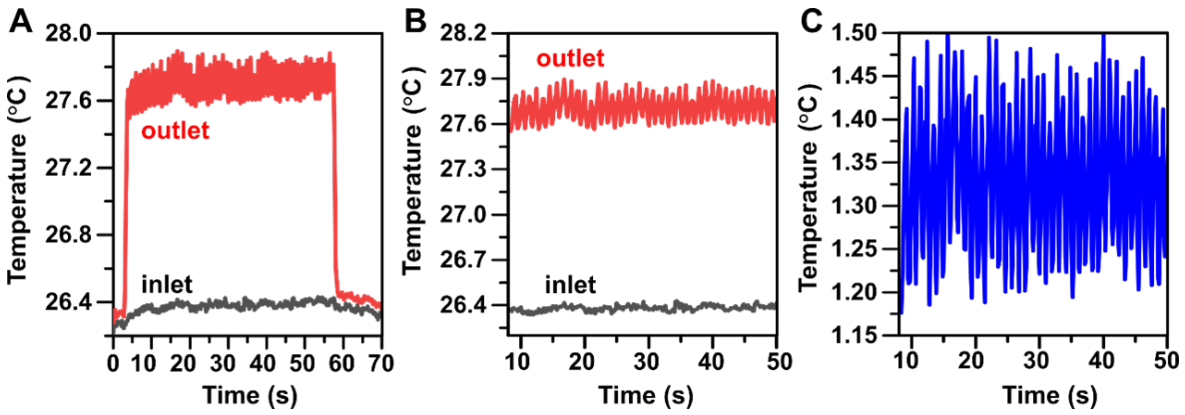

Figure 7.2: A: Mean temperature at the inlet and outlet. B: Isolation of steady-state temperatures. C: Temperature difference of inlet and outlet.

We use the mean value along x-axis of the capillary to indicate the temperature at y = -30 and y = 50 respectively (Fig. 7.2A). We extract the temperatures at steady state as shown in Fig.7.2B, and the temperature difference between inlet and outlet is shown in Fig. 7.2C. ΔT is calculated using the mean value of the temperature differences. Using the foregoing analysis procedure, the laser power converted to heat under different water flow rate and laser intensity setting is shown in Fig.7.3.

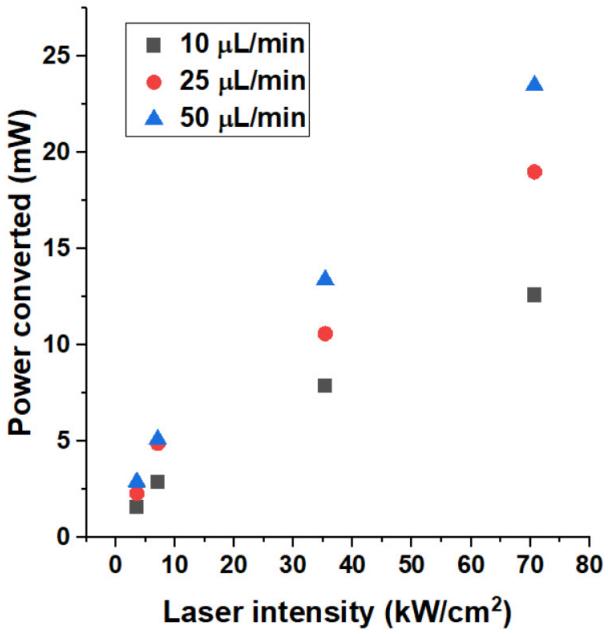

Figure 7.3: Average power converted to heat at different laser power densities (maximum laser power is 25 mW)

7.2 Transient plane source method for aerogel thermal diffusivity characterization

The thermal diffusivity of insulating materials is often measured by one or more of several methods, including transient plane source [56], laser flash [95] or 3-omega [36]. In this work, the sample is highly porous hBNAGs with a roughly cuboidal overall shape. For the transient plane source (TPS) method, the sensor is typically sandwiched by two identical samples. Considering the weight and shape of the sample here, robust symmetric contact with the sensor would be difficult to achieve in practice. As for the laser flash and 3-omega methods, they typically perform well for thin samples (thicknesses $< 100\mu$m) and are therefore not suitable for the present sample.

In this work, a variant of the TPS method is used in which the sample is suddenly but gently lowered onto a copper surface with constant temperature. The sudden contact with the copper surface simulates the process of applying constant temperature to the bottom the

sample. Upon contacting the copper surface, heat flows vertically from the copper plate to the sample; therefore heat conduction is reasonably approximated as 1D. Moreover, considering a very short time period in which thermal penetration depth is much less than the dimension of the sample, the sample size can be treated as infinite. Therefore in this work, semi-infinite 1D transient conduction theory is applied [24] to determine thermal diffusivity α.

7.2.1 Theory

For transient conduction into a semi-infinite plane with a constant surface temperature and a uniform-temperature initial condition, the temperature at distance x from the surface and time t is given by [24]:

$$\frac{T\left(x,t\right)-T_s}{T_i-T_s}=\mathrm{erf}\frac{x}{2\sqrt{\alpha\ t}} \tag{7.2}$$

where T_i is the initial temperature of the sample, T_s is the temperature of the hot copper surface, α is the thermal diffusivity, t is time, and x is the distance from the hot copper surface. In practice, a plane wall of a thickness $2L$ can be accurately approximated as a semi-infinite solid if[24]:

$$Fo=\alpha \mathrm{t}/L^2\leq 0.2 \tag{7.3}$$

Because the length of the sample is finite, to satisfy the semi-infinite assumption the model is valid up to $t<tmax=2$ s; this assumption is checked for validity according to the calculated α value.

7.2.2 Experimental setup

A large square copper plate was heated by a hot plate, and a copper bar was attached to the square copper plate with thermal paste. The remainder of the square copper plate was covered with styrofoam to impede heat flow to the surrounding air underneath the sample. The top surface of the copper bar was the source of constant temperature T_s in Eq. 7.2, and its temperature was recorded by a thermocouple reader (Omega™CL3515R). The ambient air temperature around the sample was measured by a thermocouple reader (Omega™CL3515R).

The sample was left in the air for at least 2 mins to reach the temperature of ambient air, which serves as T_i in Eq. 7.3. In this work, constant temperature was applied to the bottom of the sample by quickly lowering it to a hot copper surface. Because the sample was very light, it did not fall by its own weight; therefore, a holder was designed to guide the sample to drop to the hot copper surface. The sample holder was made of styrofoam with similar thermal properties as the hBNAGs to minimize heat transfer between the sample and the sample holder. The sample holder was inserted into a vertical guiding slot to fall (Fig. 7.4a and b). The sample holder was designed such that the bottom surface of the sample remained parallel to the copper surface during the descent to achieve good face-to-face contact (Fig. 7.4b), at $t = 0$ in Eq. 7.3. Because the thermal mass of the copper bar was much greater than that of the sample, changes in the copper temperature as measured by the thermistor were imperceptible. The average of the thermistor reading during the experiment was used as T_s in Eq. 7.3.

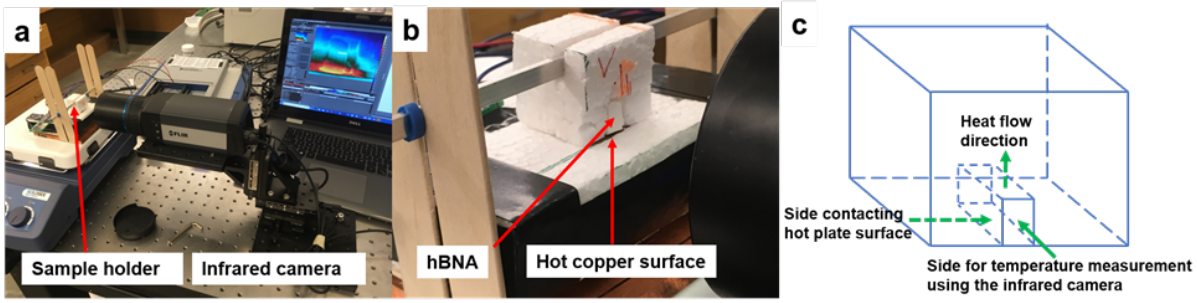

Figure 7.4: Experimental setup for the semi-infinite plane transient heat conduction. (a) The hBNAG is fixed in the middle of the sample holder, and the sample is lowered gently to the copper surface via a slot. The sample's vertical temperature profile was recorded using an infrared camera mounted on a X-Y-Z linear stage to guarantee perpendicularity. (b) hBNAG sample within the sample holder. (c) Illustration of different sides of sample when it touches the copper surface, faces the infrared camera, as well as the direction of heat flow.

Prior to the experiment, the radiative emissivity of the sample was calibrated by heating it to a known temperature measured by the thermistor. Because the heat conduction process was 1D (see Fig. 7.4c) in the x direction, temperature was assumed to be identical in the

plane perpendicular to x direction. Therefore, temperature on the side of the sample was treated as the sample temperature at different x and was detected using an infrared camera (Flir A655sc) with a closeup lens (25 μm resolution) as shown in Fig. 7.4. In the thermal image, different lines on the sample's side surface indicate different distances from the hot copper surface, and the average temperature of all pixels along each line was treated as the temperature at location x.

7.2.3 Uncertainty quantification

Given the temperature measurement results and corresponding mathematical model (Eq. 7.2), a commonly used approach to determine thermal diffusivity α is non-linear regression, such as Levenberg-Marquardt method. Such an approach gives a best estimate of α but is unable to estimate the probability distribution for α and does not consider uncertainties in other parameters (such as T_i, T_s, x). Bayesian inference incorporates prior distributions and likelihoods to give a complete statistical description of the unknown parameters (61) based on Bayes' formula:

$$p\left(\theta|Y\right) = \frac{p\left(Y|\theta\right)p(\theta)}{p(Y)} \tag{7.4}$$

where θ is the unknown random variable and Y is the observed data. The marginal probability distribution function $p(\theta)$ is the prior, which reflects prior knowledge of the parameter before experiment. The likelihood function is $p\left(Y|\theta\right)$, and the posterior probability density function (PPDF) of θ after observing measurement data Y is $p\left(\theta|Y\right)$. θ is typically estimated using an estimator such as the posterior mean, and the uncertainty of θ is determined by sampling the PPDF $p\left(\theta|Y\right)$.

In this work, according to Eq. 7.2, $\theta = \{\alpha, T_i, T_s,\ x\}$. The first step is to assign a prior distribution for all elements in θ. Before the experiment, prior knowledge was prescribed that the thermal conductivity of hBNAGs were comparable to air, and the order of magnitude of thermal diffusivity α was estimated using:

$$\alpha = k/(\rho \cdot C_p) \tag{7.5}$$

where k is thermal conductivity, ρ is mass density and C_p is the specific heat of hBNAGs. According to Eq. 7.4, α was estimated to be of the order of magnitude of $10^{-6}\mathrm{m}^2/\mathrm{s}$. A much wider uniform distribution ($10^{-8}\mathrm{m}^2/\mathrm{s}$, $10^{-4}\mathrm{m}^2/\mathrm{s}$) that covered 10^{-6} m2/s was used as the prior distribution for α. For T_i and T_s, because they were obtained using a thermocouple reader (Omega™CL3515R) that was accurate up to 0.5 K, the prior distribution for T_i and T_s were uniform distribution within (T_i-0.5 K, T_i +0.5 K) and (T_s-0.5 K, T_s +0.5 K) respectively. Temperature was measured at six evenly spaced locations (x) on the sample, indicated by six evenly spaced lines in Fig. 7.5. The location for line i is:

$$x_i = \text{offset} + i \times 5\text{pixels} \tag{7.6}$$

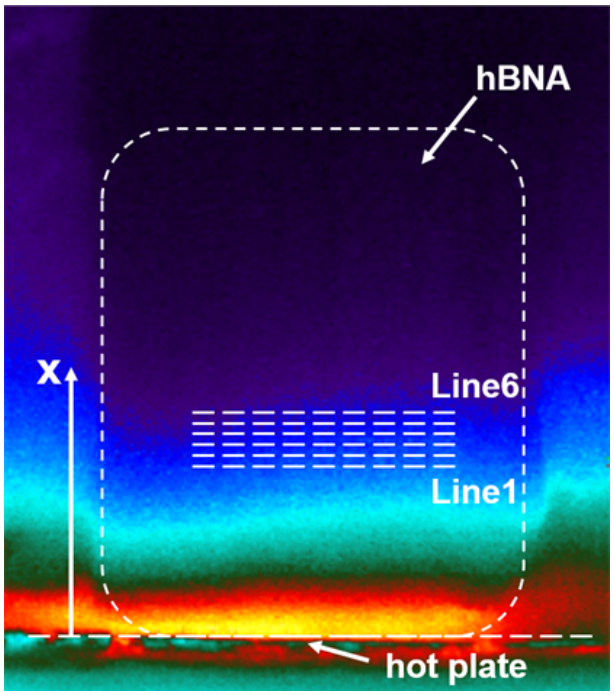

Figure 7.5: Thermal measurement of the hBNAG sample by IR imaging. Six evenly spaced lines indicate locations where temperature is measured. The average temperature of an individual line is obtained by averaging the temperature at all pixels along that line.

where $offset$ is the distance between the hot plate surface and the nearest line (line 0); five pixels represents the space between neighboring locations; and i=$\{0, 1, 2, 3, 4, 5\}$ indicates

the index of a given line. Because the boundary of the hot plate was not perfectly clear, an uncertainty of 3 pixels was assigned to offset. The software of the IR camera can accurately obtain temperature along evenly spaced lines; therefore, no uncertainty was assigned to the space between neighboring lines. According to Eq. 7.6, the prior distribution of the location of line i is a uniform distribution within ($offset$ + 5 pixels $\times$ i-3 pixels , $offset$ + 5 pixels $\times i$+3 pixels).

The second step is to build the likelihood $p\left(Y|\theta\right)$. In this work, the measured temperature was assumed to be Gaussian with mean $T\left(\theta\right)$ and standard deviation v_T. Therefore, $p\left(Y|\theta\right)$ is defined as:

$$p(Y \mid \theta) \propto \exp\left\{-\frac{\left((Y-T(\theta))^T(Y-T(\theta))\right)}{2v_T}\right\} \tag{7.7}$$

The third step involves combining the prior and likelihood using Eq. 7.6 to obtain the PPDF for thermal diffusivity. In this work, the PYMC3 python module [103] was used for the posterior mean estimation and sampling PPDF. For each measurement, α was estimated using the posterior mean according to the temperature profile at all six locations (x_i) on the sample, and the PPDF of α was obtained from numerical sampling. The temperature measurement result, posterior mean and PPDF of α for one measurement is shown in Fig. 7.6. For each hBNAG sample, the temperature measurement was repeated five times. Each measurement gives a posterior mean as well as a PPDF for α. Five PPDFs were combined to derive the mean thermal diffusivity using:

$$\bar{\alpha} \;=\; \frac{1}{5}\sum_{i=1}^{5}\alpha_i \tag{7.8}$$

where $\bar{\alpha}$ is the mean thermal diffusivity, and α_i indicates a random sample drawn from i^{th} PPDF.

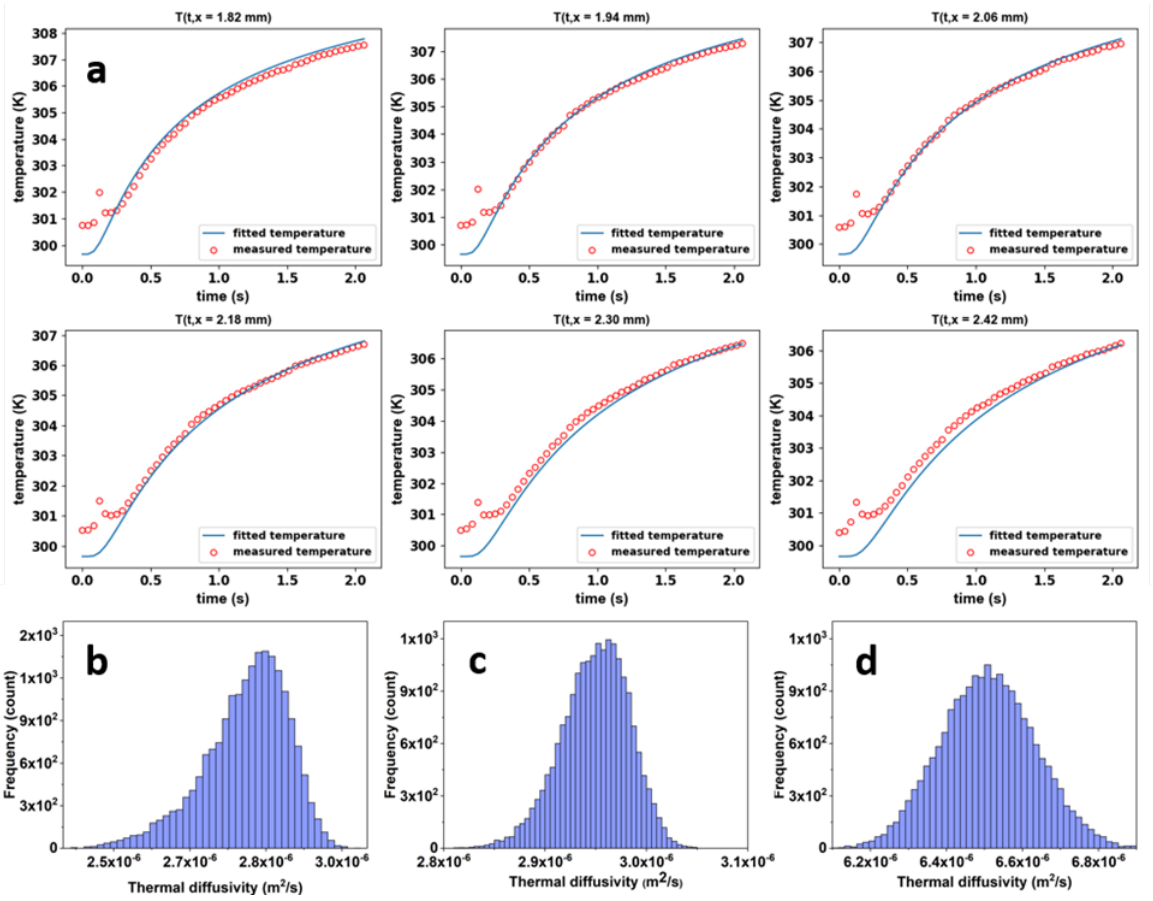

Figure 7.6: Fitting for thermal diffusivity at 6 different locations of one measurement. (a) Measured temperature at six evenly spaced locations on 10.1 mg/cm^3 hBNAG (red open circles) and temperature calculated using Eq. 7.2 and posterior mean estimation of thermal diffusivity (solid blue line). (b) Posterior probability density function of thermal diffusivity for one measurement. (c-d) Posterior probability density function of mean thermal diffusivity $\bar{\alpha}$ (combines PPDFs of 5 measurements) for hBNAGs of 10.1 mg/cm^3 and 5.2 mg/cm^3.

In this work, thermal diffusivity of hBNAGs of different densities were measured. For example, using the foregoing Bayesian inference approach, mean thermal diffusivities for 5.2 mg/cm^3 sample were 6.5×10^{-6}m^2/s, and the probability distribution of corresponding mean thermal diffusivity is shown in Fig. 7.6. According to the probability distribution, the 95% confidence interval for mean thermal diffusivities for 5.2 mg/cm^3 samples were (6.27×10^{-6}m^2/s to 6.75×10^{-6}m^2/s). Because the experiment was performed at 40.1°C

according to Fig. 7.6, the specific heat of hBNAG is 630 J/(kg K). Using Eq. 7.5, thermal conductivities for the hBNAG of 5.2 mg/cm^3 are 21.3 ± 0.8 mW/m K.

7.3 PDMS thermal diffusivity characterization

We employ the custom thermal diffusivity instrument present in section 2.4 to characterize nanowire impregnated Poly-dimethyl Siloxane (PDMS). The advantage of this method is that it does not require the knowledge of exact heat input to the sample and is insensitive to heat loss to the surrounding. This method assumes heat is conducted in-plane in one dimension. For a stripe sample, this method requires imposition of periodic temperature oscillations at one end, and measures the amplitude decay and phase shift of the oscillatory temperature profiles at different locations along the sample. The experimental setup is shown in Fig. 7.7(A). Here we applied periodic voltage signals to a Peltier device, two aluminum angle brackets were used to conduct heat from the Peltier device to the PDMS sample. Temperature was measured using a FLIR A655sc high resolution infrared camera and the temperature profiles along the direction of heat conduction is shown in Fig. 7.7(B). For two isothermal lines in the heat conduction path, the oscillatory temperature profiles are shown in Fig. 7.7(C).

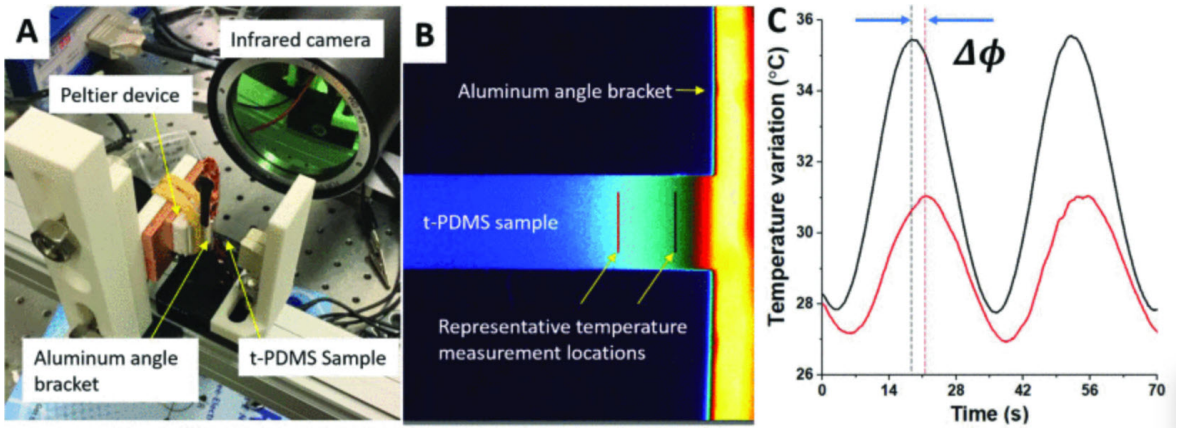

Figure 7.7: (A) Experimental setup of thermal diffusivity measurements. (B) Representative infrared image capture from the diffusivity experiment. (C) Representative plot of measured data depicting phase delay of thermal wave.

The thermal diffusivity of the material can be determined based on amplitude decay and phase shift from multiple locations along the heat conduction path on the sample. Results of the thermal diffusivity experiment are provided in Fig. 7.8(A), with 95% confidence interval error bars included.

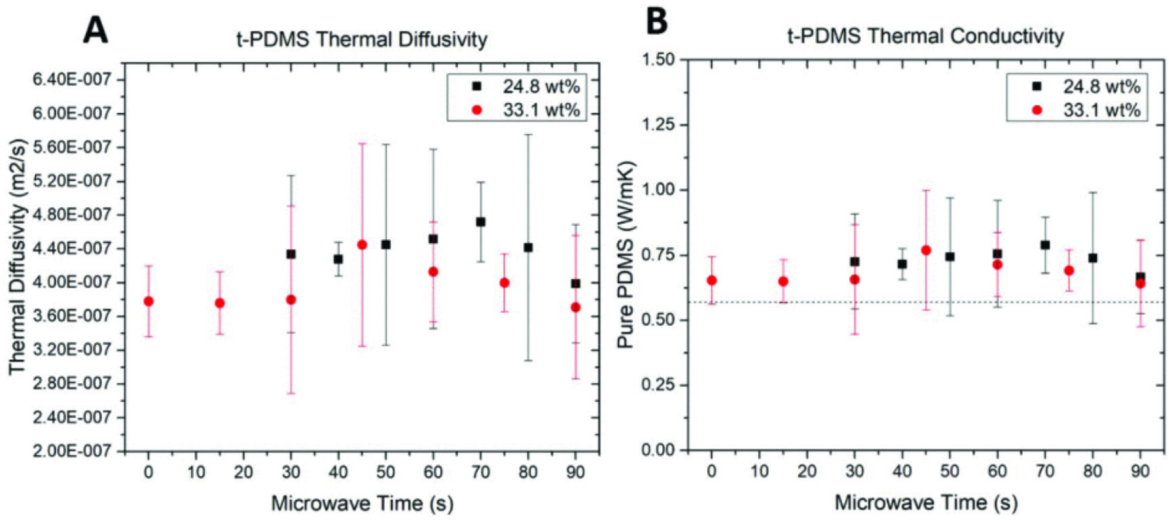

Figure 7.8: (A) Measured thermal diffusivities of t-PDMS samples at 24.8 wt% and 33.1 wt%. (B) Computed thermal conductivities of t-PDMS samples. The dashed line depicts the measured thermal conductivity of pure PDMS.

The density of the pure PDMS sample was provided in the datasheet as 1106.7 kg/m^3, while the densities of the t-PDMS samples was calculated using the rule of mixtures and assuming the density of the copper nanowires is equivalent to the density of bulk copper. The computed thermal conductivities of the t-PDMS samples are shown in Fig. 7.8(B) as functions of microwave time, as well as the thermal conductivity of pure PDMS, depicted as a dashed line, measured in the same set of experiments. The data shows that the improvement in thermal conductivity is minimal at both fill fractions, with a peak enhancement of 38.7% for the 24.8 wt% t -PDMS at a microwave time of t = 70s.

CHAPTER 8

Closure

In this study, we develop new spectroscopy techniques for rapid and accurate characterization for thermal and electrochemical systems. In addition, we employ data science methods for rigorous uncertainty quantification. Next, we summarize the main highlights and findings for each research topic, as well as potential future works.

8.1 Room temperature thermal diffusivity characterization

For the room temperature thermal diffusivity characterization, we use forced convection such that the averaged convective heat transfer coefficient along the heat conduction is uniform and constant. This enables thermal diffusivity characterization outside vacuum for high sample testing throughput. Secondly, we use IR thermography to precisely measure amplitude decay and phase shift, and simultaneously characterize multiple regions on a sample. Thirdly, we use an analytical solution developed by Lopze et al.[77] to eliminate the semi-infinite medium assumption and enables characterization of relatively short samples. Lastly, we develop a Bayesian framework for uncertainty quantification instead of using classical regression approaches.

The limitations of our approach are: (1) samples must be thermally conducting, such that forced convection does not introduce 2D effect. (2) A thin layer of high emissivity coating material must be applied to facilitate IR thermography. The coating must be thin and uniform. In addition, for thin film samples, the contribution of such coating materials may not be neglected. We must either include their contribution in the model or use different temperature detection methods [60].

For potential future works, firstly we can use similar technique to characterize materials with non-uniform thermal diffusivities. We've publish a python module to simplify this process. Secondly, similar technique can be used to characterize thermal contact resistance, and our preliminary findings indicate amplitude decay exhibit relatively high sensitivity in thermal contact resistance. Thirdly, we can estimate the averaged convective heat transfer coefficient from the physical model. Our result shows that without any optimization, the averaged convective heat transfer coefficient estimated from amplitude and phase measurements matches reasonably well compared to that obtained using the external flow correlation over an isothermal plate. With certain optimization, convective heat transfer coefficient can be determined much more precisely, and this can be further used to estimate fluid velocity.

8.2 High temperature thermal diffusivity characterization

For the high temperature study, we directly heat samples using a concentrated light source which enables the samples to reach stable high temperatures rapidly (in 10 min) compared to conventional surrounding heating approaches (several hours). Secondly, we use IR thermography for non-contact, non-destructive and data-rich temperature detection. We further demonstrate that amplitude decay and phase shift can be measured accurately, even if emissivity is not known precisely. Thirdly, we use surrogate-accelerated Bayesian framework and a No-U-Turn sampler for rigorous uncertainty quantification, compared to regression approaches in previous studies for solving inverse heat transfer problems.

The main limitation of this study is that significant temperature gradients exist along the heat conduction direction. This is inconvenient because (1) The light source must be characterized accurately because temperature-dependent properties are required for modeling, and thus energy input to the system must be characterized. For most Angstrom's methods quantifying energy input to the system is not required. (2) An analytical solution does not exist because radiation losses cannot be linearized. In our study we use surrogate models to accelerate the physical model. However, surrogate modeling suffers the curse of dimensionality and does not work if huge amount of unknowns exist. (3) Significant thermal stress are

observed during the transient heating process. This can be a severe issue for materials with high thermal expansion coefficient and low thermal conductivity, and may cause sample to bend and fail.

For future works, firstly we need to quantify model form error for the finite difference model and also include the error in the surrogate model for the Bayesian analysis. Secondly, the system can be modified to characterize characterize more complex samples. Cowan's method [42] can be employed to characterize smaller samples using peak solar intensity to achieve higher temperatures. Thirdly, the system can be used to characterize other properties. For instance, we obtained relatively consistent intensity distribution parameter with different graphite samples and heating frequencies. However, we also observe that the life span of the light bulb decrease dramatically with oscillating current, which is also not recommended in the manual of the plasma light bulb. Therefore, modulating the intensity of the light source may not be the best approach, and use periodic shutter for the light source may be more practically preferable.

8.3 Electrochemical impedance spectroscopy

In this work, we use exponential chirp signals as broadband perturbations to accelerate impedance measurements. We develop an adaptive procedure to apply different shunt resistors and chirp signals for different frequency bands, such that EIS can be characterized precisely over the entire frequency range. The custom instrument is accurate and is nearly four times faster compared to commercial instruments that use the single frequency scan approach.

The limitations of this study are (1) NI data acquisition systems are used for signal generation and data acquisition. This can be replaced with custom circuitry to significantly reduce cost. (2) Characterizing EIS beyond 10 kHz using the exponential chirp signal is inefficient and the result tends to be noisy. The instrument can be designed into hybrid mode, in which exponential chirp signals are used to characterize EIS up to 10 kHz frequency

range, and use single frequency scan for higher frequencies.

The possible future works include (1) custom data acquisition system to replace and NI hardware. (2) interpret EIS results using data science methods. For instance, use EIS to derive equivalent circuits for electrochemical devices, or use EIS to understand state of health and state of charege of electrochemical devices. Currently, data science techniques are being widely used for such interpretations. With rapid EIS characterization speed and in-depth analysis using data science, I believe more insights can be obtained for electrochemical devices.

APPENDIX A

Appendix for room temperature Ångström's method study

A.1 Temperature variation along y-axis

The convective heat transfer coefficient h is non-uniform along the y-axis, as discussed in section 4. Here we examine the effect of non-uniformity in h by showing the mean temperatures along four horizontal lines in Fig. A.1A. Air was supplied below the sample and the velocity was approximately 3.3 m/s. For four different y locations on the sample, the mean temperatures did not exhibit significant difference as shown in Fig. A.1B, possibly because of good heat spreading properties of the sample under test. Therefore, variation of h along the y-axis is insignificant in this work.

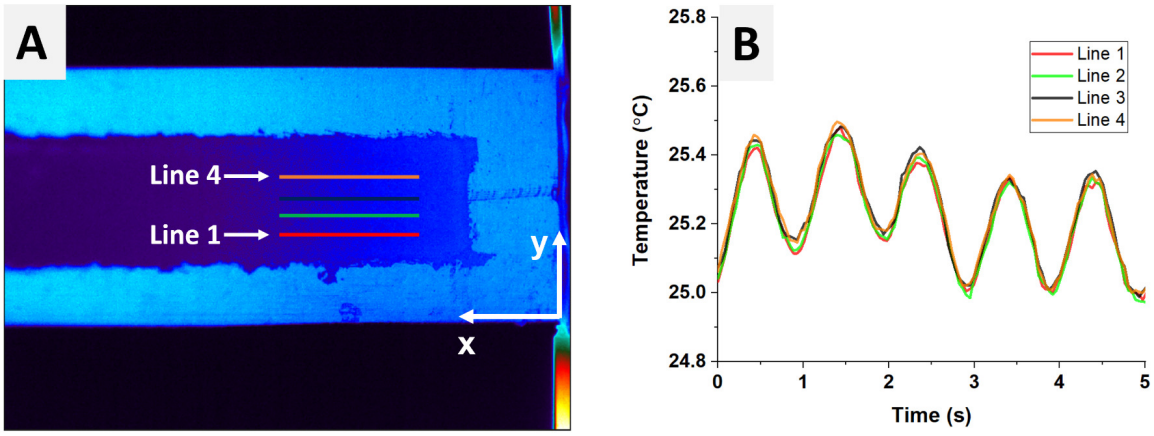

Figure A.1: (A) Four evenly spaced horizontal lines in an IR image. (B) Average temperatures on the four lines shown in Fig. A.1A.

A.2 Amplitude ratio and phase difference calculation in the region of interest

For N evenly spaced isotherms shown in Fig. A.2A, we obtained phases and amplitudes at these locations by fitting the temperature profiles to a sinusoidal function. Next we normalized the amplitudes for these isotherms using the amplitude at Line 1 to obtain the amplitude ratios. Similarly, we subtracted the phases using the phase at line 1 to calculate the phase differences. The amplitude ratios and phase differences for these isotherms are shown in Fig. A.2B.

To fully utilize temperature measurements in the region of analysis, the evenly spaced isotherms in Fig. A.2A were shifted to the left by one pixel to obtain another N isotherms as shown in Fig. A.2C. Then we extract the amplitude ratios and the phase differences for these isotherms. The foregoing process was repeated several times to obtain amplitude ratios and phase differences in the entire region of analysis, as shown in Fig. A.2D.

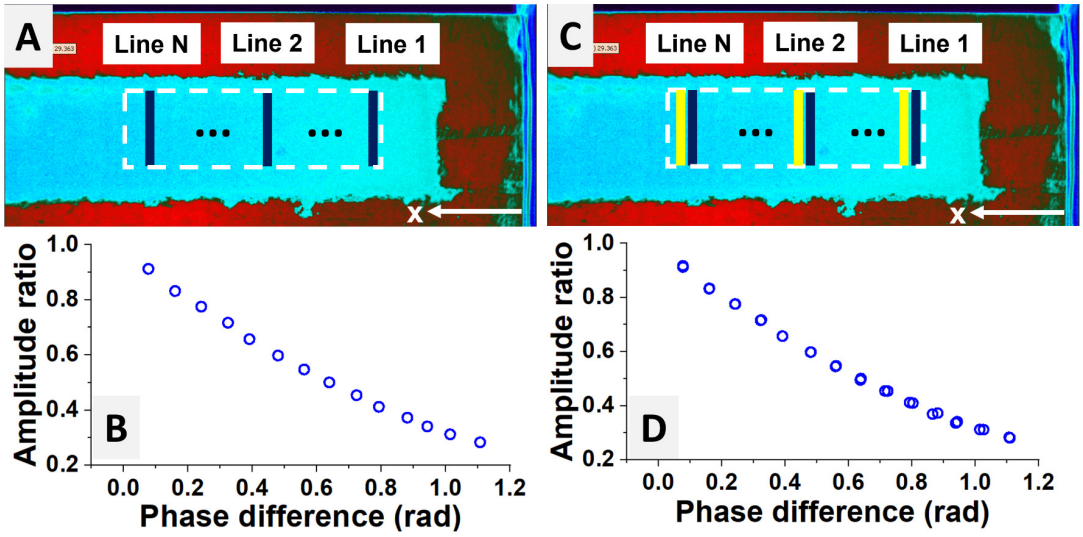

Figure A.2: (A) Infrared (IR) imaging and the region of interest (dashed white rectangle) for N equally spaced isotherms. (B) Phase differences and amplitude ratios for the isotherms in (A). (C) Another N isothermal lines (yellow lines) by shifting the isothermal lines in (A) to the left by one pixel. (D) Phase differences and amplitude ratios for the entire region of analysis.

A.3 Trace plots of the Metropolis algorithm

Here we examine the random samples obtained from our Metropolis algorithm. The trace plot for the first parameter α is shown in Fig. A.3A, and good mixing is observed. The autocorrelation between samples is low, as indicated in Fig. A.3B. Then we examine the trace plot for the second parameter h. Similarly good mixing is observed as shown in Fig. A.3C, and the autocorrelation between samples is low, as indicated in Fig. A.3D. Furthermore, good mixing and relative low autocorrelation between samples are observed for parameter $\sigma_{\Delta A}$ and $\sigma_{\Delta\phi}$. Lastly we examine the fifth parameter ρ. Relatively strong autocorrelation is observed (0.4 for lags = 40). Based on the trace plot, mixing is not as good as the other parameters but still shows reasonable coverage of the space.

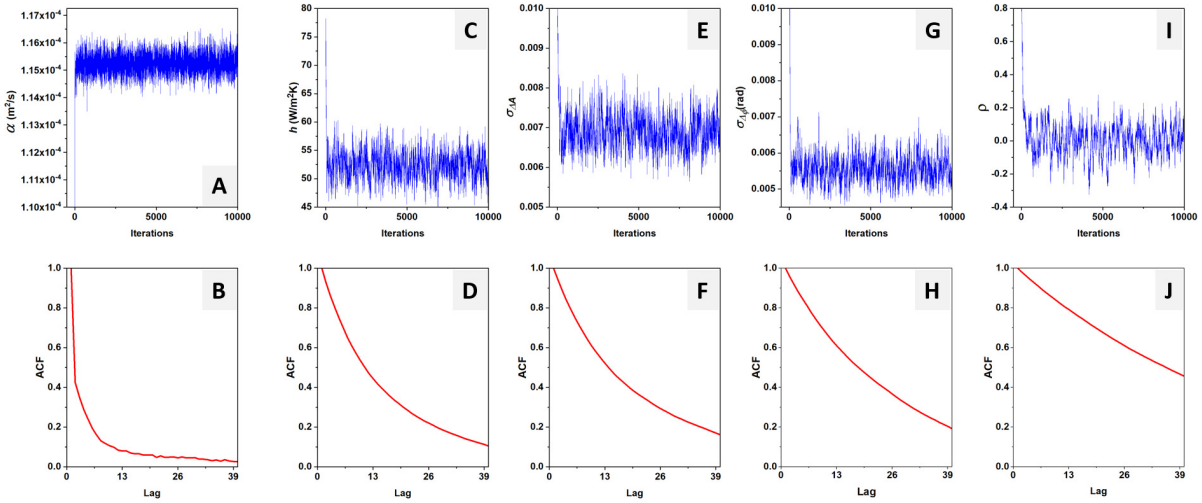

Figure A.3: (A) Trace plot for α. (B) Autocorrelation function (ACF) for trace α. (C) Trace plot for h. (D) ACF for trace h. (E) Trace plot for $\sigma_{\Delta A}$. (F) ACF for $\sigma_{\Delta A}$. (G) Trace plot for $\sigma_{\Delta P}$. (H) ACF for $\sigma_{\Delta P}$. (I) Trace plot for ρ. (J) ACF for ρ.

To further examine the trace, we provide a pairwise scatter plot for all parameters. Because of large amount of data, only 1 out of 10 sample is shown here. The plots on the diagonal indicate probability distribution for each parameter. The contour plots below the diagonal indicate joint distribution and the scatter plots above the diagonal show the 2D scatter plots between two parameters. No strong correlation between parameters are observed according to the pairwise scatter plots, which indicate good identifiability for model parameters.

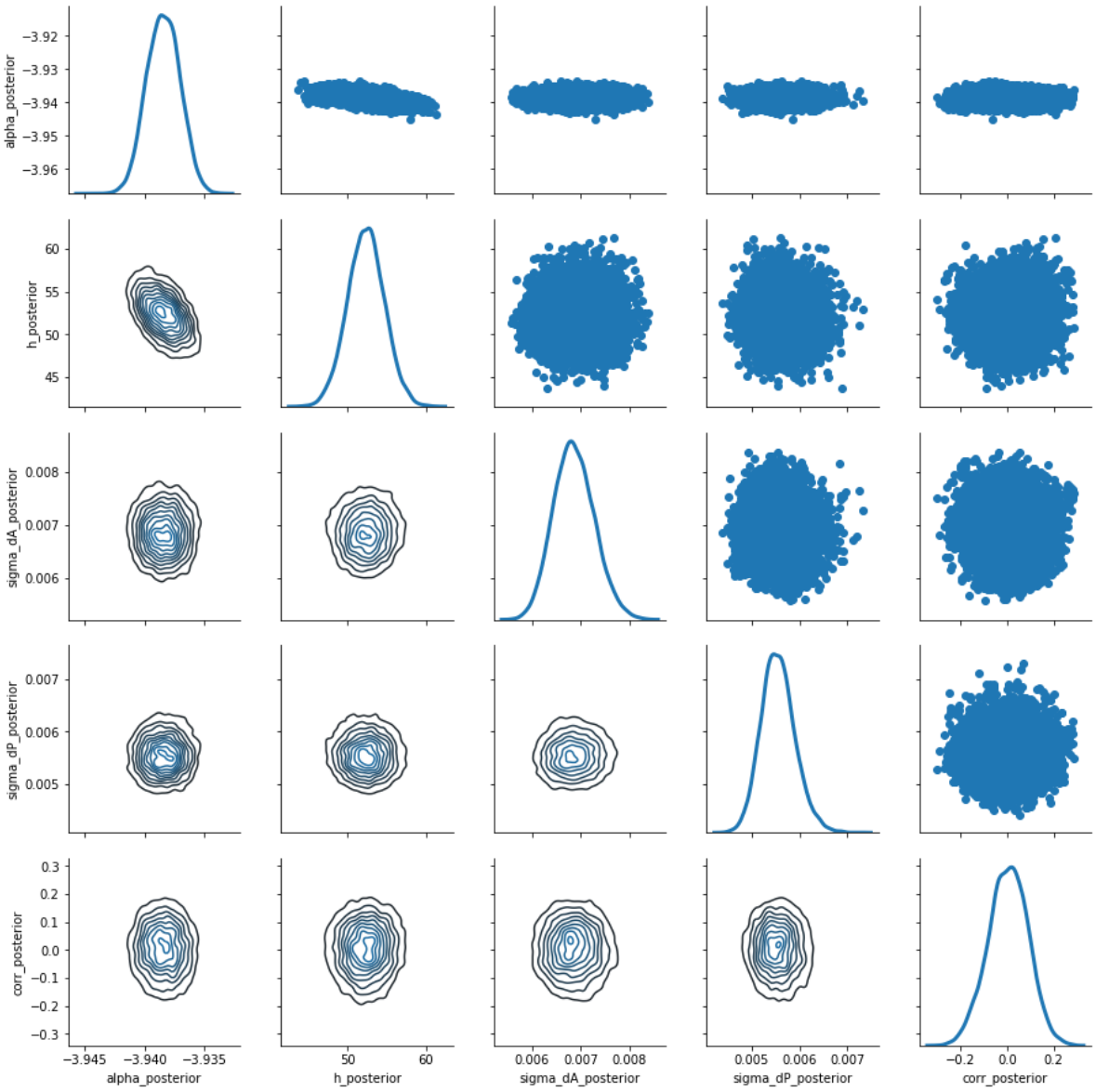

Figure A.4: Pairwise scatter plot for posteriors

A.4 Use of a Fisher transformation for parameter ρ

The initial proposal distribution used for parameter ρ was a uniform distribution defined in Eq. A.1. However, the posterior showed poor mixing and strong autocorrelation, as shown in Fig. A.5.

$$\rho^{'} = \mathrm{U}[\max(-1, \rho - 0.01), \min(1, \rho + 0.01)] \tag{A.1}$$

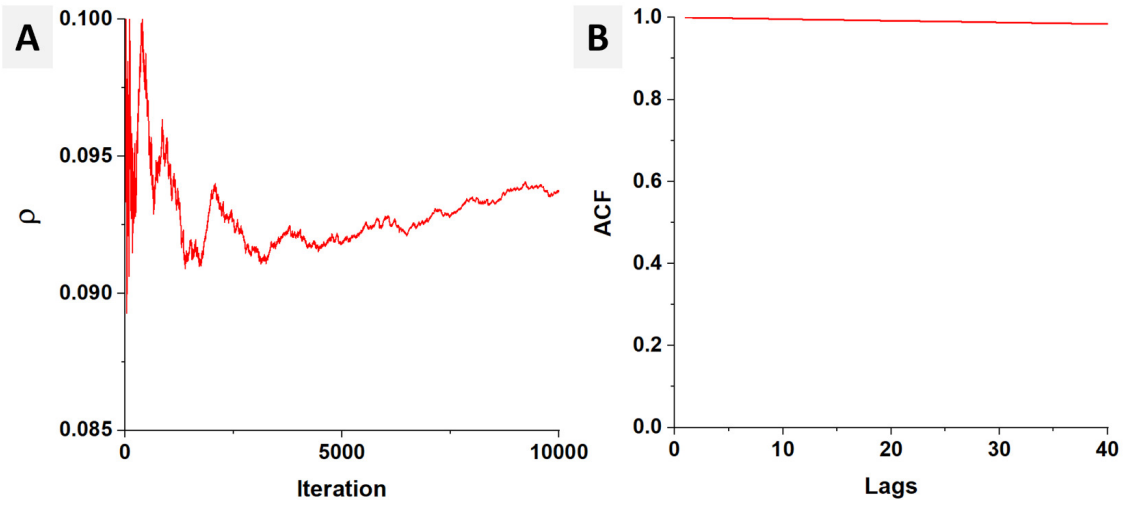

Figure A.5: (A) Trace plot for ρ using uniform proposal. (B) ACF for ρ using uniform proposal. The autocorrelation between samples is very strong, indicating poor mixing.

To mitigate this issue, we applied a Fisher transformation to convert ρ into an unbounded variable z, and used a normal random walk to propose z. To account for the reparametrization, a Jacobian was added to the posterior. The results for the transformed variable are shown in Fig. A.3I and J, and much better mixing and much lower autocorrelation are obtained using transformed variable.

APPENDIX B

Appendix for electrochemical impedance spectroscopy characterization using exponential chirp signals

B.1 Computed EIS from chirp signals

In this work an exponential chirp signal is employed. It scans each frequency decade at the same rate and is particular efficient for low frequency EIS measurements. The expression for a generic exponential chirp voltage signal as a function of time t is given in Eq. B.1,

$$v(t) = A\sin\left\{\phi_0 + 2\pi f_0\left(\frac{k^t - 1}{\ln k}\right)\right\}, k = \left(\frac{f_1}{f_0}\right)^{1/T} \tag{B.1}$$

where A is the voltage amplitude, and is set as 25 mV in this work to promote system linearity [33]. ϕ_0 is the initial phase and is set as zero in this work. f_0 is the starting frequency, f_1 is the ending frequency, and T is the time required to scan from f_0 to f_1. In this work, each chirp signal starts at low frequency $f_{C,0} = 0.5 \times f_0$ and ends at high frequency $f_{C,1} = 1.2 \times f_1$. The sampling frequency f_S is selected to be 10 times of the highest frequency f_1, and the length of the chirp signal T is chosen as $3/(2f_0)$, so that the resolution in the frequency domain is approximately $2f_0/3$.

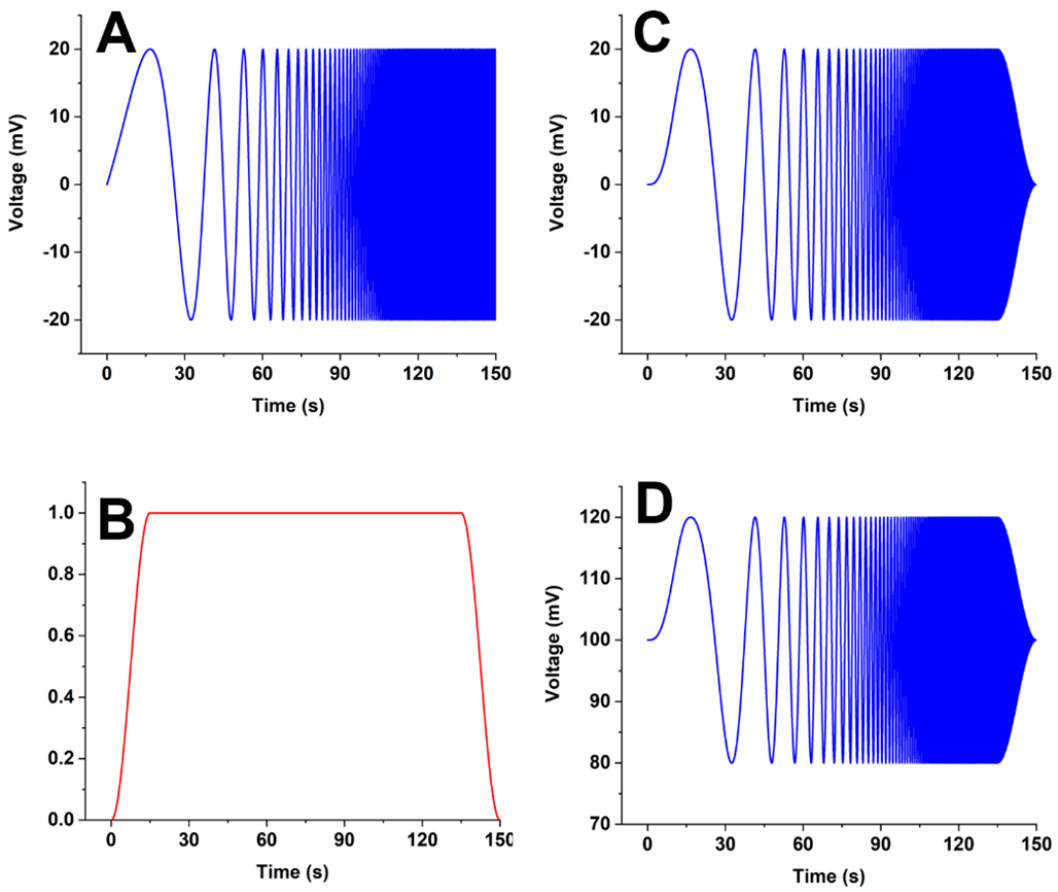

Figure B.1: (A)The original chirp signal. (B) A Tukey window function. (C) The windowed chirp signal. (D) The windowed chirp signal superimposed with bias DC voltage (100 mV).

Fig. B.1A shows a chirp signal with $f_0 = 10$ mHz, $f_1 = 10$ Hz and $T = 150$ s. To avoid sharp transition at $T = 0$ and $T = 150$ s, a Tukey window $\alpha = 0.03$ (Fig. B.1B) is employed to smooth the original signal, and the windowed chirp signal is shown in Fig. B.1C. In this work, α is chosen such that the chirp signal in the frequency band of interest ($[f_0, f_1]$) is not attenuated by the Tukey window. And lastly, a constant V_{DC} is added to the windowed signal to enable EIS characterization at bias voltage. The expression for the windowed exponential chirp signal used in this work is defined below, where win indicates a Tukey window function:

$$v(t) = V_{DC} + \text{win}\left[A\sin\left\{\phi_0 + 2\pi f_0\left(\frac{k^t - 1}{\ln k}\right)\right\}\right], k = \left(\frac{f_{C,1}}{f_{C,0}}\right)^{1/T} \tag{B.2}$$

The quantization error for the 16-bit DAQ board is 0.3 mV [10], which is approximately 1.2% of the perturbation amplitude (25 mV) and is therefore acceptable for EIS measurements.

The foregoing perturbation signal is generated and applied to the circuit in Fig. 5.4. The voltages across the shunt resistor (V_S) and the supercapacitor (V_C) are measured by two differential analog input channels, as shown in Fig.5.4. The current through the circuit (I_C) is calculated using the voltage across the shunt resistor:

$$i_s\left(t\right) = \ v_s(t)/R_S \tag{B.3}$$

The impedance of the supercapacitor is derived using a discrete Fourier transform (DFT), and because the DC bias voltage creates a constant current in the circuit (I_{DC}), these DC components must be subtracted before calculating impedance.

$$Z_C = \frac{DFT\left(v_C\left(n\Delta\right) - v_{DC}\left(n\Delta\right)\right)}{DFT(i_C\left(n\Delta\right) - i_{DC}\left(n\Delta\right))} \tag{B.4}$$

where $n\Delta$ indicates discrete sample.

An example is shown below for EIS calculation. Here we used a 998.5 Ω shunt resistance to measure EIS of a commercial supercapacitor (Manufacturer: Nichicon, capacitance 1 mF). The frequency range of EIS measurement is 10 mHz to 1 Hz and bias DC voltage V_{DC} is 2.0 V. For the chirp signal $v\left(t\right)$ applied to the circuit, $f_0 = 10$ mHz, $f_1 = 1$ Hz, the length of the chirp signal is $T = \ \frac{3}{2f_0} = 150$ s. Sampling frequency is $f_s = 10f_0 = 10$ Hz. The measured perturbation signal $v(n\Delta)$ is shown in Fig. B.2A. The measured voltage sample $v_C\left(n\Delta\right)$ and $v_S\left(n\Delta\right)$ are shown in Fig. B.2B and C respectively. Based on $v_S\left(n\Delta\right)$ and the shunt resistance $R_S = 998.5\Omega$, the current in the circuit $i(n\Delta)$ is determined and shown in Fig. B.2D. Given $v_C\left(n\Delta\right)$ and $i(n\Delta)$, EIS of the supercapacitor was computed using Eq. B.4, and impedance and phase component of the EIS results are shown in Figs. B.2E and F.

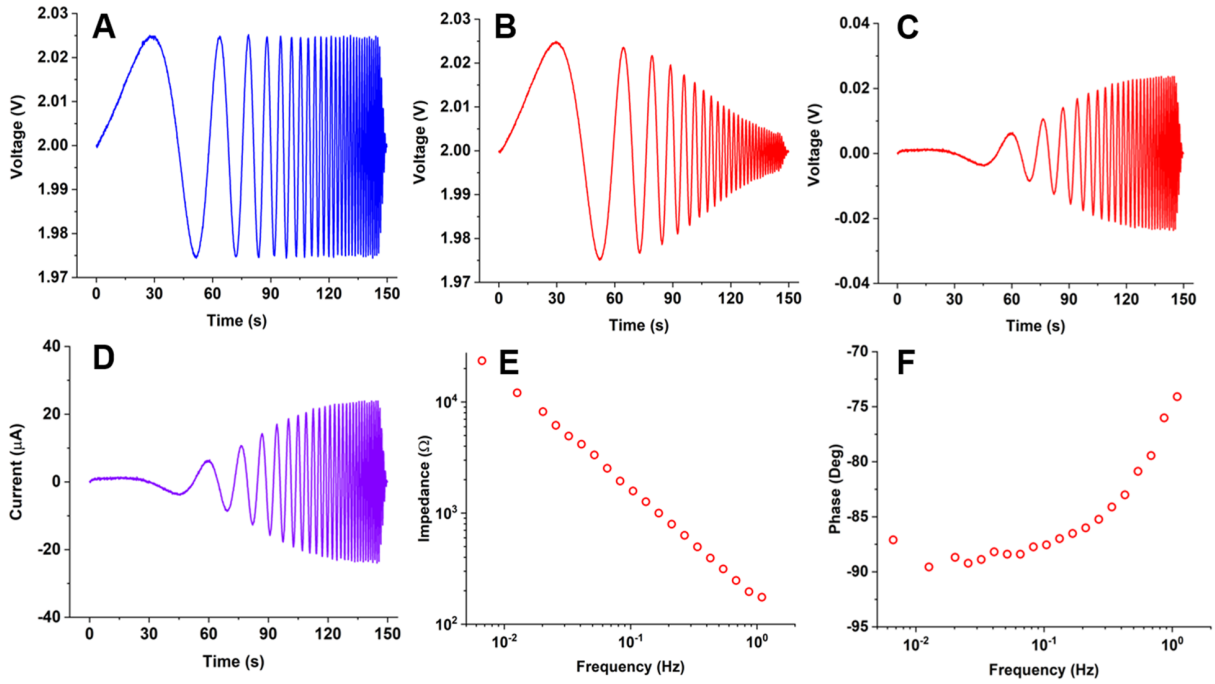

Figure B.2: Demonstration of EIS measurement and calculation using a commercial supercapacitor from 10 mHz to 1 Hz under 2 V bias voltage. (A) Perturbation voltage signal applied to the circuit $v\,(n\Delta)$. (B) Voltage across the supercapacitor $v_S\,(n\Delta)$. (C) Voltage across the shunt resistor $v_S\,(n\Delta)$. (D) Current in the circuit $i\,(n\Delta)$. (E) Bode plot for calculated impedance $|Z_C(f)|$. (F) Bode plot for calculated phase $\angle Z_C(f)$.

B.2 Instrument software

The EIS measurement system requires advanced software architecture for signal generation, circuit control, and data acquisition. In a previous study [111], Stevic and Andjelkovic and Antic employed a simple LabVIEW 'while' loop to accomplish signal generation and data acquisition. Such a software architecture cannot easily implement complicated measurement procedures as well as code upgrades. To improve versatility of the code, a classical state machine [31] was used to implement the adaptive EIS algorithm shown in Fig. B.3. In addition, an objected-oriented LabVIEW class is employed to enhance data encapsulation in the code to simplify data management. The flow diagram of the instrument is shown in

Fig. B.4.

Algorithm 1 Adaptive EIS

```
procedure ADAPTIVE EIS
    Z(f) ← EIS(f_0, f_1, V_DC, R_s)
loop:
    if max(Z)/R_s > x_b then
        if max(Z)/max(R_s) > x_s then
            if R_s = max(R_s) then
                if min(Z)/R_s > x_s then
                    check and save data, update f, R_s
                else
                    1. find f* s.t. Z(f*) ≥ R_s · x_s
                    2. save data between [f^0, f*], update f, R_s.
            if R_s ≠ max(R_s) then
                R_s ← max(R_s), repeat measurement
        if max(Z)/max(R_s) ≤ x_s then
            1. find all Rs s.t. x_s < max(Z)/R_s ≤ x_b
            2. use smallest R_s, repeat measurement
    if max(Z)/R_s < x_b then
        if max(Z)/min(R_s) ≤ x_b then
            if R_s = min(R_s) then
                check and save data, update f, R_s
            else
                R_s ← min(R_s), repeat measurement
        if max(Z)/min(R_s) > x_b then
            1. find all Rs s.t. x_s < max(Z)/R_s ≤ x_b
            2. use smallest R_s, repeat measurement
    if x_s ≤ max(Z)/R_s ≤ x_b then
        if min(Z)/R_s ≥ x_s then
            check and save data, update f, R_s
    else
        if R_s = min(R_s) then
            check and save data, update f, R_s
        else
            1. find f* s.t. Z(f*) ≥ R_s · x_s
            2. save data between [f^0, f*], update f, R_s.
    goto loop.
    close;
```

Figure B.3: Adaptive procedure for EIS measurements using variable shunt resistance.

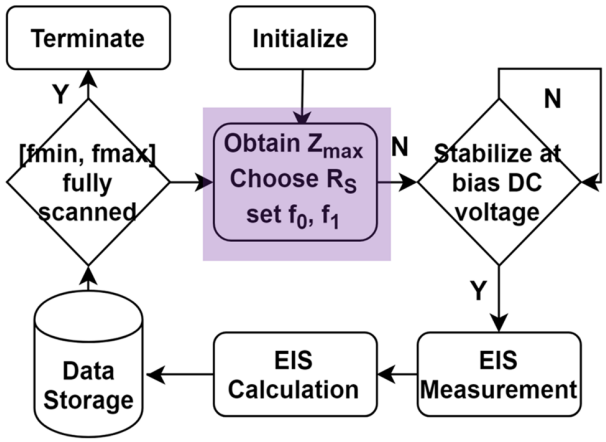

Figure B.4: Flow chart of the instrument. The shaded region indicates the adaptive algorithm shown in Fig. B.4.

The graphical user interface for the custom instrument is shown in Fig. B.5A. The software is user- friendly and requires only three inputs: the frequency band of EIS measurements, the bias DC voltage at which EIS is performed, and the estimated capacitance of the supercapacitor (need not be accurate). The LabVIEW program executes impedance measurements automatically, and real time impedance results can be visualized. The software also saves all relevant data, including important process parameters, signal waveforms, and EIS results to a local MySQL database. To visualize and compare historical measurements, a web-based user interface was developed as shown in Fig. B.5B.

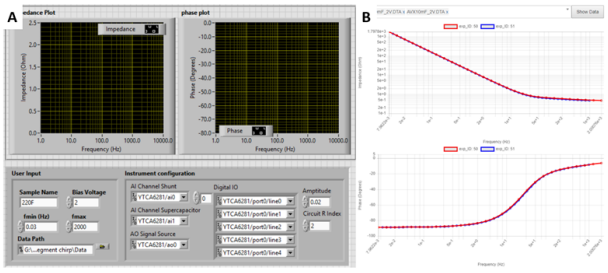

Figure B.5: (A) Instrument user interface. (B) A web-based interface for EIS data visualization and management.

B.3 Adaptive algorithm for EIS measurement

The algorithm for adaptive EIS measurement is shown as a pseudo-code in Fig. B.3. We provide an example to demonstrate this algorithm step by step to reproduce EIS results shown in Figs. B.6A and B.

Here, the frequency range of EIS is from 10 mHz to 2 kHz with 2 V constant DC bias voltage. According to the estimated capacitance of 1.1 mF, the estimated maximum impedance is about 14.4 k Ω according to Eq. 5.2. Therefore, according to Eq. 5.3, the fourth resistor in the resistor bank ($R_S = 998.5\Omega$) was connected to the circuit for EIS measurements from 10 mHz to 1 Hz. Then a chirp perturbation signal was applied ($f_{C,0} = 0.5 \times 10 = 5$ mHz, $f_{C,1} = 1.2 \times 1 = 1.2$ Hz, $T = 150$ s), and the resulting voltage across across the shunt resistor and the supercapacitor are shown in Fig. B.6A. The corresponding EIS results for this frequency band are shown in Fig. B.6B.

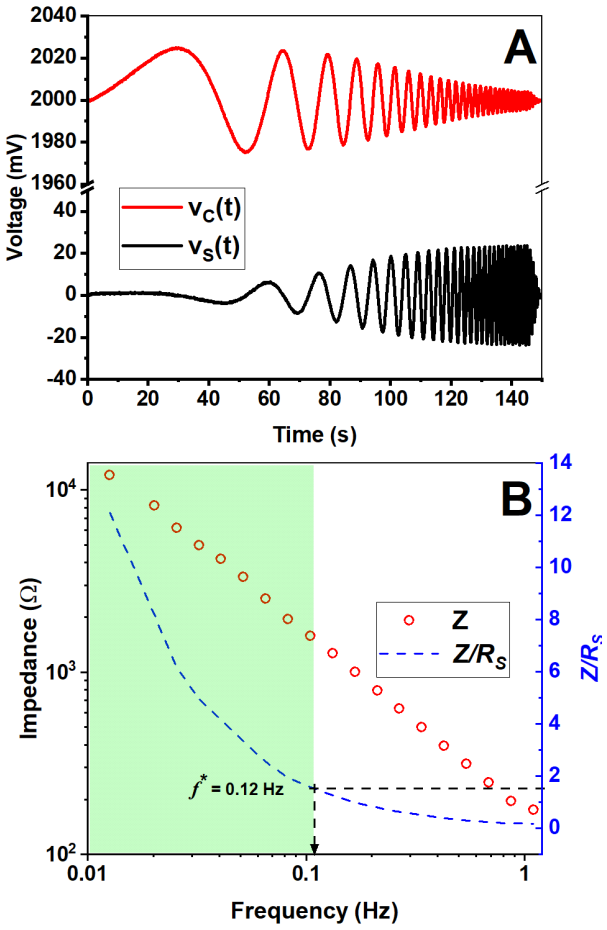

Figure B.6: (A) The voltage across the supercapacitor and the voltage across the shunt resistor ($R_S = 998.5\Omega$) when the chirp perturbation signal was applied ($f_{C,0} = 0.5 \times 10 = 5$ mHz, $f_{C,1} = 1.2 \times 1 = 1.2$ Hz, $T = 150$ s). (B) The Bode plot of impedance for the frequency band from 5 mHz to 1.2 Hz. The right axis indicates the ratio between the impedance of the supercapacitor Z and the shunt resistance R_S. The green shaded region indicates accurate EIS results.

First the algorithm computes EIS results within a given frequency subband (10 mHz - 1 Hz), and evaluates the ratio between Z_{max} (12062 Ω) and R_S. Because $1.5 < 12062/R_S < 15$, the shunt resistance is comparable to the maximum impedance of the supercapacitor. Therefore, Z_{max} measured with $R_S = 998.5\ \Omega$ is accurate. Next the algorithm checks if Eq. 5.4 is satisfied for the entire frequency subband (10 mHz - 1 Hz). The ratio between

impedance and shunt resistance is shown as a dashed blue curve in Fig. B.6B, and the highest frequency such that Eq. 5.3 holds is $f^* =$ 0.126 Hz. Therefore, impedance results from 0.01 Hz to 0.126 Hz were saved (shown as green shaded area). The measurement continued from 0.126 Hz. Based on the impedance at 0.126 Hz, the instrument automatically connected an appropriate shunt resistance ($R_S =$ 99.9Ω) to the circuit to account for decreased impedance with increased frequency. Next the instrument applied a different chirp excitation for the new frequency subband ($f_0 =$ 0.126 Hz, $f_1 =$ 12.6 Hz) using an appropriate chirp signal ($f_{C,0} = 0.5 \times 0.126 =$ 0.063 Hz, $f_{C,1} = 1.2 \times 12.6 =$ 15.1 Hz, $T =$ 15.88 s). The voltages across the supercapacitor and the shunt resistor are shown in Fig. B.7A, and corresponding EIS results are shown in Fig. B.7B.

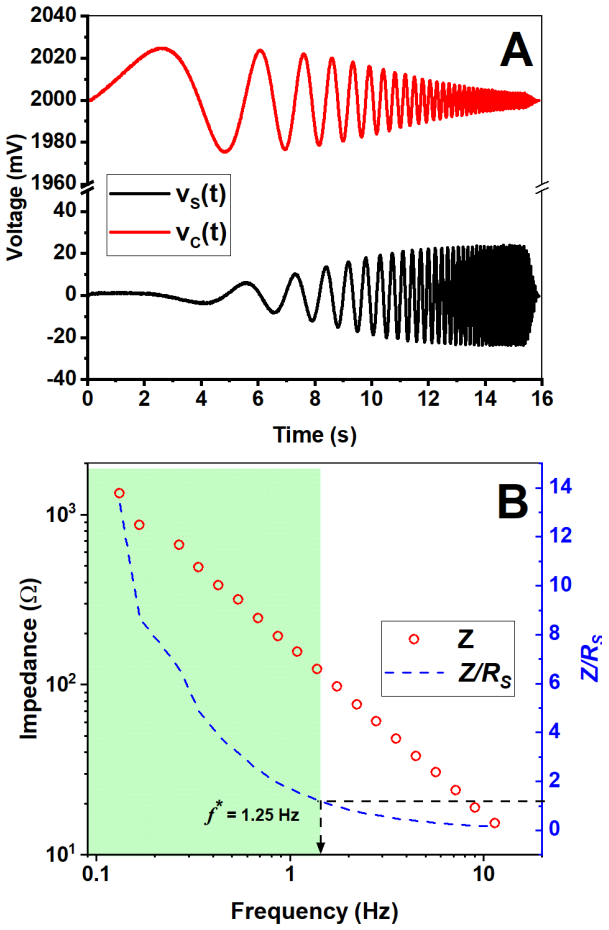

Figure B.7: (A) The voltage across the supercapacitor and the voltage across the shunt resistor ($R_S =$ 99.0Ω) when the chirp perturbation signal was applied ($f_{C,0} = 0.5 \times 0.126 = 0.063$ Hz, $f_{C,1} = 1.2 \times 12.6 =$ 15.1 Hz, $T = 15.88$ s). (B) The Bode plot of impedance for frequency band from 0.126 Hz to 12.6 Hz. The right axis indicates the ratio between the impedance of the supercapacitor Z and the shunt resistance R_S. The green shaded region indicates accurate EIS results.

Similarly, based on the shunt resistance $R_S =$ 99.9Ω, the highest frequency such that Eq. 5.5 holds is $f^* =$ 1.259 Hz. Therefore, EIS results from 0.12 Hz to 1.259 Hz are saved. Next, measurements continued from 1.25 Hz. Based on the impedance at 1.259 Hz, an appropriate shunt resistance ($R_S =$ 10.10Ω) was connected to the circuit, and then the instrument applied a chirp signal ($f_{C,0} = 0.5 \times 1.259 = 0.63$ Hz, $f_{C,1} = 1.2 \times 125.9 = 151.1$

Hz, $T = 1.58$ s) and measured $v_S(t)$ and $v_C(t)$, as shown in Fig. B.8A. The corresponding EIS results are shown in Fig. B.8B.

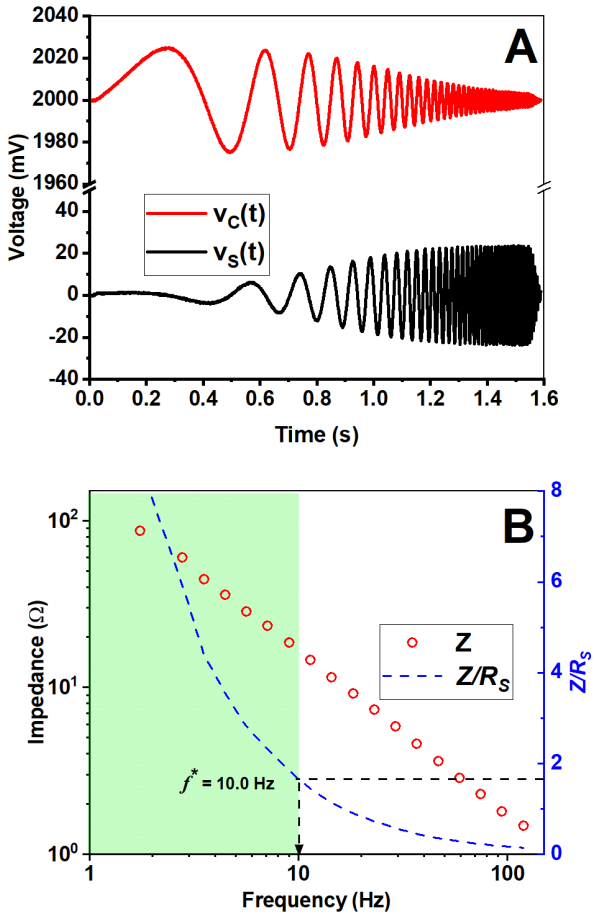

Figure B.8: (A) The voltage across the supercapacitor and the voltage across the shunt resistor ($R_S = 99.0\Omega$) when the chirp perturbation signal was applied ($f_{C,0} = 0.5 \times 0.126 = 0.063$ Hz, $f_{C,1} = 1.2 \times 12.6 = 15.1$ Hz, $T = 15.88$s). (B) The Bode plot of impedance for frequency band from 0.126 Hz to 12.6 Hz. The right axis indicates the ratio between the impedance of the supercapacitor Z and the shunt resistance R_S. The green shaded region indicates accurate EIS results.

For EIS measurement using $R_S = 10.10\Omega$, the highest frequency such that Eq. 5.5 holds is $f^* = 10$ Hz. Therefore, EIS results from 1.259 Hz to 10 Hz was stored, and measurement continued from 10 Hz and scanned the rest of the frequency band using a smaller shunt

resistance in the resistor band ($R_S = 2.73\Omega$). The measured voltage signals are shown in Fig. B.8A and corresponding EIS results are shown in Fig. B.9B. Because $R_S = 2.73\Omega$ is the smallest shunt resistance, all results are saved even if Eq. 5.5 does not hold for this frequency subband. The algorithm terminated once the entire frequency band was scanned, the complete EIS results are shown in Fig. 5.5A in the main document.

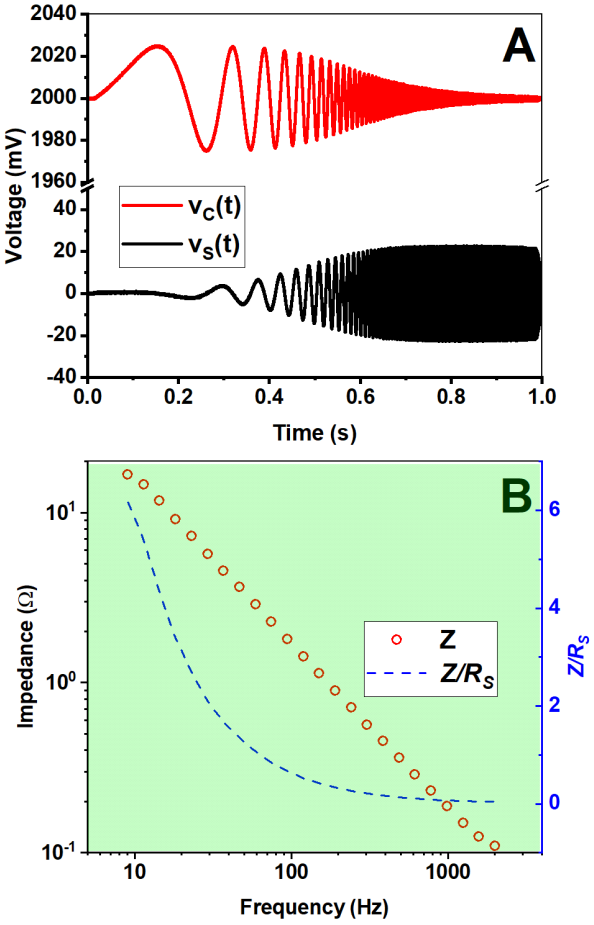

Figure B.9: (A) The voltage across the supercapacitor and the voltage across the shunt resistor ($R_S = 2.73\Omega$) when the chirp perturbation signal was applied ($f_{C,0} = 0.5 \times 2 = 1.0$ Hz, $f_{C,1} = 1.2 \times 2000 = 2400$Hz, $T = 1.0$ s). (B) The Bode plot of impedance for frequency band from 10 Hz to 2 kHz. The right axis indicates the ratio between the impedance of the supercapacitor Z and the shunt resistance R_S. The green shaded region indicates accurate EIS results.

B.4 Uncertainty quantification

The primary source of error in the custom instrument is random noise in the circuit, as shown in Fig. 5.1B. This leads to random noise in voltage measurements for both $v_S(t)$ and $v_C(t)$. Take random noise across the shunt resistor for example, the histogram of the noise signal is shown in Fig. B.10A and it exhibits bell shape. The corresponding auto-correlation function is shown in Fig. B.10B and very low correlation is observed for lags $N > 1$. Therefore, in this work random noise signals are modeled using Gaussian distributions. This section presents an approach to quantify the uncertainty in EIS measurement due to random noise in the circuit.

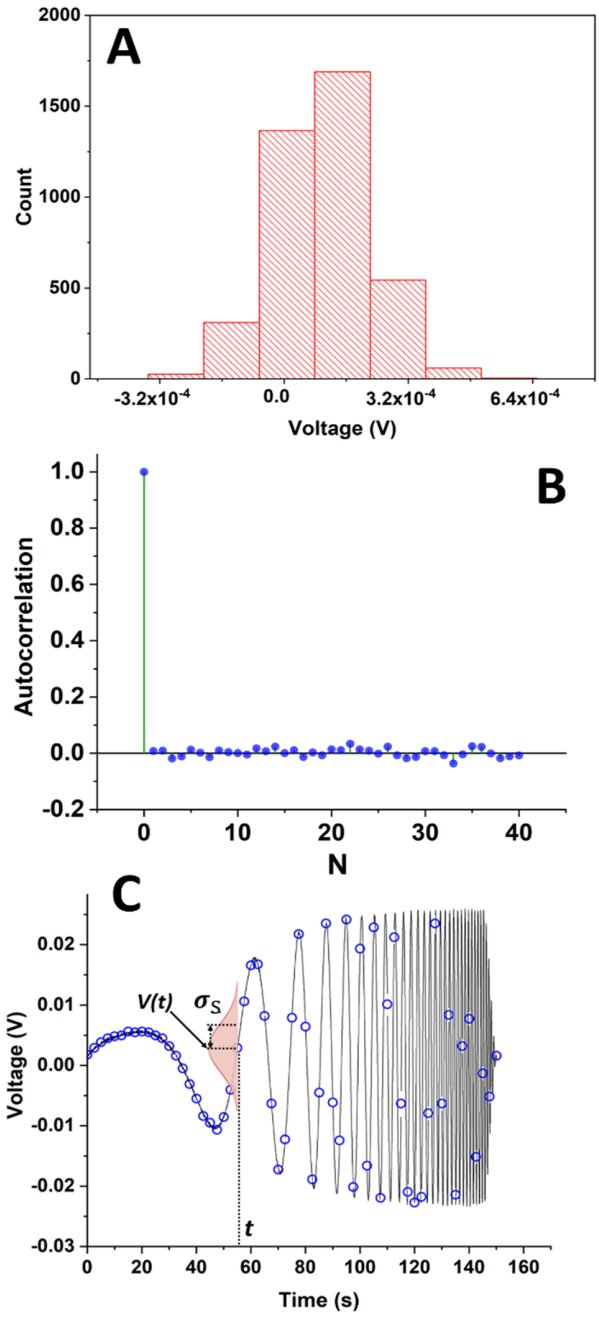

Figure B.10: (A) The histogram of the amplitude of random noise across the shunt resistor. (B) Autocorrelation plot of the noise signal in $v_S(t)$ measurement. (C) For a specific time t, the distribution of $v_S(t)$ given Gaussian noise in the circuit.

Because we cannot separate random noise from voltage signals during EIS measurements.

We measure the noise signals across the shunt resistor and the supercapacitor before EIS measurements. Based on the voltage noise samples $v_{S,noise}(n\Delta)$ and $v_{C,noise}(n\Delta)$, the corresponding standard deviations σ_S and σ_C are calculated. Typically, σ_S and σ_C fall between 0.1 - 0.2 mV.

In this work, a Monte Carlo method [127] is employed to quantify uncertainties in EIS results in the presence of random noise. To simulate random noise in $v_S(t)$ and $v_C(t)$ when chirp voltage perturbation is applied, we generate two arrays of Gaussian white noise with standard deviations σ_S and σ_C , and add these white noise to measured $v_S(n\Delta)$ and $v_C(n\Delta)$ respectively. We then compute EIS results using the measured signals with added noise. The same procedure is repeated one thousand times, and the 2.5 and 97.5 percentiles of the impedance and phase in the EIS Bode plot are extracted to represent the uncertainty intervals.

APPENDIX C

Appendix for high temperature Ångström's method study

C.1 Concentrated light source characterization

In this study the light source is controlled using an external 0-10 V programmable voltage source. In order to model the concentrated light source, we must have an expression for the total intensity as a function of the control voltage V. In this work, We heat the sample to steady state using a constant control voltage V. At steady state, the total energy absorbed from the concentrated light source and the surroundings equals to energy losses via radiation,

$$q(V) + q_{surr} = q_{radiation} \tag{C.1}$$

A schematic to analyze the energy balance is shown in Fig. C.1A. First we calculate $q_{radiation}$. An IR image for steady state heating is shown in Fig. C.1B. We isolate the sample using a digital mask and the processed image is shown in Fig. C.1C. We compute the total radiation power by taking the summation of pixel-wise radiation using the data in Fig. C.1C:

$$q_{radiation} = \Sigma_{i=1}^{N_p} \left(T(r_i)^4 \epsilon_{front}\, 2\pi\, r_i \Delta r + T(r_i)^4 \epsilon_{back}\, 2\pi\, r_i \Delta r \right) + 2\pi\, R\, d_z \epsilon T(R)^4 \tag{C.2}$$

where dz is the sample thickness, and $2\pi\, R\, d_z \epsilon T(R)^4$ indicates radiation from the edge.

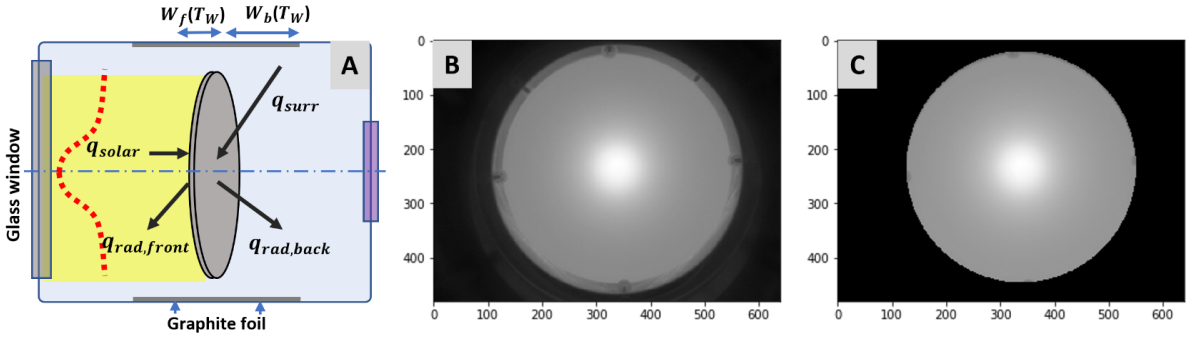

Figure C.1: (A) Schematic for solar simulator characterization system. (B) An IR image of the sample. (C) An IR image with a circular digital mask to isolate the sample for radiation calculation.

In this study a layer of graphite foil with high-emissivity coating is wrapped around the sample holder to minimize stray reflection. The graphite foil's temperatures T_W on the back side were measured using the IR camera and we assume the temperature is constant for the entire foil. The radiation from the graphite foil absorbed by the sample is calculated using:

$$q_{surr} = (A_f F_{fs} \sigma \, \epsilon_{front} + A_b F_{bs} \sigma \, \epsilon_{back}) T_w^4 \tag{C.3}$$

where A_f and A_b are the area of the graphite foil at the front and back side. F_{fs} and F_{bs} indicates the view factor between the graphite foil to the sample at the front and back side respectively.

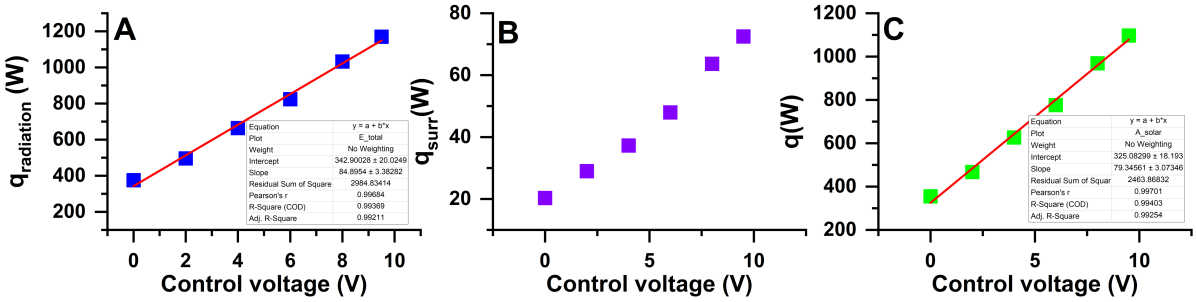

Figure C.2: (A) Total emissive power ($q_{radiation}$) of the sample measured at different control voltages. (B) Total absorption power measured from surrounding at different control voltages (q_{surr}). (C) Total energy absorbed by the sample from the concentrated light source $q(V)$ at different control voltages.

The intensity of the concentrated light source follows an Lorentzian distribution defined in Eq. 3.1 in the main paper. We integrate the intensity distribution over sample's radius R and further multiply with absorptivity of the sample η to obtain the rate of energy absorbed from the light source $q(V)$:

$$q(V) = \int_0^R \frac{\eta A(V)}{\pi} \frac{\sigma_{solar}}{\sigma_{solar}^2 + r^2} = 2\eta A(V)\sigma_{solar} \ln \frac{R^2 + \sigma_{solar}^2}{\sigma_{solar}^2} \tag{C.4}$$

Using Eq. C.1, $q(V)$ is further expressed as:

$$\begin{aligned} 2\eta A(V)\sigma_{solar} \ln \frac{R^2 + \sigma_{solar}^2}{\sigma_{solar}^2} =& \Sigma \left(T(r_i)^4 \epsilon_{front}\, 2\pi\, r_i \Delta r + T(r_i)^4 \epsilon_{back}\, 2\pi\, r_i \Delta r \right) \\ &+ 2\pi\, R\, d_z \epsilon T(R)^4 - (A_f F_{fs} \sigma\, \epsilon_{front} + A_b F_{bs} \sigma\, \epsilon_{back}) T_w^4 \end{aligned} \tag{C.5}$$

In this study, σ_{solar} is treated as a random variable and estimated using the Bayesian framework. For a specific σ_{solar}, the other parameter of the Lorentzian distribution $A(V)$ is determined using Eq. C.5.

C.2 Discretizing the governing equation and the Newton's solver

The governing equation of energy balance is expressed as:

$$\frac{\partial}{\partial r}\left(k\frac{\partial T}{\partial r}\right) + \frac{1}{r}\left(k\frac{\partial T}{\partial r}\right) + \frac{q_s^{"}}{dz} - \frac{(\epsilon_{back} + C_{lb,m}/(d\theta\, r\, dr))\sigma\, T^4}{dz} + \frac{q_{lb,m} + q_{surr,back}}{r\, dr\, d\theta\, dz} = \rho\, c_p \frac{\partial T}{\partial t} \tag{C.6}$$

The initial and the boundary conditions are:

$$\begin{cases} \text{IC: } t = 0,\ T(x,0) = T_i & \text{(C.7a)} \\ \text{BC: } r = R,\ -k\dfrac{\partial T}{\partial r} = \sigma(\epsilon T^4 - \eta\, T_W^4) & \text{(C.7b)} \\ \text{has to satisfy: } \dfrac{\partial T}{\partial r}|_{r=0} = 0 & \text{(C.7c)} \end{cases}$$

Eq. C.6 is discretized using the central-difference method, and thermal properties are evaluated at arithmetic mean temperature.

$$\begin{aligned} \frac{\partial}{\partial r}\left(k\frac{\partial T}{\partial r}\right) &= \frac{1}{\Delta r}[(\frac{k_{m+1}^{p-1}+k_m^{p-1}}{2}T_{m+1}^p - \frac{k_{m+1}^{p-1}+k_m^{p-1}}{2}T_m^p)\Delta r \\ &- (\frac{k_m^{p-1}+k_{m-1}^{p-1}}{2}T_m^p - \frac{k_m^{p-1}+k_{m-1}^{p-1}}{2}T_{m-1}^p)\Delta r] \\ &= \frac{1}{2\Delta r^2}\left[(k_{m+1}^{p-1}+k_m^{p-1})T_{m+1}^p - (k_{m+1}^{p-1}+2k_m^{p-1}+k_{m-1}^{p-1})T_m^p + (k_{m+1}^{p-1}+k_m^{p-1})T_{m-1}^p\right] \end{aligned} \tag{C.8}$$

$$\frac{k}{r}\frac{\partial T}{\partial r} = \frac{k_m^{p-1}}{r}\frac{T_{m+1}^p - T_{m-1}^p}{2\Delta r} = \frac{k_m^{p-1}(T_{m+1}^p - T_{m-1}^p)}{2\,r\,\Delta r} \tag{C.9}$$

$$\rho c_p \frac{\partial T}{\partial t} = \rho c_p \frac{T_m^p - T_m^{p-1}}{\Delta t} \tag{C.10}$$

The discretized governing equation for a node m and at time step p is further expressed as:

$$T_m^{p-1} = A_m\, T_{m-1}^p + B_m\, T_m^p + C_m\, T_{m+1} + D_m\, T_m^{p4} + E_m + F_m \tag{C.11}$$

where

$$A_m = -\frac{\alpha_{ba}\Delta t}{\Delta r^2} + \frac{\Delta t \alpha}{2\,r\,\Delta r}\,,\ \alpha = \frac{k_m^{p-1}}{\rho c_m^{p-1}}\,,\ \alpha_{ba} = \frac{k_m^{p-1}+k_{m-1}^{p-1}}{2\rho c_m^{p-1}} \tag{C.12}$$

$$B_m = \frac{2\Delta t}{\Delta r^2}\alpha_{ce} + 1\,,\ \alpha_{ce} = \frac{k_{m+1}^{p-1}+2k_m^{p-1}+k_{m-1}^{p-1}}{4\rho c_m^{p-1}} \tag{C.13}$$

$$C_m = -\frac{\Delta t}{\Delta r^2}\alpha_{fo} - \frac{\Delta t \alpha}{2r\Delta r}\,,\ \alpha_{fo} = \frac{k_{m+1}^{p-1}+k_m^{p-1}}{2\rho c_m^{p-1}} \tag{C.14}$$

$$D_m = \frac{(C_{lb}/(2\pi r \Delta r) + \epsilon_{back})\sigma\, \Delta t}{dz\, \rho\, c_m^{p-1}} \tag{C.15}$$

$$E_m = -\frac{q_s^{"} \Delta t}{dz\, \rho\, c_m^{p-1}} \tag{C.16}$$

$$F_m = -\frac{q_{lb,m} + q_{surr,back}}{r\, dr\, dz} \frac{\Delta t}{\rho c_m^{p-1}} \tag{C.17}$$

For $r = 0$, the governing equation has to satisfy the symmetry condition. Here we introduce a ghost node T_{-1}^p. Using central diffence, the symmetry condition is expressed as:

$$\frac{\partial T}{\partial r} = \frac{T_{-1}^p - T_1^p}{2\Delta r} \tag{C.18}$$

Therefore, $T_{-1}^p = T_1^p$. The finite difference equation for the node at the center $r = 0$ is expressed as:

$$T_0^{p-1} = (A_0 + C_0)T_1^p + B_0\, T_0^p + D_0\, T_0^4 + E_0 + F_0 \tag{C.19}$$

Consider the boundary condition at $r = R$. We introduce another ghost node outside domain T_{N+1}^p. Using central difference method, Eq. C.7b is discretized as:

$$-k_N^{p-1} \frac{T_{N+1}^p - T_{N-1}^p}{2\Delta r} = \sigma(\epsilon T^4 - \eta T_W^4) \tag{C.20}$$

The temperature at the last node is:

$$T_N^{p-1} = (A_N + C_N)T_{N-1}^p + B_N\, T_N^p + (D_N - \frac{2C_N\, \Delta r\, \sigma\, \epsilon}{k_N^{p-1}})T_N^{p4} + E_N + F_N + \frac{2\Delta r\, \sigma\, \eta\, T_W^4\, C_N}{k_N^{p-1}} \tag{C.21}$$

The finite difference equations (Eq. C.19, Eq. C.11 and Eq. C.21) are solved implicitly using Newton-Raphson's method. Here we denote temperatures before and after Newton-Raphson update as $T^{'}$ and T. If we define the residual using:

$$G = -T_m^{p-1} + A_m\, T_{m-1}^p + B_m\, T_m^p + C_m\, T_{m+1} + D_m\, T_m^{p4} + E_m + F_m \tag{C.22}$$

Using Newton-Ralphson's method we obtain:

$$J(T^{'})(T - T^{'}) = -G(T^{'}) \tag{C.23}$$

where $J(\cdot)$ indicates the Jacobian matrix for G and is shown below:

$$\left\{\begin{matrix} B_0 + 4D_0 T_0^{'P3}, & A_0 + C_0, & 0 & 0 & 0 & 0 & ..... \\ 0 & ... & A_m, & B_m, & C_m, & 0 & ..... \\ 0 & 0 & 0 & 0 & ... & A_N + C_N, & B_N + 4(D_N - \frac{2C_N \Delta r \sigma \epsilon}{k_N^{p-1}}) T_N^{'p3} \end{matrix}\right\}$$
$$\times \begin{bmatrix} \delta T_0 \\ \delta T_1 \\ ... \\ \delta T_N \end{bmatrix} = - \begin{bmatrix} G_0(T^{'}) \\ G_1(T^{'}) \\ ... \\ G_N(T^{'}) \end{bmatrix} \tag{C.24}$$

At a given time step temperature is updated as:

$$T = T^{'} + \delta T \tag{C.25}$$

For each time step the convergence criteria is $\delta T < 10^{-12}$ K.

A mesh independent study is conducted to determine the optimal number of nodes for the 1D transient heat transfer simulation. We examine the relative error in transient temperature profiles, amplitude decay and phase shift for simulations with fewer number of nodes compared to simulation with high number of nodes ($N = 600$). As observed in Fig. C.3, choosing $N \approx 200$ yields high accuracy (less than 0.1%) and fast computing speed (approx. 40 s compared to 5 mins with $N = 600$). In this study, we discretize the radius of the sample with approx. 220 nodes.

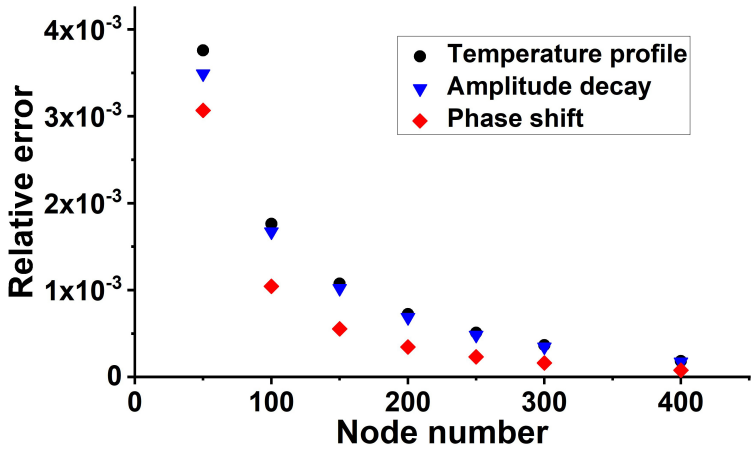

Figure C.3: Relative error in amplitude decay, phase shift and transient temperature profiles with increased number of nodes.

C.3 Light blocker temperature measurement

In this study the light blocker is closely placed in front of the sample so that the intensity of the truncated light source can be modeled with a simple window function shown in Fig. 3.1C. Placing thermocouples on the light blocker is difficult because of tight space. Because the light blocker facing the sample is coated with high temperature high-emissivity coating, we use the IR camera to measure the light blocker temperature along the radial direction. We used a disk that is identical to samples under test and cut a narrow slot along the radial direction. We heat the sample with slot to identical working conditions (the same bias control voltage) and measure the temperature of the narrow slot using the IR camera. An IR image for the sample with slot is shown in Fig. C.4A and the steady temperatures measured at different radius is shown in Fig. C.4B.

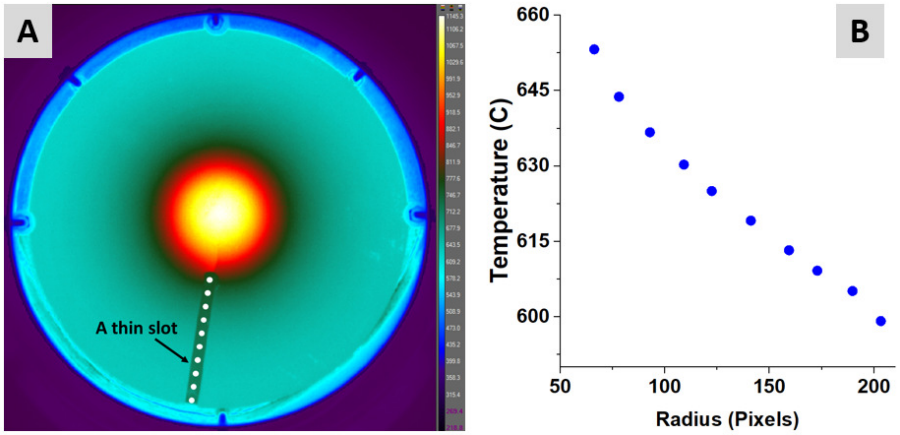

Figure C.4: (A) An IR image for a sample with a narrow slot for light blocker temperature measurements. (B) Measured light blocker temperature at different radial locations.

However, because of the slot on the disk, the measured light blocker temperature defers from that without the slot. The light blocker temperature is also difficult to determine precisely because reflection from the front side of the sample (facing the solar simulator) is difficult to quantify. However, because of the high-emissivity coating on the light blocker, the error caused by unknown reflection is estimated to be less than 20 K. To mitigate these system errors, we treated the light blocker temperature $T(r)$ as a random variable and assumed it equals to the temperatures measured by the IR camera $T_{IR}(r)$ plus an unknown bias temperature:

$$T(r) = T_{IR}(r) + T_{bias} \tag{C.26}$$

We employ the Bayesian framework to estimate the unknown bias temperature T_{bias}.

C.4 Effect of random noise at high temperatures

Under extreme temperatures high noise exist, as shown in Fig. 3.1B. Therefore, to reduce such random noise, we average the pixels along the isothermal locations, i.e. constant radius as shown in Fig. C.5A. Our approach is to convert temperature measurements in a Cartesian coordinate shown in Fig. C.5A to a polar coordinate using bilinear interpolation illustrated

in Fig. C.5B.

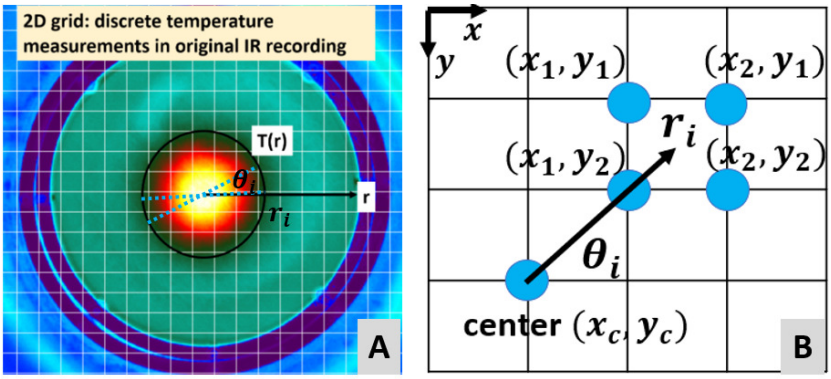

Figure C.5: (A) Temperature data in Cartesian coordinate. (B) Average Cartesian temperature data to polar coordinate using bilinear interpolation.

First we identify the center of the light source (x_c, y_c). Then for each discrete radius r_i ($r_i \in [1, 2...N]$, unit pixels), we divide it into N_{angle} evenly spaced points along the circle. To estimate the temperature of a particular point at angle θ_i, we employ bilinear interpolation using the nearest four temperature data in Cartesian coordinate using Eq. C.27. We averaged temperatures obtained at 200 evenly spaced θ_i ranging from 0 to 2π to get the mean temperature at r_i. Then the procedure is repeated to get all the mean temperatures along the sample's radial direction. Lastly we employ parallel computing to execute the foregoing process for all images in an IR recording. The final result is averaged radial temperatures as a function of time shown in Fig. 3.5C.

$$T(R,\theta) \approx \frac{y_2 - R\sin(\theta)}{y_2 - y_1} T\left(R\cos(\theta), y_1\right) + \frac{R\sin(\theta) - y_1}{y_2 - y_1} T(R\cos(\theta), y_2) \tag{C.27}$$

C.5 Amplitude decay and phase shift calculation

Given two quasi-steady-state oscillating temperature profiles $v_1(t)$ and $v_2(t)$. The amplitude decay ΔA and phase shift $\Delta\phi$ are calculated using a discrete Fourier transform (DFT), where

$n\Delta$ indicates discrete samples.

$$dA = \left| \frac{\mathrm{DFT}(v_1(n\Delta))}{\mathrm{DFT}(v_2(n\Delta))} \right| \ , \ d\phi = \angle \frac{\mathrm{DFT}(v_1(n\Delta))}{\mathrm{DFT}(v_2(n\Delta))} \tag{C.28}$$

For an IR image shown in Fig. C.6A, we divide such an image into eight areas and analyze amplitude and phase within each area bounded by dashed blue lines and the region of interest (bounded by dashed red and black lines). The corresponding amplitude decay and phase shift results are shown in Fig. C.6B and C respectively.

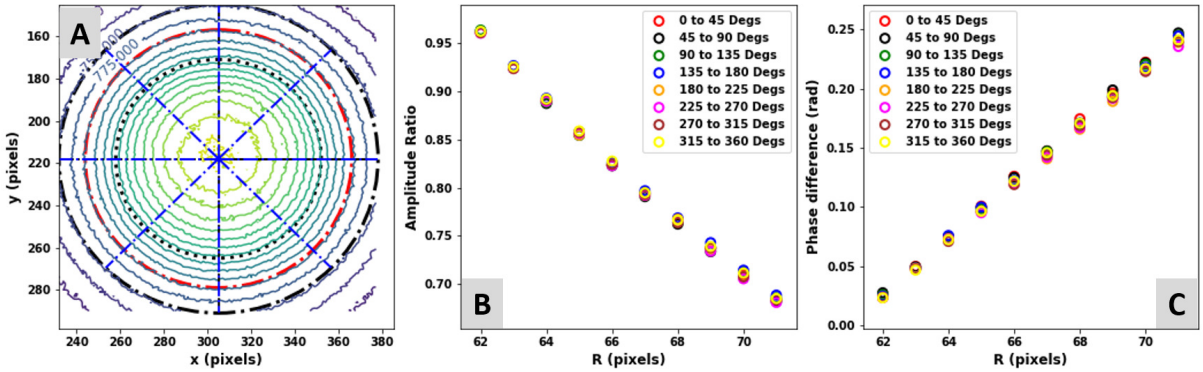

Figure C.6: (A) Temperature contour plot of an IR image. The black dots indicate the area irradiated by the concentrate light source. The region of analysis for amplitude and phase is bounded by the red and black dashed line. (B) Amplitude decay for different angular regions (shown in A) on the sample. (C) Phase shift for different angular regions (shown in A) on the sample.

REFERENCES

[1] ACTE, "ACTE Supercapacitors Datasheet", accessed Jan 01, 2018, http://www.acte-uk.com/technologies/ultracapacitors.

[2] Aremco Product Inc., "High Temperature High Emissivity Coatings", accessed Feb 02, 2020, https://www.aremco.com/high-emissivity-coatings/.

[3] Entegris, "Graphite Properties and Characteristics, Entegris", accessed June 19, 2020, https://poco.entegris.com/content/dam/poco/resources/reference-materials/brochures/brochure-graphite-properties-and-characteristics-11043.pdf.

[4] ESPI Metals, "ESPI Metal Data Sheet for Copper", accessed Jan 01, 2018, https://www.espimetals.com/index.php/online-catalog/357-copper.

[5] FLIR Systems, Inc., "User's Manual FLIR A6xx Series", accessed Feb 02, 2020, https://www.flir.com/products/a655sc/.

[6] Greencap Supercapacitor, "Greencap Supercapacitor Datasheet", accessed Jan 01, 2018, http://www.masters.com.pl/files/ds/samwha/samwha-green-cap.pdf.

[7] Matt Pitkin, "Using a Black Box Likelihood Function", accessed Feb 02, 2020, http://mattpitkin.github.io/samplers-demo/pages/pymc3-blackbox-likelihood/.

[8] Maxwell Technologies, "Supercapacitor Datasheet", accessed Jan 01, 2018, http://www.maxwell.com/products/ultracapacitors/16v-small-modules.

[9] Misumi USA, "Air Nozzles Compact Type AFTC7", accessed Jan 01, 2019, https://us.misumi-ec.com/pdf/fa/2019/2019-us-3552.pdf.

[10] National Instruments, "Compact Data Acquisition System White Paper", accessed Jan 01, 2017, http://www.ni.com/product-documentation/53090/en/.

[11] Superior Quartz Products, INC., "Lamp Characteristics and Description", accessed Feb 02, 2020, https://www.sqpuv.com/pdfs/technicalspecificationguide.pdf.

[12] Z Abdulagatova, S Kallaev, Z Omarov, A Bakmaev, B Grigor'ev, and I Abdulagatov. Temperature Effect on Thermal-Diffusivity and Heat-Capacity and Derived Values of Thermal-Conductivity of Reservoir Rock Materials. *GEOMECH GEOPHYS GEO.*, 6(1):1–23, 2020.

[13] B. Abeles, G. Cody, and D. Beers. Apparatus for the Measurement of the Thermal Diffusivity of Solids at High Temperatures. *J. Appl. Phys.*, 31(9):1585–1592, 1960.

[14] M Abuseada, C Ophoff, and N Ozalp. Characterization of a New 10 kWe High Flux Solar Simulator via Indirect Radiation Mapping Technique. *J. Sol. Energy Eng.*, 141(2), 2019.

[15] M Acerce, D Voiry, and M Chhowalla. Metallic 1T Phase MoS 2 Nnanosheets as Supercapacitor Electrode Materials. *Nat. Nanotechnol*, 10(4):313–318, 2015.

[16] W. Adamczyk, R. Białecki, H. Orlande, and Z. Ostrowski. Nondestructive, Real Time Technique for in-Plane Heat Diffusivity measurements. *Int. J. Heat Mass Transf.*, 154:119659, 2020.

[17] P Agarwal, M Orazem, and L Garcia-Rubio. Measurement Models for Electrochemical Impedance Spectroscopy: I. Demonstration of Applicability. *J. Electrochem. Soc.*, 139(7):1917, 1992.

[18] M Akoshima and T Baba. Study on a Thermal-Diffusivity Standard for Laser Flash Method Measurements. *Int. J. Thermophys.*, 27(4):1189–1203, 2006.

[19] A Allard, N Fischer, G Ebrard, B Hay, P Harris, L Wright, D Rochais, and J Mattout. A Multi-thermogram-based Bayesian Model for the Determination of the Thermal Diffusivity of a Material. *Metrologia*, 53(1):S1, 2015.

[20] A. Angström. XVII. New Method of Determining the Thermal Conductibility of Bodies. *Philos. Mag.*, 25(166):130–142, 1863.

[21] Richard C Aster, Brian Borchers, and Clifford H Thurber. *Parameter Estimation and Inverse Problems*, pages 279–280. Elsevier, 2018.

[22] A Bar-Cohen and P Wang. Thermal Management of on-Chip Hot Spot. *J of HEAT TRANSFER-TRANSACTIONS OF THE ASME*, 134(5):051017, 2012.

[23] J Berger, H Orlande, and N Mendes. Proper Generalized Decomposition Model Reduction in the Bayesian Framework for Solving Inverse Heat Transfer Problems. *Inverse Probl Sci Eng.*, 25(2):260–278, 2017.

[24] T.L. Bergman, F.P. Incropera, A.S. Lavine, and D.P. Dewitt. *Introduction to Heat Transfer*, pages 311–314. John Wiley & Sons, 2011.

[25] M Betancourt. A Conceptual Introduction to Hamiltonian Monte Carlo. *arXiv preprint arXiv:1701.02434*, pages 1–60, 2017.

[26] L Biegler, G Biros, O Ghattas, M Heinkenschloss, D Keyes, B Mallick, L Tenorio, B van Bloemen Waanders, K Willcox, and Y Marzouk. *Large-Scale Inverse Problems and Quantification of Uncertainty*, volume 712, pages 123–144. John Wiley & Sons, 2011.

[27] K Bochenek and M Basista. Advances in Processing of NiAl Intermetallic Alloys and Composites for High Temperature Aerospace Applications. *Prog. Aerosp. Sci.*, 79:136–146, 2015.

[28] VL Borges, S De Lima E Silva, and G Guimarães. A Dynamic Thermal Identification Method Applied to Conductor and Nonconductor Materials. *Inverse Probl Sci Eng.*, 14(5):511–527, 2006.

[29] S Brahim, E Indra, S Zhang, R Sy, P Bonzato, and S Maat. Supercapacitors Using Binder-Free & Surfactant-Free CNT Electrodes. *ECS Trans*, 75(24):13, 2017.

[30] S Brahim, S Zhang, and S Maat. Fabrication and Performance of Supercapacitor Devices Using Binder-Free CNT Electrodes. In *ECS Meeting Abstracts*, number 1, page 82. IOP Publishing, 2018.

[31] T Bress. *Effective LabVIEW Programming*, pages 90–97. Nts Press, 2013.

[32] S. Brooks, A. Gelman, G. Jones, and X. Meng. *Handbook of Markov Chain Monte Carlo*, pages 114–132. CRC Press, 2011.

[33] S Buller, M Thele, R De Doncker, and E Karden. Impedance-Based Simulation Models of Ssupercapacitors and Li-ion Batteries for Power Electronic Applications. *IEEE Trans. Ind. Appl.*, 41(3):742–747, 2005.

[34] A.F Burke. Batteries and Ultracapacitors for Electric, Hybrid, and Fuel Cell Vehicles. *Proc. IEEE.*, 95(4):806–820, 2007.

[35] S. Butterworth. On the Theory of Filter Amplifiers. *Wireless Engineer*, 7(6):536–541, 1930.

[36] D. G. Cahill. Thermal Conductivity Measurement from 30 to 750 K: the 3 Omega Method. *Rev. Sci. Instrum.*, 61(2):802–808, 1990.

[37] H Chen, T Cong, W Yang, C Tan, Y Li, and Y Ding. Progress in Electrical Energy Storage System: A Critical Review. *Prog. Nat. Sci. PROG NAT SCI-MATER*, 19(3):291–312, 2009.

[38] W Chen, L Jiang, R Pathak, and F Wu. Sb2S3/TiO2 Heterojunction Solar Cells Based on Carbon Electrode with Higher Photocurrent. *ECS J. Solid State Sci. Technol*, 8(4):Q67, 2019.

[39] X Chen, R Paul, and L Dai. Carbon-Based Supercapacitors for Efficient Energy Storage. *Natl. Sci. Rev.*, 4(3):453–489, 2017.

[40] F. Chu, R. Taylor, and A. Donaldson. Thermal Diffusivity Measurements at High Temperatures by the Radial Flash Method. *J. Appl. Phys.*, 51(1):336–341, 1980.

[41] L. Clark Iii and R. Taylor. Radiation Loss in the Flash Method for Thermal Diffusivity. *J. Appl. Phys.*, 46(2):714–719, 1975.

[42] R. Cowan. Proposed Method of Measuring Thermal Diffusivity at High Temperatures. *J. Appl. Phys.*, 32(7):1363–1370, 1961.

[43] K Darowicki and P Ślepski. Determination of Electrode Impedance by Means of Exponential Chirp Signal. *Electrochem. Commun.*, 6(9):898–902, 2004.

[44] R De Levie. On Porous Electrodes in Electrolyte Solutions: I. Capacitance Effects. *Electrochim. Acta*, 8(10):751–780, 1963.

[45] S Duane, A.D Kennedy, B J Pendleton, and D Roweth. Hybrid Monte Carlo. *Phys. Lett. B.*, 195(2):216–222, 1987.

[46] D.B. Dunson. Commentary: Practical Advantages of Bayesian Analysis of Epidemiologic Data. *Am J Epidemiol.*, 153(12):1222–1226, 2001.

[47] AF Emery. Stochastic Regularization for Thermal Problems with Uncertain Parameters. *Inverse Probl Sci Eng.*, 9(2):109–125, 2001.

[48] J. Feinberg and P. Langtangen. Chaospy: An Open Source Tool for Designing Methods of Uncertainty Quantification. *J. Comput. Sci.*, 11:46–57, 2015.

[49] P Feldmann and R.W Freund. Efficient Linear Circuit Analysis by Padé Approximation via the Lanczos Process. *IEEE TCAD.*, 14(5):639–649, 1995.

[50] R. A. Fisher. Frequency Distribution of the Values of the Correlation Coefficient in Samples from an Indefinitely Large Population. *Biometrika.*, 10(4):507–521, 1915.

[51] A Gelman, D.B Rubin, et al. Inference from Iterative Simulation using Multiple Sequences. *Stat. Sci.*, 7(4):457–472, 1992.

[52] P M Gomadam and J.W. Weidner. Analysis of Electrochemical Impedance Spectroscopy in Proton Exchange Membrane Fuel Cells. *Int. J. Energy Res.*, 29(12):1133–1151, 2005.

[53] F. Gomez-Garcia, S. Santiago, S. Luque, M. Romero, and J. Gonzalez-Aguilar. A New Laboratory-Scale Experimental Facility for Detailed Aerothermal Characterizations of Volumetric Absorbers. In *AIP Conference Proceedings*, volume 1734, page 030018. AIP Publishing LLC, 2016.

[54] D Gottlieb and S.A Orszag. *Numerical Analysis of Spectral Methods: Theory and Applications*, pages 1–156. SIAM, 1977.

[55] S. Gustafsson. Transient Plane Source Techniques for Thermal Conductivity and Thermal Diffusivity Measurements of Solid Materials. *Rev. Sci. Instrum.*, 62(3):797–804, 1991.

[56] S.E Gustafsson, E Karawacki, and M.N Khan. Transient Hot-Strip Method for Simultaneously Measuring Thermal Conductivity and Thermal Diffusivity of Solids and Fluids. *J. Phys. D Appl. Phys.*, 12(9):1411, 1979.

[57] M Gustavsson, E Karawacki, and S.E Gustafsson. Thermal Conductivity, Thermal Diffusivity, and Specific Heat of Thin Samples From Transient Measurements with Hot Disk Sensors. *Rev. Sci. Instrum.*, 65(12):3856–3859, 1994.

[58] J Hahn, T Reid, and A Marconnet. Infrared Microscopy Enhanced Angstrom's Method for Thermal Diffusivity of Polymer Monofilaments and Films. *J of HEAT TRANSFER-TRANSACTIONS OF THE ASME*, 141(8):081601, 2019.

[59] M. Hao, K. R. Saviers, and T. S. Fisher. Design and Validation of a High-Temperature Thermal Interface Resistance Measurement System. *J. Thermal Sci. Eng. Appl.*, 8(3):031008, 2016.

[60] I. Hatta, Y. Sasuga, R. Kato, and A. Maesono. Thermal Diffusivity Measurement of Thin Films by Means of an AC Calorimetric Method. *Rev. Sci. Instrum.*, 56(8):1643–1647, 1985.

[61] J. Healy, J. De Groot, and J. Kestin. The Theory of the Transient Hot-Wire Method for Measuring Thermal Conductivity. *Physica B+C*, 82(2):392–408, 1976.

[62] S.R. Hinton. Chainconsumer. *J. Open Source Softw.*, 1(4):00045, 2016.

[63] M. Hoffman and A. Gelman. The No-U-Turn sampler: Adaptively Setting Path Lengths in Hamiltonian Monte Carlo. *J. Mach. Learn. Res.*, 15(1):1593–1623, 2014.

[64] L. Howarth. On the Solution of the Laminar Boundary Layer Equations. *Proc. Royal Soc. A.*, pages 547–579, 1938.

[65] Y Hu, S Brahim, S Maat, P Davies, A Kundu, and T.S Fisher. Rapid Analytical Instrumentation for Electrochemical Impedance Spectroscopy Measurements. *J. Electrochem. Soc.*, 167(2):027545, 2020.

[66] Y Hu and T.S Fisher. Suggested Standards for Reporting Power and Energy Density in Supercapacitor Research. *Bull. Mater. Sci.*, 41(5):1–4, 2018.

[67] Y. Hu and T.S. Fisher. Accurate Thermal Diffusivity Measurements Using a Modified Ångström's Method With Bayesian Statistics. *J of HEAT TRANSFER-TRANSACTIONS OF THE ASME*, 142(7):071401, 2020.

[68] Yuan Hu. "Angstrom's Method for High Temperature Thermal Diffusivity Characterization Python Module pyangstromHT", https://doi.org/10.5281/zenodo.4587868, 2021.

[69] T. Katsura. Thermal Diffusivity of Silica Glass at Pressures up to 9 GPa. *Phys Chem Miner.*, 20(3):201–208, 1993.

[70] R Kötz and M Carlen. Principles and Applications of Electrochemical Capacitors. *Electrochim. Acta*, 45(15-16):2483–2498, 2000.

[71] B Lamien, D Le Maux, M Courtois, T Pierre, M Carin, P Le Masson, H.R.B Orlande, and P Paillard. A Bayesian Approach for the Estimation of the Thermal Diffusivity of Aerodynamically Levitated Solid Metals at High Temperatures. *Int. J. Heat Mass Transf.*, 141:265–281, 2019.

[72] Wah Lau and CW Tan. Errors in One-Dimensional Heat Transfer Analysis in Straight and Annular Fins. *J of HEAT TRANSFER-TRANSACTIONS OF THE ASME*, pages 723–727, 1973.

[73] Z Li, Y Yao, Y Zheng, T Gao, Z Liu, and G Zhou. Fabrication of core-shell Fe3O4-C-MnO2 Microspheres and Their Application in Supercapacitors. *J. Electrochem. Soc.*, 165(2):E58, 2018.

[74] T Lin, I Chen, F Liu, C Yang, H Bi, F Xu, and F Huang. Nitrogen-Doped Mesoporous Carbon of Extraordinary Capacitance for Electrochemical Energy Storage. *Science*, 350(6267):1508–1513, 2015.

[75] J Liu and R Yang. Tuning the Thermal Conductivity of Polymers with Mechanical Strains. *Phys. Rev. B.*, 81(17):174122, 2010.

[76] F Loguercio, F de Matos, M de Oliveira, G Marin, S Khan, J Dupont, S.R. Teixeira, N.M. Balzaretti, J Santos, and M Santos. Polypyrrole/Ionic Liquid/Au Nanoparticle Counter-Electrodes for Dye-Sensitized Solar Cells: Improving Charge-Transfer Resistance at the CE/Electrolyte Interface. *J. Electrochem. Soc.*, 166(5):H3188, 2019.

[77] E. Lopez-Baeza, J. D. H. Rubia, and H. J. Goldsmid. Angstrom's Thermal Diffusivity Method for Short Samples. *J. Phys. D.*, 20(9):1156, 1987.

[78] John Leask Lumley. The Structure of Inhomogeneous Turbulent Flows. *Atmospheric turbulence and radio wave propagation*, pages 166–177, 1967.

[79] V.C Mariani and L dos Santos Coelho. Estimation of the Apparent Thermal Diffusivity Coefficient using an Inverse Technique. *Inverse Probl Sci Eng.*, 17(5):569–589, 2009.

[80] M Mateos, M Tchangaï, R Meunier-Prest, O Heintz, F Herbst, J Suisse, and M Bouvet. Low Conductive Electrodeposited Poly (2, 5-dimethoxyaniline) as a Key Material in a Double Lateral Heterojunction, for sub-ppm Ammonia Sensing in Humid Atmosphere. *ACS sensors*, 4(3):740–747, 2019.

[81] N. Metropolis, A. Rosenbluth, M. Rosenbluth, A. Teller, and E. Teller. Equation of State Calculations by Fast Computing Machines. *J. Chem. Phys.*, 21(6):1087–1092, 1953.

[82] S Miao, H Li, and G Chen. Temperature Dependence of Thermal Diffusivity, Specific Heat Capacity, and Thermal Conductivity for Several Types of Rocks. *J. Therm. Anal. Calorim.*, 115(2):1057–1063, 2014.

[83] S Min, J Blumm, and A Lindemann. A New Laser Flash System for Measurement of the Thermophysical Properties. *Thermochim. Acta.*, 455(1-2):46–49, 2007.

[84] S Mondal, U Rana, and S Malik. Graphene Quantum Dot-Doped Polyaniline Nanofiber as High Performance Supercapacitor Electrode Materials. *Chem.Commun*, 51(62):12365–12368, 2015.

[85] D. Montgomery. *Design and Analysis of Experiments*, pages 183–225. John Wiley & Sons, 2012.

[86] A.L. Moore and L Shi. Emerging Challenges and Materials for Thermal Management of Electronics. *Mater. Today*, 17(4):163–174, 2014.

[87] B Moore. Principal Component Analysis in Linear Systems: Controllability, Observability, and Model Reduction. *IEEE Trans. Automat. Contr.*, 26(1):17–32, 1981.

[88] A. Muscio, P. G. Bison, S. Marinetti, and E. Grinzato. Thermal Diffusivity Measurement in Slabs using Harmonic and One-Dimensional Propagation of Thermal Waves. *Int J. Therm Sci.*, 43(5):453–463, 2004.

[89] H Nara, D Mukoyama, R Shimizu, T Momma, and T Osaka. Systematic Analysis of Interfacial Resistance Between the Cathode Layer and the Current Collector in Lithium-ion Batteries by Electrochemical Impedance Spectroscopy. *J. Power Sources.*, 409:139–147, 2019.

[90] M Newville, T Stensitzki, D B Allen, M Rawlik, A Ingargiola, and A Nelson. LMFIT: Non-Linear Least-Square Minimization and Curve-Vitting for Python. *ASCL.*, pages ascl–1606, 2016.

[91] S. Ostrach. An Analysis of Laminar Free-Convection Flow and Heat Transfer about a Flat Plate Parallel to the Direction of the Generating Body Force. Technical Report NACA-TN-2635, National Aeronautics and Space Administration Cleveland Oh Lewis Research Center, 1952.

[92] N.E Owen, P Challenor, P.P Menon, and S Bennani. Comparison of Surrogate-based Uncertainty Quantification Methods for Computationally Expensive Simulators. *SIAM-ASA J UNCERTAIN.*, 5(1):403–435, 2017.

[93] N.P. Padture. Advanced Structural Ceramics in Aerospace Propulsion. *Nat. Mater*, 15(8):804–809, 2016.

[94] D. G Park, H. M. Kim, S. J. Baik, K. H. Kim, S. B. Ahn, and W. S. Ryu. Heat Loss Effects of Laser Flash Method for Low Thermal Diffusivity Materials. In *Proceedings of the KNS autumn meeting*, pages 29–30, Oct 2009.

[95] W. Parker, R. Jenkins, C. Butler, and G. Abbott. Flash Method of Determining Thermal Diffusivity, Heat Capacity, and Thermal Conductivity. *J. Appl. Phys.*, 32(9):1679–1684, 1961.

[96] G Popkirov and R Schindler. A new Impedance Spectrometer for the Investigation of Electrochemical Systems. *Rev. Sci. Instrum.*, 63(11):5366–5372, 1992.

[97] A. Prasad and A. Ambirajan. Criteria for Accurate Measurement of Thermal Diffusivity of Solids using the Angstrom Method. *Int. J Therm Sci.*, 134:216–223, 2018.

[98] F Rafik, H Gualous, R Gallay, A Crausaz, and A Berthon. Frequency, Thermal and Voltage Supercapacitor Characterization and Modeling. *J. Power Sources*, 165(2):928–934, 2007.

[99] T Reshetenko and A Kulikovsky. A Model for Extraction of Spatially Resolved Data from Impedance Spectrum of a PEM Fuel Cell. *J. Electrochem. Soc.*, 165(5):F291, 2018.

[100] P Rousseau, C Du Toit, W Van Antwerpen, and H.J. Van Antwerpen. Separate Effects Tests to Determine the Effective Thermal Conductivity in the PBMR HTTU Test Facility. *Nucl. Eng. Des.*, 271:444–458, 2014.

[101] J. Rynn, S. Cotter, C Powell, and L. Wright. Surrogate Accelerated Bayesian Inversion for the Determination of the Thermal Diffusivity of a Material. *Metrologia*, 56(1):015018, 2019.

[102] R Salunkhe, C Young, J Tang, T Takei, Y Ide, N Kobayashi, and Y Yamauchi. A High-Performance Supercapacitor Cell Based on ZIF-8-Derived Nanoporous Carbon using an Organic Electrolyte. *Chem.Commun*, 52(26):4764–4767, 2016.

[103] J. Salvatier, T. Wiecki, and C. Fonnesbeck. Probabilistic Programming in Python using PyMC3. *PeerJ Comput. Sci.*, 2:e55, 2016.

[104] U Seipold. Temperature Dependence of Thermal Transport Properties of Crystalline Rocks—a General Law. *Tectonophysics*, 291(1-4):161–171, 1998.

[105] P Sharma and T.S. Bhatti. A Review on Electrochemical Double-Layer Capacitors. *Energy Convers. Manage.*, 51(12):2901–2912, 2010.

[106] P. Sidles and G. Danielson. Thermal Diffusivity of Metals at High Temperatures. *J. Appl. Phys.*, 25(1):58–66, 1954.

[107] P Simon, Y Gogotsi, and B Dunn. Where Do Batteries End and Supercapacitors Begin? *Science*, 343(6176):1210–1211, 2014.

[108] E.P. Simonenko, D.V. Sevast'Yanov, N.P. Simonenko, V.G. Sevast'Yanov, and N.T. Kuznetsov. Promising Ultra-High-Temperature Ceramic Materials for Aerospace Applications. *Russ. J. Inorg. Chem.*, 58(14):1669–1693, 2013.

[109] Sobol and M Ilya. Global Sensitivity Indices for Nonlinear Mathematical Models and Their Monte Carlo Estimates. *Math Comput Simul.*, 55(1-3):271–280, 2001.

[110] D. J. Spiegelhalter, N. G. Best, B. P. Carlin, and A. Van der Linde. Bayesian Deviance, the Effective Number of Parameters, and the Comparison of Arbitrarily Complex Models. Technical Report 98-009, 1998.

[111] Z Stević, Z Andjelković, and D Antić. A New PC and LabVIEW Package Based System for Electrochemical Investigations. *Sensors*, 8(3):1819–1831, 2008.

[112] S Sun, M Huang, P Wang, and M Lu. Controllable Hydrothermal Synthesis of Ni/Co MOF as Hybrid Advanced Electrode Materials for Supercapacitor. *J. Electrochem. Soc.*, 166(10):A1799, 2019.

[113] P Taberna, P Simon, and J Fauvarque. Electrochemical Characteristics and Impedance Spectroscopy Studies of Carbon-Carbon Supercapacitors. *J. Electrochem. Soc.*, 150(3):A292, 2003.

[114] P.M Tagade and H Choi. A Generalized Polynomial Chaos-Based Method for Efficient Bayesian Calibration of Uncertain Computational Models. *Inverse Probl Sci Eng.*, 22(4):602–624, 2014.

[115] T. Tanaka and H. Suzuki. The Thermal Diffusivity of Pyrolytic Graphite at High Temperatures. *Carbon*, 10(3):253–257, 1972.

[116] R Tatara, P Karayaylali, Y Yu, Y Zhang, L Giordano, F Maglia, R Jung, P Schmidt, I Lund, and Y Shao-Horn. The Effect of Electrode-Electrolyte Interface on the Electrochemical Impedance Spectra for Positive Electrode in Li-ion Battery. *J. Electrochem. Soc.*, 166(3):A5090, 2018.

[117] K.A Terrani, D Wang, L.J Ott, and R.O. Montgomery. The Effect of Fuel Thermal Conductivity on the Behavior of LWR Cores During Loss-of-Coolant Accidents. *J. Nucl. Mater.*, 448(1-3):512–519, 2014.

[118] Y S Touloukian, R W Powell, C Y Ho, and M C Nicolaou. *Thermophysical properties of matter, the TPRC data series. Volume 10. Thermal diffusivity. Data book. 1974*, volume 10. 1 1974.

[119] J. Vandersande and R. Pohl. Simple Apparatus for the Measurement of Thermal Diffusivity between 80–500 K using the Modified Ångström method. *Rev. Sci. Instrum.*, 51(12):1694–1699, 1980.

[120] E. Visser, E. Versteegen, and W. van Enckevort. Measurement of Thermal Diffusion in Thin Films using a Modulated Laser Technique: Application to Chemical-Vapor-Deposited Diamond Films. *J. Appl. Phys.,*, 71(7):3238–3248, 1992.

[121] E.P Visser, E.H Versteegen, and W van Enckevort. Measurement of Thermal Diffusion in Thin Films using a Modulated Laser Technique: Application to Chemical-Vapor-Deposited Diamond Films. *J. Appl. Phys.,*, 71(7):3238–3248, 1992.

[122] J. Wang and N. Zabaras. A Bayesian Inference Approach to the Inverse Heat Conduction Problem. *Int. J. Heat Mass Transf.*, 47(17-18):3927–3941, 2004.

[123] J Wang and N Zabaras. Hierarchical Bayesian Models for Inverse Problems in Heat Conduction. *Inverse Probl.*, 21(1):183, 2004.

[124] J Wang and N Zabaras. Using Bayesian Statistics in the Estimation of Heat Source in Radiation. *Int. J. Heat Mass Transf.*, 48(1):15–29, 2005.

[125] M. Wheeler. Thermal Diffusivity at Incandescent Temperatures by a Modulated Electron Beam Technique. *Br. J. Appl. Phys.*, 16(3):365, 1965.

[126] G. White and S. Collocott. Heat Capacity of Reference Materials: Cu and W. *J. Phys. Chem. Ref. Data*, 13(4):1251–1257, 1984.

[127] G Wübbeler, M Krystek, and C Elster. Evaluation of Measurement Uncertainty and Its Numerical Calculation by a Monte Carlo Method. *Meas Sci Technol*, 19(8):084009, 2008.

[128] G Xiong, P He, D Wang, Q Zhang, T Chen, and T.S Fisher. Hierarchical Ni–Co Hydroxide Petals on Mechanically Robust Graphene Petal Foam for High-Energy Asymmetric Supercapacitors. *Adv. Funct. Mater.*, 26(30):5460–5470, 2016.

[129] H Xu, J Wu, Q Li, Y Chen, J Tang, and X Fan. Chemical Synthesis of De–doped Polyaniline for High Performance Aqueous Supercapacitive Material. *J. Electrochem. Soc.*, 165(16):A3903, 2018.

[130] J. Xu and T. S. Fisher. Enhancement of Thermal Interface Materials with Carbon Nanotube Arrays. *Int. J. Heat Mass Transf.*, 49(9-10):1658–1666, 2006.

[131] X Xu, Q Zhang, M Hao, Y Hu, Z Lin, L Peng, T Wang, X Ren, C Wang, Z Zhao, et al. Double-Negative-Index Ceramic Aerogels for Thermal Superinsulation. *Science*, 363(6428):723–727, 2019.

[132] Y. Xu, T. Shankland, A. Linhardt, D. Rubie, F. Langenhorst, and K. Klasinski. Thermal Diffusivity and Conductivity of Olivine, Wadsleyite and Ringwoodite to 20 GPa and 1373 K. *Phys. Earth Planet. Inter.*, 143:321–336, 2004.

[133] D Yang and A Laforgue. Laser Surface Roughening of Aluminum Foils for Supercapacitor Current Collectors. *J. Electrochem. Soc.*, 166(12):A2503, 2019.

[134] D Zhang and Y Rahmat-Samii. T Op-Cross-Loop Improving the Performance of the UWB Planar Monopole Antennas. *Opt. Technol. Lett.*, 59(10):2432–2440, 2017.

[135] S Zhang, S Brahim, and S Maat. High-voltage operation of binder-free cnt supercapacitors using ionic liquid electrolytes. *J. Mater. Res.*, 33(9):1179–1188, 2018.

[136] S Zhang and N Pan. Supercapacitors Performance Evaluation. *Adv. Energy Mater.*, 5(6):1401401, 2015.

[137] D. Zhao, X. Qian, X. Gu, S. A Jajja, and R. Yang. Measurement Techniques for Thermal Conductivity and Interfacial Thermal Conductance of Bulk and Thin Film Materials. *J Electron Packag.*, 138(4):040802, 2016.

[138] W Zhou and W Zhou. Enhanced Thermal Conductivity Accident Tolerant Fuels for Improved Reactor Safety–A Comprehensive Review. *Ann. Nucl. Energy.*, 119:66–86, 2018.

[139] X Zhu, T Man, M Tan, P Chung, M.A Teitell, and P Chiou. Distributed Colorimetric Interferometer for Mapping the Pressure Distribution in a Complex Microfluidics Network. *Lab Chip.*, 21(5):942–950, 2021.

[140] Y. Zhu. Heat-Loss Modified Angstrom Method for Simultaneous Measurements of Thermal Diffusivity and Conductivity of Graphite Sheets: The Origins of Heat Loss in Angstrom Method. *Int. J. Heat Mass Transf.*, 92:784–791, 2016.